

在BESIII上对粲偶素跃迁和强衰变的实验研究

(申请清华大学理学博士学位论文)

培 养 单 位 : 工 程 物 理 系

学 科 : 物 理 学

研 究 生 : 廖 广 睿

指 导 教 师 : 高 原 宁 教 授

二〇一三年四月

The study of charmonium transition and hadronic decay at BESIII

Dissertation Submitted to

Tsinghua University

in partial fulfillment of the requirement

for the degree of

Doctor of Science

in

Particle and Nuclear Physics

by

Liao Guangrui

Dissertation Supervisor : Professor Gao Yuanning

April, 2013

关于学位论文使用授权的说明

本人完全了解清华大学有关保留、使用学位论文的规定，即：

清华大学拥有在著作权法规定范围内学位论文的使用权，其中包括：（1）已获学位的研究生必须按学校规定提交学位论文，学校可以采用影印、缩印或其他复制手段保存研究生上交的学位论文；（2）为教学和科研目的，学校可以将公开的学位论文作为资料在图书馆、资料室等场所供校内师生阅读，或在校园网上供校内师生浏览部分内容；（3）根据《中华人民共和国学位条例暂行实施办法》，向国家图书馆报送可以公开的学位论文。

本人保证遵守上述规定。

（保密的论文在解密后应遵守此规定）

作者签名：_____

导师签名：_____

日 期：_____

日 期：_____

摘要

自从 J/ψ 和 $\psi(2S)$ 发现以来, 粲偶素就在实验上以及理论上成为重要的研究对象。对于粲偶素的研究有助于我们理解粲偶素衰变动力学以及微扰量子色动力学。尽管之前已经有很多关于这方面的工作, 但主要集中在总自旋为1, 轨道角动量为0的基态, 即 1^3S_1 态。对于其它粲偶素态的理解比较有限, 特别是 η_c , 虽然有许多文章已经对其进行预言, 但直到1980年, η_c 才在晶体球实验被发现。根据粒子数据组在2012年的统计, η_c 还有将近70%的衰变尚未发现, 而已经公布的数据的精度也比较低。另外, 对于粲偶素夸克态之间的跃迁一直以来都是粒子物理学家研究的重点, 这些过程的实验研究和理论对比是非常有意义的, 这些将有助于我们理解 Υ 的衰变机制。

升级改造后的BEPCh/BESIII的性能有了很大的提高, 比如说, 主漂移室的动量分辨从BESII的2.4%@1 GeV提高到了BESIII的0.5%@1 GeV, 量能器的能量分辨从BESII的20%@1 GeV提高到了BESIII的2.5%@1 GeV。这些提高对于探测光子和带电径迹起到非常重要的作用。另外, BESIII拥有世界上最大的 J/ψ 和 $\psi(2S)$ 统计样本。在2009年, BESIII上一共采集了 225×10^6 的 J/ψ 数据和 106×10^6 的 $\psi(2S)$ 数据。到了2012年, BESIII又采集了3亿的 $\psi(2S)$ 和8亿的 J/ψ 样本。所有的这些给了我们重新测量这些衰变道的机会。

通过在BESIII上收集到的 J/ψ 样本, 本文对 $\eta_c \rightarrow \phi\phi$ 和 $\eta_c \rightarrow \omega\phi$ 的分支比重新进行了测量, 得到的结果和之前的结果是一致的。前者测量精度相对于BESII的实验的结果提高了1.8倍, 并且进一步缩小了后者的可观察范围。

- $\eta_c \rightarrow \phi\phi$ 分支比: $Br(\phi\phi) = (2.09^{+0.10}_{-0.12}(\text{stat.}) \pm 0.58(\text{syst.})) \times 10^{-3}$
- $\eta_c \rightarrow \omega\phi$ 分支比: $Br(\omega\phi) < 3.14 \times 10^{-4} @ 90\%$

另外, 通过在BESIII上收集到的 $\psi(2S)$ 样本, 本文给出 $\psi(2S) \rightarrow \pi^0(\eta)J/\psi$ 这两个衰变道的精确测量结果, 该测量值和之前测量的平均值是一致的, 相比于平均值, R 值的测量精度提高了5倍。

- $\psi(2S) \rightarrow \pi^0 J/\psi$ 的分支比: $Br_1 = (1.26 \pm 0.02(\text{stat.}) \pm 0.03(\text{syst.})) \times 10^{-3}$
- $\psi(2S) \rightarrow \eta J/\psi$ 的分支比: $Br_2 = (33.75 \pm 0.17(\text{stat.}) \pm 0.86(\text{syst.})) \times 10^{-3}$
- 这两个衰变道的比值: $R = \frac{Br_1}{Br_2} = (3.74 \pm 0.06(\text{stat.}) \pm 0.04(\text{syst.})) \times 10^{-2}$

关键词: 粲偶素; η_c ; 强衰变; 精确测量

Abstract

The study of charmonium states has been an important subject for both experimental and theoretical work since the J/ψ and $\psi(2S)$ were discovered. Such study would be useful for people to understand the charmonium decay dynamics and test the perturbative QCD. Great effort had been made to the study of these states, but most of the work focused on the ground states with the total spin equaling to 1 and total orbital angular momentum equaling to 0, denoting with 1^3S_1 . The knowledge of other charmonium states was limit at that time, especially for η_c . Many theories have expected the state, it was not until 1980 that η_c was observed at Crystal Ball. According to the Particle Data Group (PDG) published in 2012, almost 70% of the total branching fraction are yet to be discovered while the values listed on the PDG are in very low precision. Moreover, transitions between different charmonium states have always been the major subjects for particle physicists. The comparison of experimental works with theory is meaningful, and it will be helpful for us to understand the mechanisms of Υ system.

The performance of the upgraded BEPCII/BESIII is highly improved, such as the momentum resolution of main drift chamber has risen from 2.4%@1 GeV at BESII to 0.5%@1 GeV at BESIII, the energy resolution of the electromagnetic calorimeter has increased from 20%@1 GeV at BESII to 2.5%@1 GeV at BESIII. It is helpful to measure the deposited energy and momentum of photons and other charged particles. In addition, BESIII has accumulated 225 million of J/ψ data sample and 106 million of $\psi(2S)$ sample in 2009. Both of the two samples are the largest ones in the world. In 2012, another 8 million of J/ψ sample and 3 million of $\psi(2S)$ sample have been accumulated at BESIII. These would provide us with a good opportunity to study these channels again.

Using 225×10^6 of J/ψ events number accumulated at BESIII detector, measurements on the branching fractions of $\eta_c \rightarrow \phi\phi$ and $\eta_c \rightarrow \omega\phi$ are performed, the results of our work are consistent with the previous ones, and the precision of the former channel is improved with a factor of about 1.8. And our work set a tight upper limit for the branching fraction of $\eta_c \rightarrow \omega\phi$.

- The branching fraction of $\eta_c \rightarrow \phi\phi$

$$Br(\eta_c \rightarrow \phi\phi) = (2.09_{-0.12}^{+0.10}(\text{stat.}) \pm 0.58(\text{syst.})) \times 10^{-3}$$

Abstract

- The branching fraction of $\eta_c \rightarrow \omega\phi$

$$Br(\eta_c \rightarrow \omega\phi) < 3.14 \times 10^{-4} @ 90\%$$

In addition, precise measurements of $\psi(2S) \rightarrow \pi^0(\eta)J/\psi$ decay modes with 106×10^6 $\psi(2S)$ data sample are performed. The measured branching fractions of these decay channels are consistent with the previous world average ones, and a precision improvement of about a factor of 5 for R -ratio has obtained in our work.

- The branching fraction of $\psi(2S) \rightarrow \pi^0 J/\psi$

$$Br_1 = (1.26 \pm 0.02(\text{stat.}) \pm 0.03(\text{syst.})) \times 10^{-3}$$

- The branching fraction of $\psi(2S) \rightarrow \eta J/\psi$

$$Br_2 = (33.75 \pm 0.17(\text{stat.}) \pm 0.86(\text{syst.})) \times 10^{-3}$$

- The ratio of these two channels

$$R = \frac{Br_1}{Br_2} = (3.74 \pm 0.06(\text{stat.}) \pm 0.04(\text{syst.})) \times 10^{-2}$$

Key words: charmonium; η_c ; hadronic decay; precise measurement

Contents

Chapter 1 Introduction	1
1.1 Particle Physics	1
1.1.1 Mesons and Hadrons	1
1.1.2 Quark Model	2
1.2 Charmonium Physics	7
1.3 Motivation	9
1.3.1 η_c decay	9
1.3.2 $\psi(2S)$ decay into $\pi^0(\eta)J/\psi$	12
1.4 Structure of the paper	13
Chapter 2 The accelerator and detector	14
2.1 BEPCII	15
2.2 BESIII	15
2.2.1 Main Drift Chamber	18
2.2.2 The Time of Flight	18
2.2.3 Electro-Magnetic Calorimeter	20
2.2.4 Muon Identifier	22
2.3 Trigger	25
2.4 Data Acquisition	25
2.5 Monte Carlo Generators	27
2.5.1 Introduction	27
2.5.2 Generator framework	27
2.5.3 BESIII Generators	27
Chapter 3 The study of $J/\psi \rightarrow \gamma\eta_c, \eta_c \rightarrow \phi\phi(\omega\phi)$	30
3.1 $J/\psi \rightarrow \gamma\eta_c, \eta_c \rightarrow \phi\phi, \phi \rightarrow K^+K^-$	30
3.1.1 Event selection	30
3.1.2 Angular distributions	32
3.1.3 Background study	35
3.1.4 Fitting of the mass spectrum	40
3.1.5 Source of systematic error	43
3.1.6 Numerical result and Summary	50
3.2 $J/\psi \rightarrow \gamma\eta_c, \eta_c \rightarrow \omega(\pi^0\pi^+\pi^-)\phi(K^+K^-)$	50
3.2.1 Event selection	50

Contents

3.2.2	The uplimit calculation of the decay channel	52
3.2.3	Source of systematic error	52
3.2.4	Numerical result	61
3.2.5	Cross check	62
Chapter 4 Precision measurement on the branching		
fractions of $\psi(2S)$ hadronic transitions to J/ψ		66
4.1	$\psi(2S) \rightarrow \pi^0(\gamma\gamma)J/\psi(l^+l^-)$	66
4.1.1	Event selection and background study.....	66
4.1.2	Fit to mass spectrum of π^0 in data	71
4.2	$\psi(2S) \rightarrow \eta(\gamma\gamma)J/\psi(l^+l^-)$	75
4.2.1	Event selection and background study.....	75
4.2.2	Fit to mass spectrum of η in Data	79
4.3	Source of systematic error	80
4.3.1	Total number of $\psi(2S)$	83
4.3.2	Tracking Efficiency	83
4.3.3	4C Kinematic Fitting	86
4.3.4	E/p ratios	88
4.3.5	Mass window cut on the invariant mass of the two leptons	90
4.3.6	Mass window cut on the invariant mass of $M_{\gamma l^+ l^-}$	91
4.3.7	The background shape.....	93
4.3.8	Summary of systematic errors	95
4.4	Summary and discussion.....	95
Chapter 5 Conclusions		98
5.1	Summary.....	98
5.1.1	$J/\psi \rightarrow \gamma\eta_c, \eta_c \rightarrow \phi\phi(\omega\phi)$	98
5.1.2	Hadronic transitions from $\psi(2S)$ to J/ψ	99
5.2	Outlook	99
Reference		101
Acknowledgement		106
声 明		107
Appendix A		108
A.1	Estimation of the uncertainty of 4C-kinematic fitting	108
A.1.1	$J/\psi \rightarrow \gamma\eta_c(\phi\phi)$	108
A.1.2	$J/\psi \rightarrow \gamma\eta_c, \eta_c \rightarrow \omega(\pi^0\pi^+\pi^-)\phi(K^+K^-)$	110
A.1.3	$\psi(2S) \rightarrow \pi^0 J/\psi(l^+l^-)$ and $\eta J/\psi(l^+l^-)$	116

Contents

Appendix B	126
B.1 Amplitude.....	126
B.1.1 Amplitude.....	126
B.1.2 Breit-Wigner	128
B.2 Fit method	128
Resume and Publications	129

List of main acronyms

BEPC	Beijing Electron-Positron Collider
BES	Beijing Spectrometer
SM	Standard Model
QCD	Quantum Chromodynamics
QED	Quantum Electrodynamics
EW	Electro-Weak
NRQCD	Non Relativistic QCD
SU(n)	Special Unitary (group) of degree n
p_t	Transverse momentum
$Q\bar{Q}$	Heavy quarkonium
PID	Particle Identification

Chapter 1 Introduction

‘What is the matter made of ?’. This is an old basic question that has puzzled scientists of all times. To answer the question, the concept of atom was first introduced by Leucippus, a famous philosopher of ancient Greece. He proposed that all matters are composed of different kinds of atoms, which do not have any substructure. In other words, atoms are the building blocks of the universe. They can not be separated into smaller particles. The modern concept of atom was proposed by John Dalton in 1803. J. J. Thomson, a British physicist, discovered electron and measured the ratio of the charge to the mass of electron, and proposed ‘plum-pudding’ picture of atom. In 1909, Rutherford and his colleagues observed the deflection of the outgoing α particles from their incident directions, some particles were drastically deflected, even occasionally going back to the source. Based on these findings, Rutherford formulated his model of the atom in 1911. Rutherford model indicates that all positive particles of atom, concentrating with nearly all of the atom’s mass, are orbited by electrons. Upon the discovery of the first anti-matter, positron, and neutron, the concept of elementary particle became widely acknowledged.

1.1 Particle Physics

Particle physics is a branch of physics that is grounded on experiment. It is a subject to identify basic elements of matter and the forces acting among them. These basic elements are known as elementary particles, which means that they are the basic particles that do not have substructures. Particle physics had made great achievements in terms of exploring the basic elements of matters and the law of their interactions since the 20th century.

1.1.1 Mesons and Hadrons

To describe the components of nucleus, Dmitri Ivanenko proposed a proton-neutron model in 1932. H. Yukawa, a Japanese physicist, constructed a theory to explain the force between nucleons in 1935. It stated that the nuclear force is mediated by a massive particle, named by pion, denoted by π .

In 1937 Anderson observed a new particle with a mass of about 200 times of electron from cosmic rays. It was thought to be Yukawa's pion at first. But latter the idea was found to be mistaken and the particle was finally confirmed to be a lepton like electron, named muon, denoted by μ . The real Yukawa' pion was found by C. Powell and his colleagues from Bristol University in 1947. Soon after the discovery of pion, British physicists G. D. Rochester and C. C. Butler published the observation of a pair of unstable particles in 1947. They are proved through experiments that these particles were always produced in pairs by strong force, but decayed slowly with lifetime typical of weak interaction processes. For the following years, more particles with the similar property had been found in cosmic ray experiment and are classified into two kinds, K mesons and hyperons. To explain the strange behaviour, Gell-Mann and Nishijima proposed a new conservation of strangeness (S) which was applied only to the strong interactions. Like other quantum numbers, the strangeness is assigned to each particle. The characteristics of these particles are summarized in table 1.1.

Table 1.1 The quantum number of hyperons and K mesons.

Particle	Λ	Σ^+	Σ^0	Σ^-	Ξ^0	Ξ^-	K^+	K^0	K^-	\bar{K}^0
Q	0	+1	0	-1	0	-1	+1	0	-1	0
S	-1	-1	-1	-1	-2	-2	+1	+1	-1	-1

Both K mesons and hyperons aforementioned have enough lifetime to leave observable tracks in detectors for analysis. The lifetime of some particles, named hadron, are so short that there are not any observable tracks. These unstable hadrons can be observed as 'resonance'. By early 1960s, resonances have been observed in experiment, such as ω (Maglic *et al.* 1961), ρ (Erwin *et al.* 1961), ϕ (Connolly *et al.* 1963), K^* and \bar{K}^* (Alston *et al.* 1961). All these particles are assigned well-defined values of various quantum numbers such as spin, isospin, strangeness and baryon number. The most important task for physicists was to classify these particles according to the nature of the constituents that could be derived at that time.

1.1.2 Quark Model

G. Zweig^[1] and M. Gell-Mann^[2-4] independently proposed that the hadrons are made up of constituents, called quarks by Gell-Mann in 1964. As they stated the baryons are made of three quarks, and the mesons of a quark and an antiquark^[5]. This combination is based on the SU(3) group which can be described mathematically:

$$q \otimes \bar{q} \equiv 3 \otimes \bar{3} = 1 \oplus 8 \tag{1-1}$$

$$q \otimes q \otimes q \equiv 3 \otimes 3 \otimes 3 = 1 \oplus 8 \oplus 8 \oplus 10 \tag{1-2}$$

The constituent quarks of mesons and baryons are shown in figure 1.1 and figure 1.2, respectively.

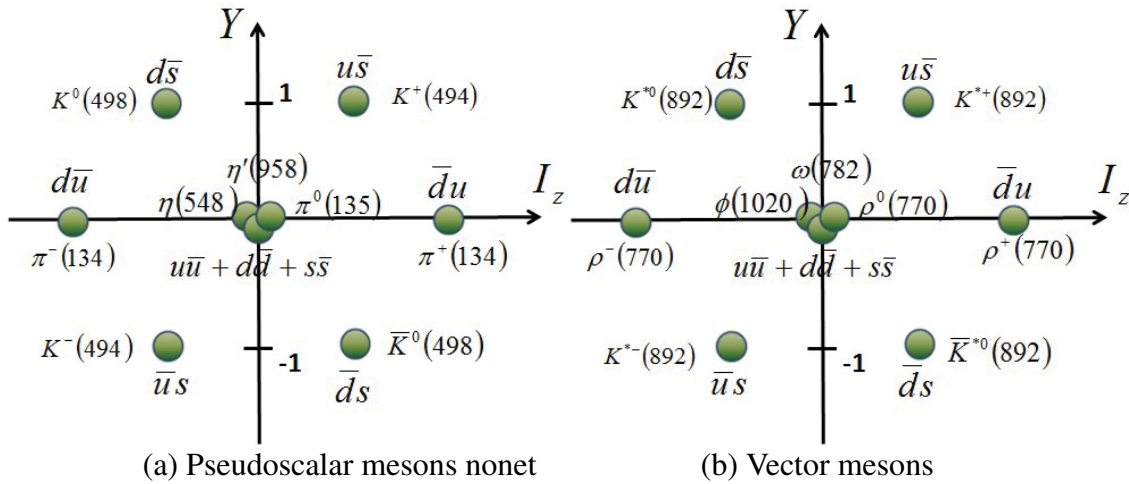


Figure 1.1 SU(3) multiples of mesons made of u, d, s quarks. I_z is the third component of the isospin of the meson, while Y is the hypercharge of the meson. The approximate values of the masses are in MeV.

In 1974, a new particle, J/ψ was discovered independently by two research groups, one at the Brookhaven National Laboratory^[6], headed by Samuel Ting from MIT, and the other one at the Stanford Linear Accelerator Center^[7], headed by Burton Richter. The discovery of J/ψ has confirmed the expectation that there must be a fourth quark to explain the suppression of the the ‘neutral current’, which is proposed by S. Glashow, I. Iliopoulos and L. Maiani in 1970^[5]. And it was soon confirmed J/ψ to be a bound state of $c\bar{c}$, known as a charmonium. More and more charmonium and charmed mesons have

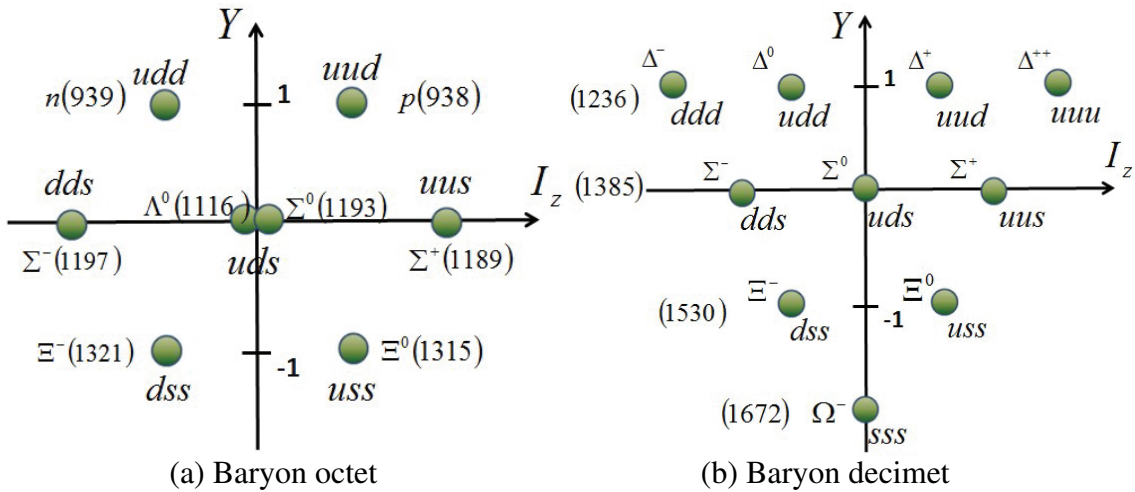


Figure 1.2 SU(3) multiples of baryon made of u, d, s quarks. I_z is the third component of the isospin of the baryon, while Y is the hypecharge of the baryon. In parentheses the masses are in MeV.

been observed since the discovery of J/ψ . These particles are expected to have explicit charm number and higher spins for their excited states. It is required that the SU(3) flavour symmetry to describe hadrons should be extended to group SU(4) to combine charmed mesons with previous baryons together. Figure 1.3 shows the SU(4) baryons multiplets, the bottom level shows SU(3) decuplet.

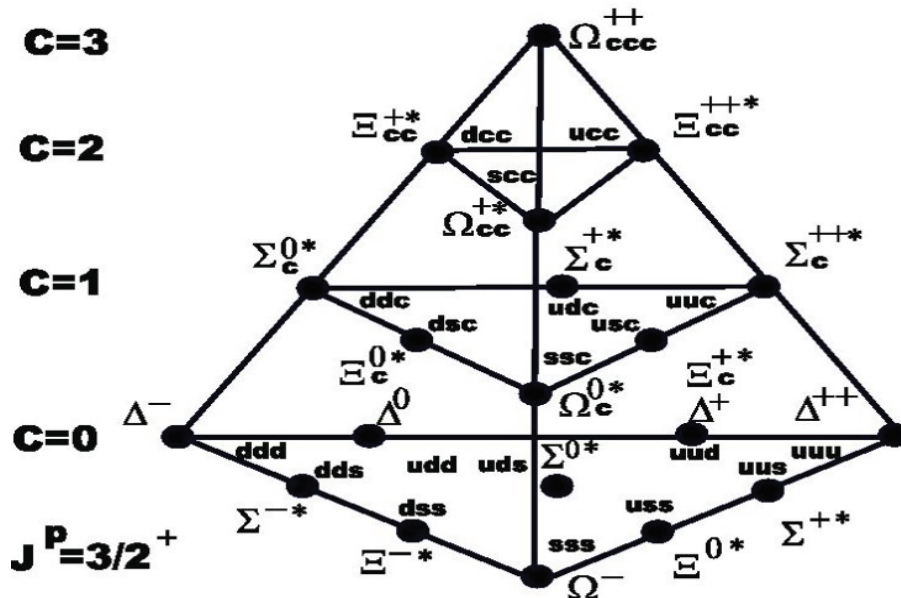


Figure 1.3 SU(4) multiplets of baryons made of $u, d, s,$ and c quarks.

Soon after physicists had digested the nature of J/ψ , another particle was discovered

in 1977 by the Fermilab E288 experiment team led by Leon M. Lederman^[8], named with bottom quark or b quark, also known as beauty quark. It took eighteen years since the discovery of b quark to find its partner, the t quark, discovered at the Tevatron proton-antiproton collider at Fermilab, in 1995^[9]. So far six members of quark family have been established in experiment, which are taken into the foundation of QCD theory. The quantum number and mass of these quarks are listed in table 1.2.

Table 1.2 The quantum numbers and masses of quarks

	Q	I	I_z	S	C	B	T	\mathcal{B}	Y	Mass ^[10]
d	-1/3	1/2	-1/2	0	0	0	0	1/3	1/3	$4.8^{+0.7}_{-0.3}$ MeV/c ²
u	+2/3	1/2	+1/2	0	0	0	0	1/3	1/3	$2.3^{+0.7}_{-0.5}$ MeV/c ²
s	-1/3	0	0	-1	0	0	0	1/3	-2/3	95 ± 5 MeV/c ²
c	+2/3	0	0	0	+1	0	0	1/3	4/3	1.275 ± 0.025 GeV/c ²
b	-1/3	0	0	0	0	-1	0	1/3	-2/3	4.18 ± 0.03 GeV/c ²
t	+2/3	0	0	0	0	0	+1	1/3	4/3	160^{+5}_{-4} GeV/c ²

Besides the quarks, there are six leptons named as electron (e), moun (μ), tau (τ) and three neutrinos (ν_e, ν_μ, ν_τ) consisting of the elementary particles of the Standard Model (SM) which formulated throughout the mid to late 20th century. It has been subjected to intense experimental scrutiny and generally accepted as the fundamental theory of elementary particle physics.

In SM, there are three kinds of gauge bosons. The first kind is photon, which mediates the electromagnetic interaction. The second ones, including W and Z bosons, mediate the weak interaction. The last one is gluon, which mediates the strong interaction. Higgs is a scalar particle to break the electroweak symmetry and to give masses to all of the elementary particles. A new boson has been reported by ATLAS and CMS experiments at CERN's Large Hadron Collider on 4 July 2012. The mass of the boson is around $126 \text{ GeV}/c^2$, consistent with the Higgs boson expected in SM. More works are desired to check whether it is indeed the Higgs particle. These particles are summarized in figure 1.4. There are four fundamental interactions among matters in SM, including strong interaction, weak interaction, electromagnetism and gravitation. Table 1.3 is the summary of the fundamental interactions.

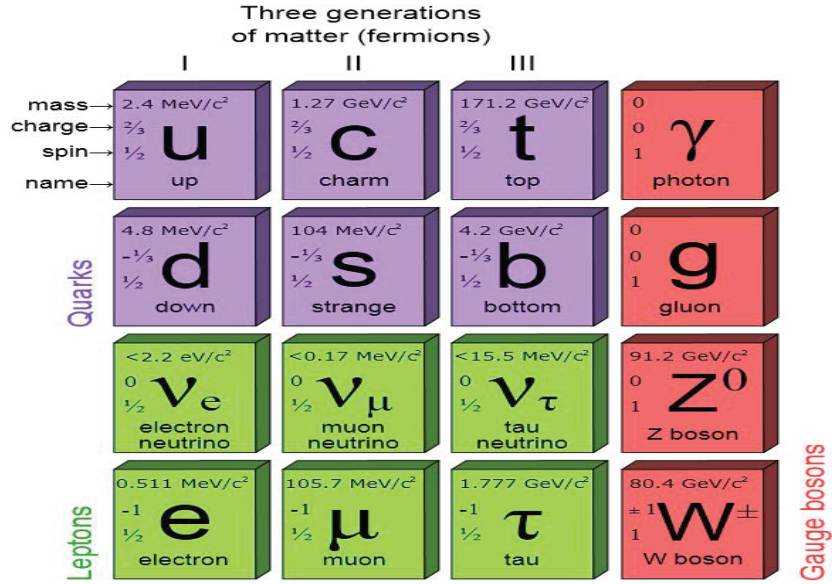


Figure 1.4 The quark generation

Table 1.3 Summary of four fundamental interactions.

	Strong	Electromagnetism	Weak	Gravitation
Source	quark	charge	weak hypercharge	mass
Coupling	$\alpha_s = \frac{g_s^2}{4\pi\hbar c}$	$\frac{G_F(M_p c^2)^2}{(\hbar c)^3}$	$\alpha = \frac{e^2}{4\pi\epsilon_0\hbar c}$	$\frac{G_N M_p^2}{4\pi\hbar c}$
Constant	$\cong 1 \times 10^{-5}$	$\cong 1/137$	$\cong 1 \sim 10$	$\cong 5 \times 10^{-40}$
Mediators	gluons	photons	bosons(W [±] , Z ⁰)	—
Interaction time(s)	10 ⁻²³	10 ⁻¹⁶	10 ⁻¹⁰	—
Range	1 fm	∞	1/400 fm	∞

1.2 Charmonium Physics

The concept of ‘Charm’ was proposed by Bjorken and Glashow^[11] according to the idea of the ‘Eightfold way’ by Gell-Mann^[12]. And the expectation was confirmed by the discovery of J/ψ . Soon another bound state of a charmed quark and antiquark, $\psi(2S)$ was found at Stanford Linear Accelerator Center in 1974^[13] and then many new charmed states have been discovered and identified in charmonium family^[14–19] shown in figure 1.5.

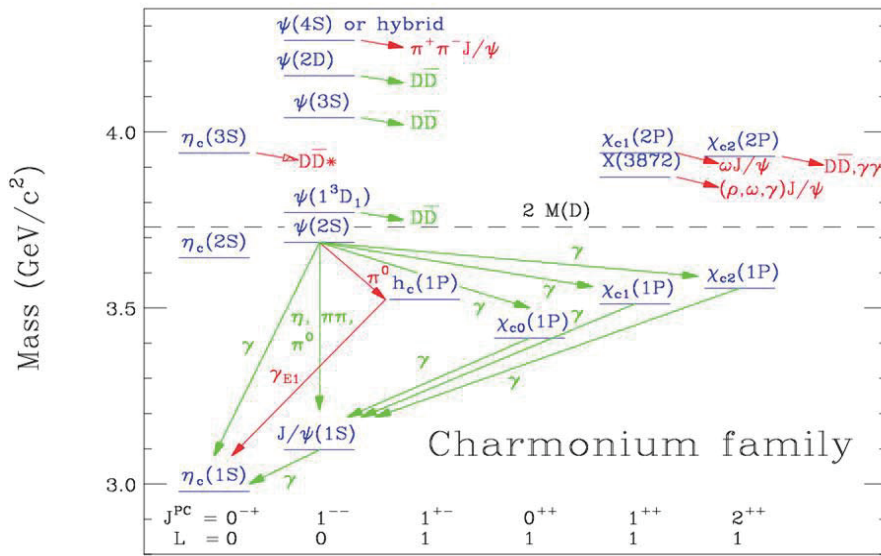


Figure 1.5 The charmonium family.

One of the reasons why the charmonium physics appealing to physicists is that the mass of charmed quark is much larger than Λ_{QCD} , the typical energy scale of the strong interaction. Charmonium states are an ideal laboratory to probe the feature of Quantum chromodynamics (QCD), the theory of strong interaction. It is helpful for people to search for exotica, and to probe the forces between quarks.

The reason why the decay width of charmonium states are extremely small is usually explained with the Okubo-Iizuka-Zweig (OZI) rule^[20]. It states that the process, in which the initial quark pairs cannot appear as part of the final state particles, is suppressed. The assumption is helpful for people to figure out why the branching fraction of $\phi \rightarrow K^+K^-$ ($s\bar{s} \rightarrow (s\bar{u})(\bar{s}u)$) is dominate while the decay of $\phi \rightarrow 3\pi$ ($s\bar{s} \rightarrow (n\bar{n})(n\bar{n})$, where $n(n\bar{)} = u, d$) is a rare decay. The OZI rule can be described with quark diagrams as shown in figure 1.6. The decays of J/ψ into open-charmed models are forbidden because the mass

of J/ψ is too light to decay into any charmed mesons. This has made it possible to precisely measure the masses of states that in the quark model which are identified with N,L multiplets^[21].

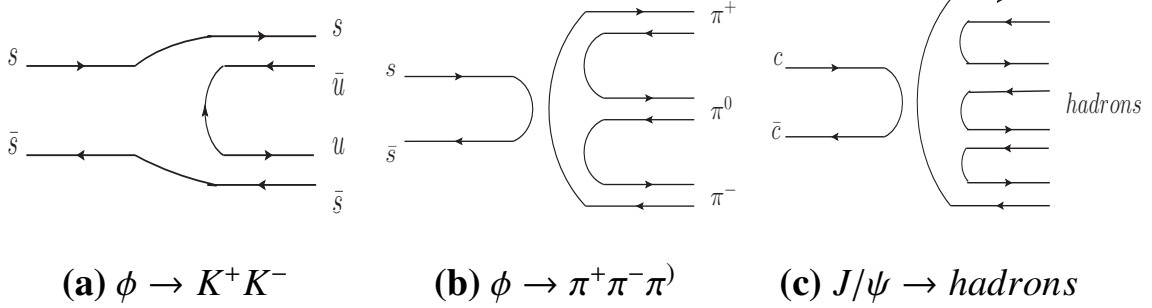


Figure 1.6 Diagrams of $\phi(1020)$ and J/ψ decays. (a) OZI allowed, (b) and (c) OZI suppressed.

The mass of charmed quark is so large that the motion of a charmed quark is less important inside a charmonium state. So a charmonium state can be described as a non-relativistic bound state. The *nonrelativistic* QCD (NRQCD)^[22–24] is regarded to be an effective theory to deal with charmonium relevant processes such as spectroscopies, annihilation decays, and inclusive productions. There are three energy scales, including M_c , $M_c v$, $M_c v^2$, where M_c and v are the mass of c quark and the velocity of the charmed quarks, respectively. These energy scales satisfy a hierarchy relation for the charmonium and bottomonium:

$$M_q^2 \gg (M_q v)^2 \gg (M_q v^2)^2, \quad (1-3)$$

Where M_q is the mass of quark (q).

After taking into account the contribution of these energy scales, the NRQCD effective lagrangian can be expressed as follow^[22–24]:

$$\mathcal{L}_{NRQCD} = \mathcal{L}_0 + \mathcal{L}_1 + \delta\mathcal{L}, \quad (1-4)$$

$$\mathcal{L}_0 = \psi^\dagger (iD_0 + \frac{D^2}{2m_c}) \psi + \chi^\dagger (iD_0 + \frac{D^2}{2m_c}) \chi, \quad (1-5)$$

$$\delta\mathcal{L} = \frac{c_1}{8m_c^3} \psi^\dagger (D^2)^2 \psi + \frac{c_2}{8m_c^2} \psi^\dagger g(D \cdot E + E \cdot D) \psi + \frac{c_3}{2m_c} \psi^\dagger g\sigma \cdot B \psi$$

$$+ i \frac{c_4}{8m_c^2} \psi^\dagger g \sigma \cdot (D \times E - E \times D) \psi + c.c., \quad (1-6)$$

where \mathcal{L}_0 is the leading order of NRQCD effective lagrangian, while \mathcal{L}_l is the usual lagrangian that describes gluons and light quarks. $\delta\mathcal{L}$ is the correction to \mathcal{L}_0 . ψ and χ denote the Pauli spinor fields of quark and antiquark, respectively. m_c is the mass of charmed quark. Gauge invariance implies that gluon field appears in the lagrangian always only through the gauge-covariant derivatives iD_0 , $i\mathbf{D}$ and the QCD field strength \mathbf{E} , \mathbf{B} .

Comparing with other theories, such as color-singlet model, color-evaporation and QCD Sum Rules, NRQCD is more effective to describe charmonium system.

The charmonium physics has been an active field both for theoretical and experimental researchers. Especially, it receive more attentions since many charmonium-like new particles are discovered recently in experiment. The advantage to study charmonium physics is motivated by:

1. Charmonium is an ideal system to study the non-relativistic features of charmed quark.
2. It is helpful for people to understand the production mechanism of color octet. Although there were many researches about the charmonium state^[25–27], it is still not clear about the contribution of color octet in the production of charmonium states^[28] up to now. The experimental results of electron-proton collision at HERA^[29] and CDF at Fermilab^[30] are conflict with the theoretical expectation.
3. The possibility of finding new bound states of gluons (glueballs, gluonia) in the radiative decays of J/ψ ^[31].
4. The hadronic transitions are important decay modes in heavy quarkonia (bound states of heavy quark q and antiquark \bar{q}), which can give information on the structure of QCD confinement as well as on the gluon content of light hadrons and provide an experimental testing ground for the theoretical calculations of nonperturbative QCD^[32].

1.3 Motivation

1.3.1 η_c decay

Charmonium mesonic decays have been studied on theoretical ground for more than two decades^[33–37]. The η_c , the lowest-lying pseudoscalar charmonium state, has been

known for many years. The mass was predicted in potential models^[38–41] and dispersion relation models^[42,43]; the η_c lies below J/ψ about $20\sim 100\text{MeV}/c^2$. A candidate for η_c , $X(2830)$ ^[44], was reported by DASP in 1977. But the state was not confirmed by Crystal Ball collaboration with even more data sample^[45]. The η_c was not observed until 1980 via radiative decay from J/ψ and $\psi(2S)$ near $2980\text{MeV}/c^2$ by Crystal Ball^[46] and was confirmed by MARKII groups^[47]. The spin and parity of η_c are identified with 0^{-+} by a set of experiments^[48–51].

The η_c decays into two- or three-bodies have been extensively studied in literature^[52]. According to perturbation theory, η_c decays through annihilation into two gluons and the gluons materializing into light mesons. The study of η_c mesonic decays is helpful for us to understand the gluon dynamics. For example, the relative ratio of contributions from the three different mechanisms for the decays of $\eta_c \rightarrow VV$ (V denotes Vector meson) as shown in figure 1.7, can be extracted if all branching ratios for VV final states are measured^[48].

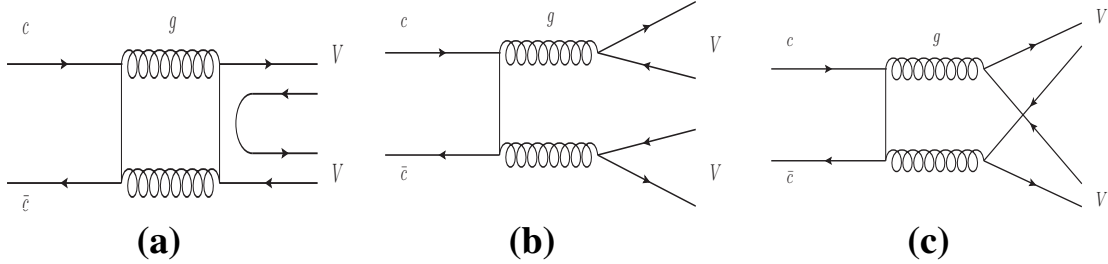


Figure 1.7 Various mechanisms for $\eta_c \rightarrow VV$. In (b) the produced mesons are color-octet states, but final-state interactions (i.e., exchange of soft gluons) are assumed to turn them into color singlets.

The branching fractions have been calculated with three different Bethe-Salpeter wave functions^[53], but their results are lower than the experimental values quoted from particle data group (PDG)^[10] by two or three orders of magnitude as shown in table 1.4. More precise results from higher statistics are expected to clarify the situation.

For charmonium $\psi(\lambda)$ decays into light hadrons $h_1(\lambda_1)$ and $h_2(\lambda_2)$, the asymptotic behavior of the branching fraction from a Perturbative QCD (pQCD) calculation to leading twist accuracy gives^[34]:

$$Br[\psi(\lambda) \rightarrow h_1(\lambda_1)h_2(\lambda_2)] \sim \left(\frac{\Lambda_{\text{QCD}}^2}{m_c^2} \right)^{|\lambda_1+\lambda_2|+2} \quad (1-7)$$

Table 1.4 Comparison of branching fraction for $\eta_c \rightarrow VV$ between theoretical predictions^[53] and PDG^[10] results. Gauss, Exponent, and Power refer to three different Bethe-Salpeter wave functions

Decay channel	Gauss	Exponent	Power	PDG
$\eta_c \rightarrow \rho\rho$	2.3×10^{-5}	8.7×10^{-5}	2.8×10^{-4}	$(1.8 \pm 0.5)\%$
$\eta_c \rightarrow K^* \bar{K}^*$	2.8×10^{-5}	8.6×10^{-5}	2.8×10^{-4}	$(6.8 \pm 1.3) \times 10^{-3}$
$\eta_c \rightarrow \phi\phi$	4.2×10^{-6}	1.6×10^{-5}	5.0×10^{-5}	$(1.94 \pm 0.30) \times 10^{-3}$

where λ, λ_1 and λ_2 denote the helicities of the corresponding hadrons. Here m_c is the charmed quark mass and Λ_{QCD} is the QCD energy scale factor. If the light quark masses are neglected, the vector-gluon coupling conserves quark helicity and this leads to the helicity selection rule (HSR)^[33]: $\lambda_1 + \lambda_2 = 0$. If the helicity configurations do not satisfy this relation, the branching fraction should be suppressed.

For η_c decays into vector meson pairs (VV), $\eta_c(Q) \rightarrow \phi(p_1, \lambda_1)\phi(p_2, \lambda_2)$, the conservation of parity requires that the decay amplitude is of asymmetric over the polarization vector of two vector mesons, namely, $M \sim \epsilon_{\alpha\beta\mu\nu} Q^\alpha (p_1 - p_2)^\beta \epsilon^\mu(\lambda_1) \epsilon^\nu(\lambda_2)$, where Q, p_1, p_2 are the four-vector momentum for η_c and ϕ mesons, respectively. λ_1 and λ_2 are the helicity values of two vector mesons. Hence the nonvanishing amplitude require that the two vector mesons must have the different polarization state, which leads to the relation $|\lambda_1 + \lambda_2| = 1$. Hence the branching fraction is suppressed.

Many theoretical calculations based on pQCD scheme^[53,54] confirmed the expectation of a suppressed branching fraction by the HSR. These results indicate that contributions from non-pQCD effects may dominate the decay of $\eta_c \rightarrow VV$, such as the charmed meson re-scattering mechanisms^[55], and the $s\bar{s}$ -quark pair production in the 3P_0 model^[56].

The η_c decays into $\phi\phi$ was once suggested to be a reliable channel to measure the spin and parity of η_c ^[57,58], and it was firstly observed by the DM2 collaboration^[59], and the improvement measurement of branching fraction was performed at BESII^[60,61]. The precision of the current world average value for this channel is very low^[10]. Recently, the double OZI suppressed decay of $\chi_{c0,1} \rightarrow \omega\phi$ has been observed by BESIII Collaboration^[62]. But the similar decay of $\eta_c \rightarrow \omega\phi$ has not been observed so far.

With the largest J/ψ data sample of 225 million decays accumulated at the BESIII

detector in 2009, it will provide an opportunity for us to improve the precision of the branching fraction for $\eta_c \rightarrow \phi\phi$ and to search for the decay of $\eta_c \rightarrow \omega\phi$. In this work, we performed an improved measurement for the branching fraction of $\eta_c \rightarrow \phi\phi$, and $\eta_c \rightarrow \omega\phi$.

1.3.2 $\psi(2S)$ decay into $\pi^0(\eta)J/\psi$

The study of the hadronic transitions between charmonium states has been an active field both for experimental and theoretical research. These transitions are caused by the interaction of heavy quarks with gluons and the gluons materializing as light mesons, i.e. π and η . The decays $\psi(2S) \rightarrow \eta J/\psi$ and $\pi^0 J/\psi$ are important probes of $\psi(2S)$ decay mechanisms that are characterized by the emission of a soft hadron, which were first observed thirty years ago, and improved measurements of the corresponding branching fractions were performed by the BESII^[63] and CLEO^[64] collaborations. The QCD multipole expansion technique was developed for applications to these heavy quarkonium system processes. For this, the measured branching fraction of $\psi(2S) \rightarrow \eta J/\psi$ can be used to predict the η transition rate between Υ states^[65].

The branching fraction ratio, $R = \frac{\mathcal{B}(\psi(2S) \rightarrow \pi^0 J/\psi)}{\mathcal{B}(\psi(2S) \rightarrow \eta J/\psi)}$, with \mathcal{B} denoting the individual branching fraction, was suggested as a reliable way to measure the light-quark mass ratio m_u/m_d ^[66]. Based on axial anomaly and QCD multipole expansion, the ratio is calculated to be $R = 0.016$ with the conventionally accepted values of the quark masses $m_s = 150 \text{ MeV}/c^2$, $m_d = 7.5 \text{ MeV}/c^2$ and $m_u = 4.2 \text{ MeV}/c^2$ ^[67]. Previously published measurements of this ratio give a significantly larger value of $R = 0.040 \pm 0.004$ ^[10]. Recently, using chiral-perturbation theory, the Jülich group investigated the source of charmed-meson loops in these decays as a possible explanation for this discrepancy^[68]. Under the assumption that the charmed-meson loop mechanism saturates the $\psi(2S) \rightarrow \pi^0(\eta)J/\psi$ decay widths, they obtained a value $R = 0.11 \pm 0.06$, which indicates that the charmed-meson loop mechanism can play an important role in explaining the data. With parameters introduced into the charmed-meson loop fixed using $\mathcal{B}(\psi(2S) \rightarrow \eta J/\psi)$ as input, the hadron-loop contribution to the isospin violation decay $\psi(2S) \rightarrow \pi^0 J/\psi$ can be evaluated^[69,70]. Measurements of these branching fractions can provide experimental evidence for hadron-loop contributions in charmonium decays, and impose more stringent constraints on charmed-meson loop contributions. It will also help clarify the influence of long-distance effects in other charmonium decays, *e.g.*

$\psi(3770) \rightarrow \pi^0(\eta)J/\psi$ ^[70,71], $\psi(2S) \rightarrow \gamma\eta_c$, and $J/\psi \rightarrow \gamma\eta_c$ ^[72].

The measurement results of this thesis are based on the 106 million of $\psi(2S)$ data sample accumulated in 2009 at BESIII. The large data sets provide us a opportunity to make a precision measurement on the branching fractions.

1.4 Structure of the paper

There are five chapters in the paper.

- The first chapter is the introduction to particle physics and the motivation of my work.
- The second chapter is about the BEPCII/BESIII.
- The third chapter is the study of $\eta_c \rightarrow VV$ via J/ψ radiative decay.
- The forth chapter is the precision measurement on $\psi(2S) \rightarrow \pi^0(\eta)J/\psi$.
- The last chapter is the summary and outlook.

Chapter 2 The accelerator and detector

The progress in our understanding of the fundamental laws of Nature is directly linked to our ability to develop instruments to detect particles and measure their characteristics, with increasing precision and sensitivity^[73].

The Beijing Electron-Positron Collider (BEPC) was designed to operate in the τ -charm energy region. Its detectors, Beijing Spectrometer (BES) and the upgraded BESII, were operated from 1989 to 2004 at the Institute of High Energy Physics of the Chinese Academy of Sciences in Beijing. An overview of BEPC is shown in figure 2.1. The BES has many interesting and important physics, including light hadron spectroscopy, charm meson decay properties, charmonium spectrum, Quantum ChromoDynamics (QCD), tau physics, rare decays, and search of glueball etc.

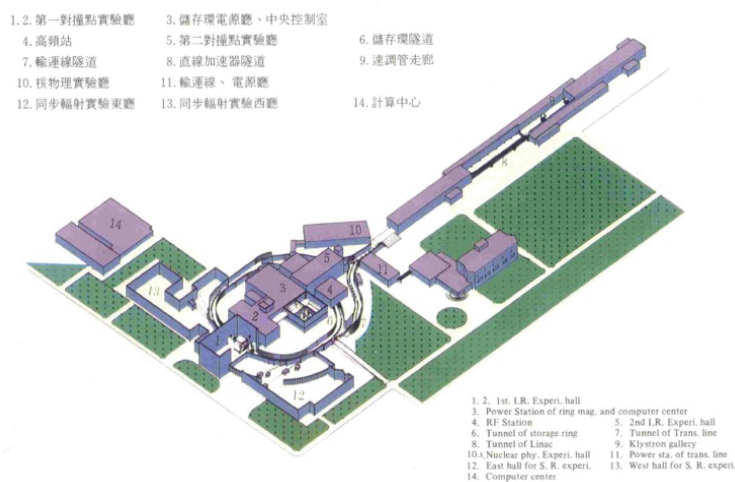


Figure 2.1 An overview of BEPC

There are usually two ways to explore new physics, including by increasing the energy of the particle accelerator to higher level and by improving the precision of measurement at lower energy. A high luminosity accelerator was proposed for the τ -charm energy region in 1980s and only BES still works at this energy region. QCD, an important component of standard model, has been successfully tested by lots of high precision experiments for its validity at the high momentum transfer. But it is difficult to be tested at low energy, especially for the property of glueballs and hybrids, which have not been predicted quantitatively in theory. Although we can obtain reliable predictions of any

strong process from Lattice QCD (LQCD), the calculation of LQCD should be checked and calibrated by high precision measurements.

The upgrade from BEPC/BESII to BEPCII/BESIII is urgent, which will provide an opportunity for us to improve the precision measurement, and will enable us to advance particle physics study substantially. The BEPCII is a multi-bunch collider, high luminosity, which requires a comparable high quality detector with modern detector technology. The existing BESII detector is aging with the time, meanwhile the data acquisition system and electronics of the detector do not support the multi-bunch mode; moreover, a corresponding reduction of systematic errors is proposed with the accumulation of statistics. Therefore, more rigid requirements have been suggested to the modern detector, BESIII:

- Good photon energy resolution and good angle resolution for photon measurement. Crystal calorimeter, such as CsI, is one of the best choices.
- Precise momentum measurement. It is important to minimize the multiple Coulomb scattering.
- Good hadron identification capability. Both Cherenkov detector and Time-of-Flight system can meet our requirements.
- A modern data acquisition system and the front-end electronics system based on the pipeline technique, which can accommodate multi-bunch mode.
- Maximum solid angle coverage($\sim 90\%4\pi\text{Sr}$.)

2.1 BEPCII

The BEPCII is a double-ring multi-bunch collider with a design luminosity of $1 \times 10^{33} \text{ cm}^{-2} \text{ s}^{-1}$ at a center-of-mass energy of $2 \times 1.89 \text{ GeV}$, which installed in the same tunnel as BEPC. The engineering run of BEPCII in collision mode was successfully completed in July of 2008, and physics data taking was started in March of 2009.

Full details of the BEPCII can be found elsewhere^[74,75]. The design goals and the design parameters of BEPCII are summarized in table 2.1 and table 2.2^[75], respectively.

2.2 BESIII

The BESIII, covering 93% of the 4π solid angle, is configured around a 1 Tesla(T) superconducting solenoid (SSM). It consists of Multilayer Drift Chamber (MDC), Time-Of-Flight (TOF) system, ElectroMagnetic Calorimeter (EMC) and Muon identifier (MUON).

Table 2.1 Design goals of the BEPCII

Parameter	Value
Beam energy	1~2.1 GeV
Optimum energy	1.89 GeV
Current of each beam in collision	0.93A
Design Luminosity	$1 \times 10^{33} \text{ cm}^{-2} \text{ s}^{-1}$ @1.89 GeV
Beam lifetime	2.7hrs.
Dedicated synchrotron radiation	250mA@2.5GeV
Injection of linac	positron injection rate: >50 mA/min total energy injection: 1.55~1.89 GeV

Table 2.2 BEPCII design parameters compared with those of BEPC

Parameters	BEPCII	BEPC
Center of mass Energy(GeV)	2 - 4.6	2 - 5
Circumference(m)	237.5	240.4
Number of rings	2	1
RF frequency f_{rf} (MHz)	499.8	199.5
peak luminosity at $2 \times 1.89 \text{ GeV}(\text{cm}^{-2} \text{ s}^{-1})$	$\sim 10^{33}$	$\sim 10^{31}$
Number of bunches	2×93	2×1
Beam current(A)	2×0.91	2×0.035
Bunch spacing(m/ns)	2.4/8	-
Bunch length(σ_z)cm	1.5	~ 5
Bunch width(σ_x) μm	~ 380	~ 840
Bunch width(σ_x) μm	~ 5.7	~ 37
Relative energy spread	5×10^{-4}	5×10^{-4}
Crossing angle(mrad)	± 11	0

Figure 2.2 shows the configuration of BESIII. The expected performance and main parameters of BESIII are listed in table 2.3^[75].

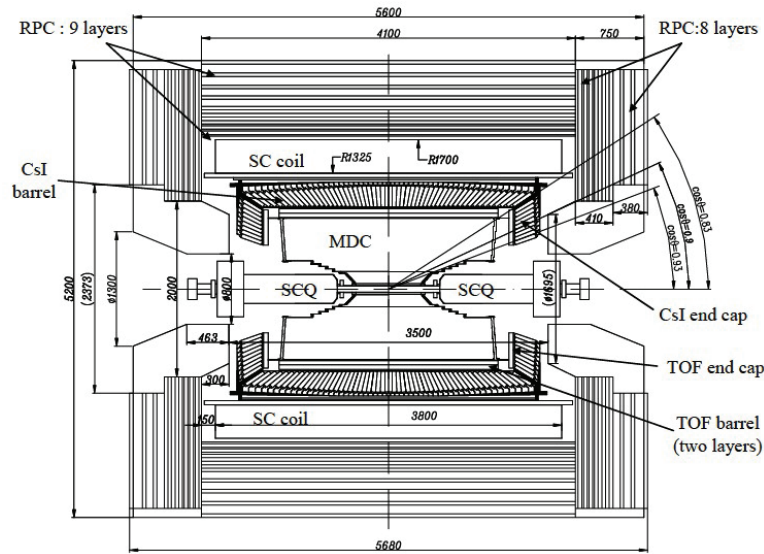


Figure 2.2 Schematic overview of BESIII

2.2.1 Main Drift Chamber

As one of the most important sub-detectors, MDC is the innermost sub-detector of the BESIII detector, which transverse momentum resolution for 1 GeV/c charged particles is 0.5%. The study of Monte Carlo simulation shows that the energy loss ($-dE/dx$) resolution is better than 6% corresponding to 3σ π/K separation up to momentum of ~ 770 MeV/c. The main functions of MDC are listed below:

- Precision momentum measurement. The effects of multiple Coulomb scattering should be minimized in the design.
- Adequate good resolution of dE/dx for particle identification.
- Maximum solid angle coverage ($\sim 90\% 4\pi$ Sr.).
- High reconstruction efficiency for short tracks from interaction point.
- Realization of charged particle trigger at level one.

The charged particle's momentum is measured by their trajectory in a magnetic field. The momenta of most charged particles are smaller than 1 GeV/c at BEPCII, hence, multiple Coulomb scattering will dominate the tracking performance. Therefore, Helium gas mixture and aluminum wires are adopted as working gas and field wires, respectively. The MDC comprises of an outer chamber and an inner chamber. To maximize the polar

Table 2.3 Detector parameters and performance comparison between BESIII and BESII

Sub-detector	Sub-system	BESIII	BESII
MDC	Single wire $\sigma_{r\phi}(\mu\text{m})$	130	250
	$\sigma_p/p(1 \text{ GeV}/c)$	0.5%	2.4%
	$\sigma(dE/dx)$	6%	8.5%
EMC	$\sigma_E/E(1 \text{ GeV})$	2.5%	20%
	Position resolution(1 GeV)	0.6 cm	3 cm
TOF	Barrel(σ_T/ps)	100	180
	End cap(σ_T/ps)	110	350
Muon	No. of layers (barrel/end cap)	9/8	3
	Cut-off momentum (MeV/c)	0.4	0.5
Solenoid magnet Field (T)		1.0	0.4
$\Delta\Omega/4\pi$		93%	80%

angle coverage and to reduce the deformation caused by wire tension in large radius, the end-plate of the outer chamber is designed to be multi-stepped and tilted shape, while that of the inner chamber has a tilt shape. Figures 2.3 shows the schematic of the MDC structure.

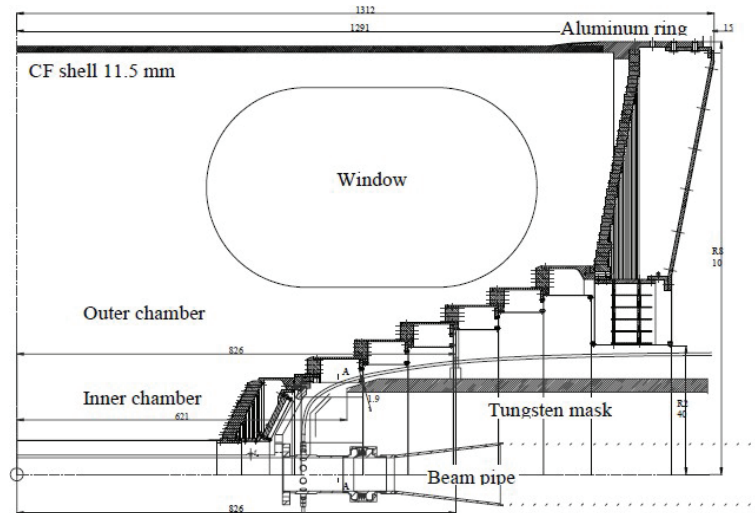


Figure 2.3 The MDC mechanical structure

2.2.2 The Time of Flight

The TOF is installed between MDC and EMC (see figure 2.2), which is a powerful sub-detector for particles identification. This sub-detector includes a double layer barrel and two single layer end caps. The polar angle of the barrel is $|\cos\theta| < 0.83$, and that of the endcaps is $0.85 < |\cos\theta| < 0.95$. The time resolution for $3\sigma \pi/K$ separation to reach 900 MeV with incident angle of 90° is expected to be ~ 100 ps. The cross section of the TOF is shown in figure 2.4. The expected performances of TOF at BESIII are listed in table 2.4, which comes from Monte Carlo studies.

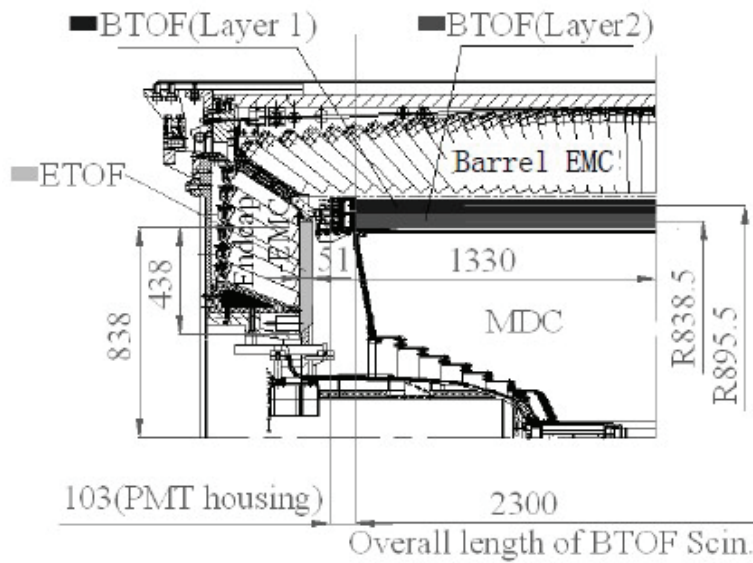


Figure 2.4 Cross-sectional view of one quadrant of the barrel TOF system and the positions of the TOF counters at BESIII

Table 2.4 Comparison of parameters of TOF between BESIII and BESII

Parameters	BESIII	BESII
Polar angle coverage Barrel (Endcap)	$ \cos\theta < 0.83$ ($0.85 < \cos\theta < 0.95$)	$ \cos\theta < 0.64$ (none)
Time resolution for 1 GeV muon Barrel (Endcap)/ps	~ 90 (~ 120)	180 (350)
Inner radius (m)	0.81	1.15
$3\sigma \pi/K$ separation (GeV/c)	< 0.9	< 0.8

A simulated K/π separation capability of barrel TOF at BESIII is shown in figure 2.5. The π/K separation capability depends on the polar angles of tracks. The 3σ π/K separation limit is 0.7 GeV/c at the incident angle of 90° .

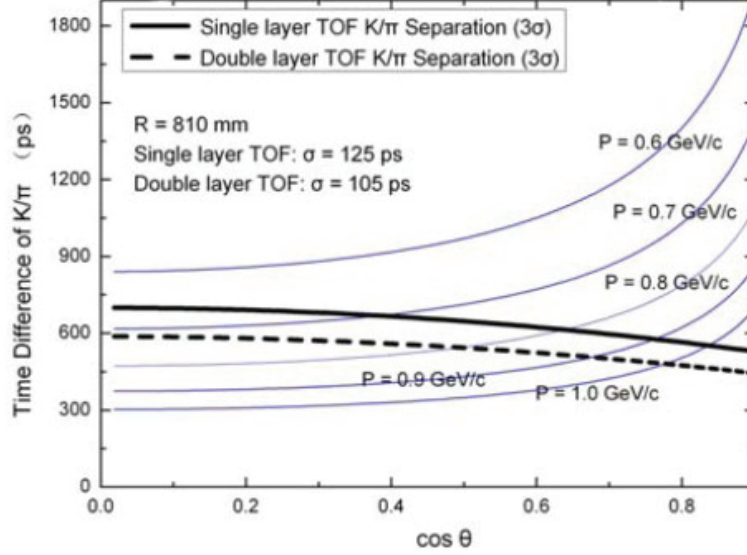


Figure 2.5 K/π separation capability as functions of $\cos \theta$. The thick solid line and thick dashed lines represent the 3σ K/π separation capability corresponding to time resolutions of 125 ps and of 105 ps, respectively.

A likelihood analysis is applied to the calculation of particle identification capability. As figure 2.6 shown, a π/K approximate separation efficiency of 95% and a misidentification of about 5% can be obtained up to 0.9 GeV/c.

2.2.3 Electro-Magnetic Calorimeter

The main functions of EMC (shown in figure 2.7) are high energy resolution and position resolution for photons and electrons. It is important to separate electrons from pions because of the misidentification of pions to electrons due to the interaction between charged pions and CsI crystals. As the radiative decay of J/ψ is considered to be one of the best places for glueball production, moreover these similar decay of charmonium are the main subject of BESIII, it is essential to precisely measure and separate the radiative photons from decays of π^0 , η , ρ etc..

The physics goal of BESIII require that the design of the EMC should be based on CsI(Tl) crystals, the expected performances are listed as below:

- The energy detection range of photon or electron is from 20 MeV to 2 GeV with a approximate energy resolution of $2.5\%/\sqrt{E(\text{GeV})}$ as figure 2.8 (a) shown. It is

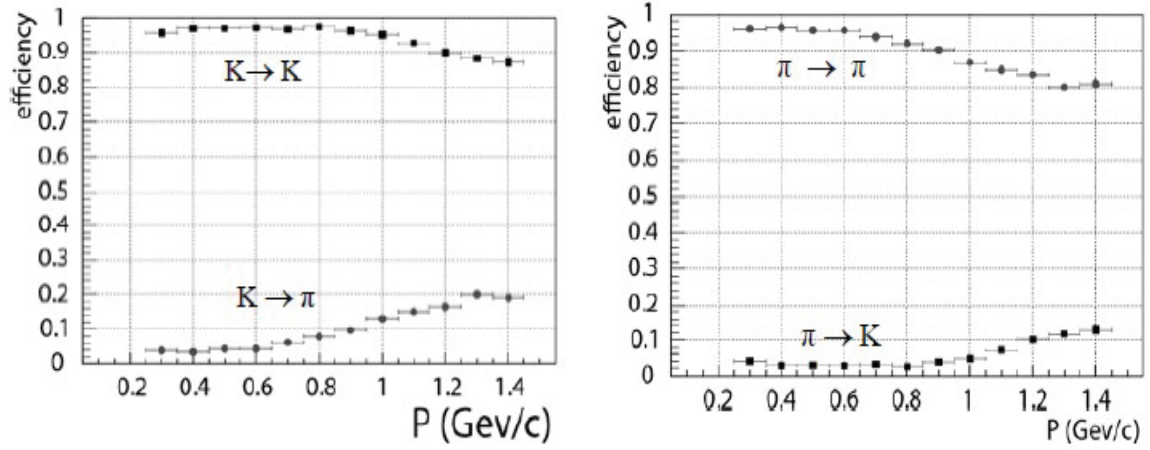


Figure 2.6 π/K separation efficiency and misidentification rate.

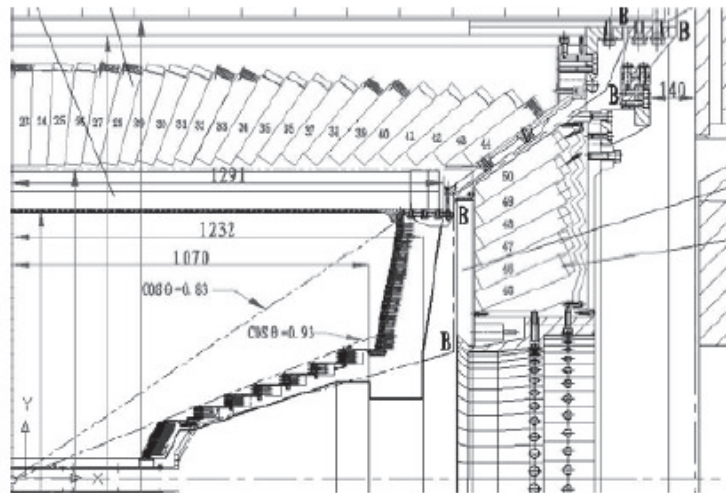


Figure 2.7 Cross-sectional view of one quarter of EMC at BESIII

crucial to obtain good energy resolution especially in the energy region below 0.5 GeV.

- Position resolution of EMC shower is $\sigma_{xy} \leq 6\text{mm} @ / \sqrt{E(\text{GeV})}$ as shown in figure 2.8 (b).
- A good e/π separation in the energy region above 200 MeV.
- Crystals have a fine granularity and signal readout so that the overlapping showers can be reconstructed, especially for high energy π^0 's.
- Providing a neutral(γ) energy trigger.
- The electronics noise for each crystal should be less than 220 KeV.

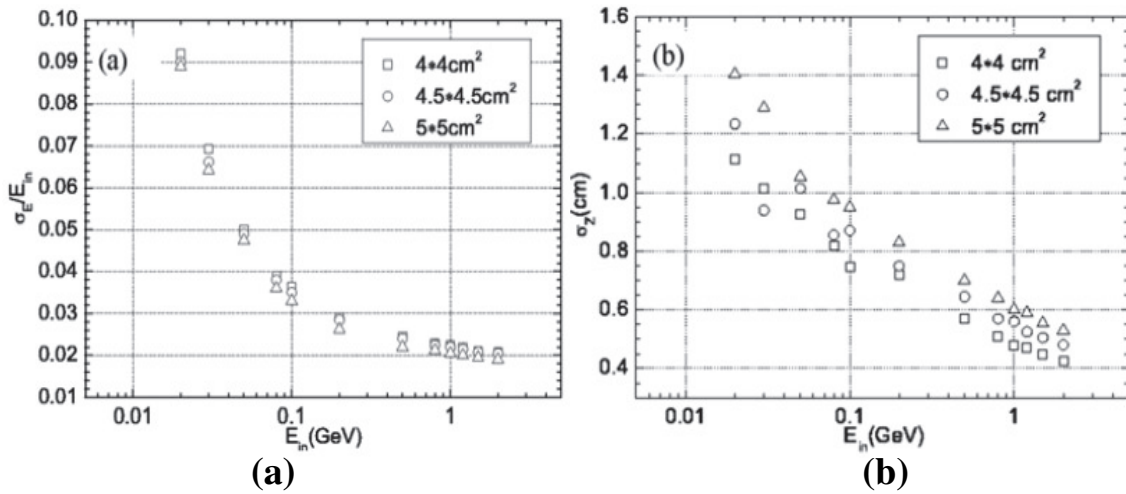


Figure 2.8 Results of Monte Carlo simulation: (a) energy and (b) position resolutions as a function of energy.

2.2.4 Muon Identifier

The muon identifier at BESIII, the outmost subsystem of the BESIII detector, is a gaseous detector based on Resistive Plate Chambers (RPCs) as shown in figure 2.9. The RPC is widely used in many experiment, such as the CMS and ATLAS experiments at LHC, the BELLE experiment at KEK-B, the BaBar experiment at SLAC and so on. RPC is composed of two parallel high resistive plate electrodes with a gap between them for the working gas to pass through as shown in figure 2.10. A signal would be produced when a particle passes through the gas chamber. The function of this sub-detector is to measure the positions and trajectories of muons produced in e^+e^- annihilation. The muon detector consists of endcap (east and west) and barrel. Its coverage of the solid angle is

about $\Omega/4\pi = 0.89$, and the position resolution of a single layer is about 1.2 cm. The comparison of performance parameters between BESIII and BESII can be found in table 2.5.

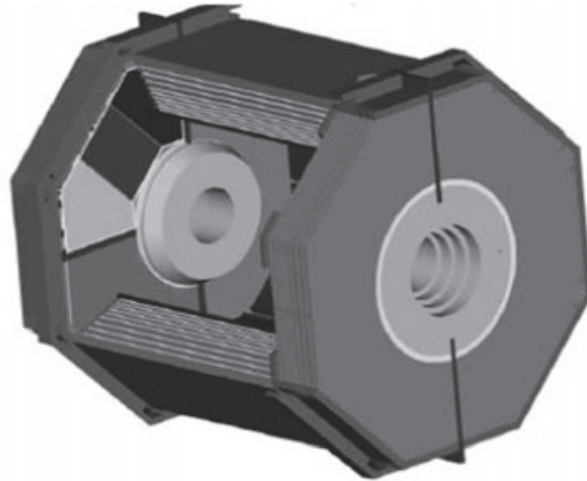


Figure 2.9 The 3D models of the muon identifier at BESIII

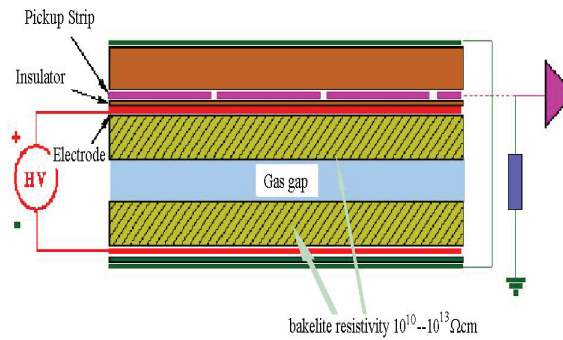


Figure 2.10 The sketch map of RPC structure at BESIII

As figure 2.11 shows, the minimum momentum of muon that can be detected is about 0.4 GeV/c. When the momentum of muon is larger than 0.5 GeV/c, the detection efficiency is determined to be over 90%, while the contamination from pions is about 10%.

Table 2.5 Comparison of parameters of Muon between BESIII and BESII

Parameters	BESIII	BESII
$\Omega/4\pi$	89%	65%
Number of layers (Barrel/Endcaps)	9/8	3
Technology	RPC	Proportional tubes
Cut-off momentum (GeV/c)	0.4	0.5

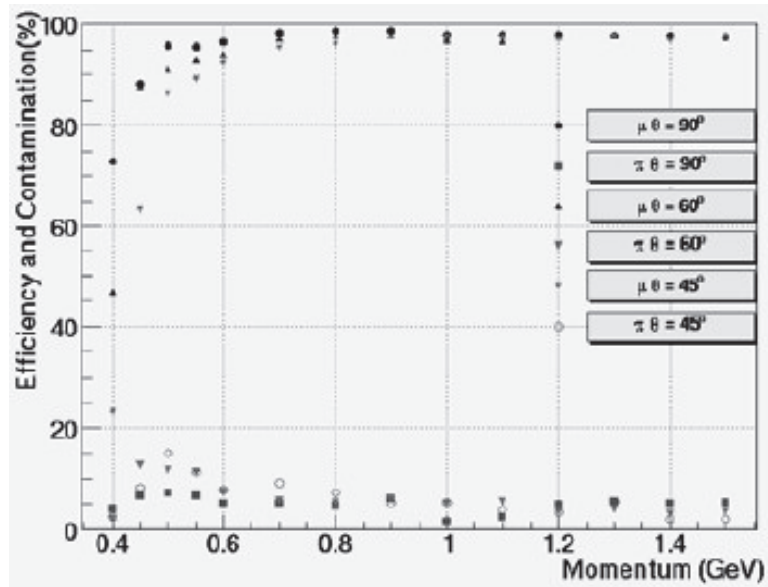


Figure 2.11 The simulated muon identification efficiency and pion contamination rate of Moun at BESIII.

2.3 Trigger

The Level-1 hardware trigger and the Level-2 software trigger (event filter) compose BESIII trigger system. Figure 2.12 shows the data flow diagram at the BESIII. The function of L1 trigger is to reduce the beam related backgrounds and cosmic ray and to select good physics events with high efficiency. The simulated trigger efficiencies for various physics channels and background rejections are given in table 2.6. L2 trigger is used to further suppress background events, and data are eventually written to the permanent storage device. The physics event rate is expected to be 2 kHz (600 Hz) at the J/ψ ($\psi(2S)$) resonance at the peak luminosity of $10^{33}\text{cm}^{-2}\text{s}^{-1}$ [75].

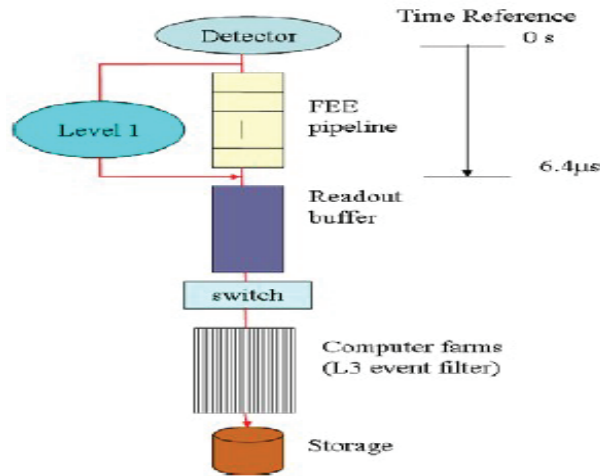


Figure 2.12 Data flow diagram of the L1 trigger at BESIII.

2.4 Data Acquisition

The architecture of DAQ system at BESIII is shown in figure 2.13 [76]. The system includes high performance computers and can be divided into two sub-systems: the front-end system and the online computer farm. High speed optical links, ethernet ports and switches are used to communicate these two systems. The software of DAQ was developed based on the framework of the ATLAS TDAQ software [77].

The comparison of data rates at different stages between BESIII and several major HEP collider experiments are listed in table 2.7. The data rate of BESIII experiment is between the rates of D0 and CMS. The BESIII data acquisition system is designed with a bandwidth of 80 MB/s for reading out data from the VME crates [75].

Table 2.6 Simulated trigger efficiencies for some representative physics channels and background rejection

Processes	Passing fraction (%)
$J/\psi \rightarrow \text{anything}$	97.66%
$\psi(2S) \rightarrow \text{anything}$	99.50%
$J/\psi \rightarrow D\bar{D} \rightarrow \text{anything}$	99.90%
$J/\psi \rightarrow \omega\eta \rightarrow 5\gamma$	97.85%
$J/\psi \rightarrow \gamma\eta \rightarrow 3\gamma$	97.75%
$J/\psi \rightarrow p\bar{p}\pi^0$	97.94%
$e^+e^- \rightarrow e^+e^-$	100%
$e^+e^- \rightarrow \gamma e^+e^-$	100%
Beam related backgrounds	4.6×10^{-3}
Cosmic ray backgrounds	9.4

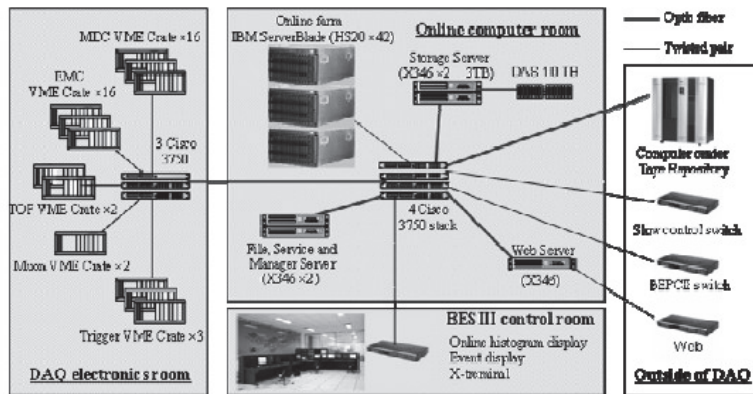


Figure 2.13 DAQ architecture at BESIII.

Table 2.7 Comparison between BESIII and other modern HEP experiments

	BESIII	Belle	D0	CMS	ATLAS
L1 trigger output rate (kHz)	4	0.3	1	100	100
L2 trigger output rate (kHz)	3	0.25	0.05	0.10	0.2
Ratio of L1/L2	1.33	1.2	200	1000	500
Average event size (kB)	14	40	250	1000	1000
Data rate to tape (MB/s)	42	15	12.5	100	200

2.5 Monte Carlo Generators

2.5.1 Introduction

High quality and precise Monte Carlo (MC) generators is not only a challenge for BESIII, but also for the precision measurements at BESIII. It is essential to minimize experimental systematic uncertainties and could be used to determine detection efficiencies and to perform background check. Recently, high-precision generators (e.g. KKMC, Bhlumi etc.) based on Yennie-Frautchi-Suura exponentiation have been developed for the QED processes $e^+e^- \rightarrow f\bar{f}(f : \text{fermion})$ ^[78]. The official ‘precision tags’ of these generators are at the order of 1% or less. Generators that incorporate dynamic information into hadron decays have also been developed, notably EvtGen, which was produced by the BaBar and CLEO collaborations to model B meson decays. These developments provide us with the luxury of being able to choose among the existing generators, which is most suitable for simulating physics processes in the tau-charm threshold region.

2.5.2 Generator framework

KKMC + BesEvtGen is the default generator framework at BESIII, which is used to generate charmonium decays. As shown in figure 2.14, charmonium is produced through e^+e^- annihilation. Before they annihilate into a virtual photon, the incident positrons and electrons could radiate real photons via initial state radiation (ISR). It is crucial to correct these radiative processes in e^+e^- experiments. In order to achieve accurate results, generators for e^+e^- collision must carefully take ISR into account. The KKMC generator is used to simulate $c\bar{c}$ production via e^+e^- annihilation with the inclusion of ISR effects with high precision; it also includes the effects of the beam energy spread. The subsequent charmonium meson decays are generated with BesEvtGen.

2.5.3 BESIII Generators

The generators used at BESIII, includes KKMC, BesEvtGen, QED generators and inclusive generators.

1. KKMC

KKMC^[79,80] is an event generator for the precise implementation of the Electroweak Standard Model formulae for the processes $e^+e^- \rightarrow f\bar{f} + n\gamma$ ($f = \mu, \tau, d, u, s, c, b$) at centre-of-mass energies from the $\tau^+\tau^-$ threshold up to 1 TeV.

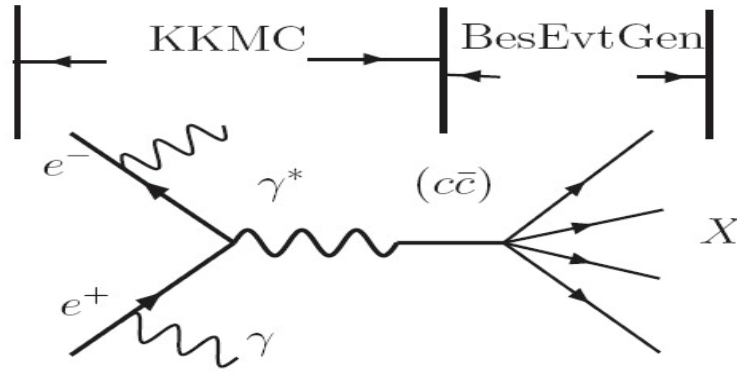


Figure 2.14 Illustration of BESIII generator framework

KKMC was originally designed for LEP, SLC, and is also suitable for future Linear Colliders, b , c , τ -factories etc.. In the BESIII generator framework, KKMC is used to generate charmonium states with the inclusion of ISR effects and the beam energy spread.

2. BesEvtGen

BesEvtGen^[81], developed from EvtGen, is used to simulate tau-charm physics at BESIII. User could create a decay model easily by EvtGen with a interface. The EvtGen interface uses dynamical information to generate a sequential decay chain through an accept-reject algorithm, which is based on the amplitude probability combined with forward and/or backward spin-density matrix information. These spin-density matrices can be calculated automatically with the EvtGen interface.

3. QED generators

There are three QED generators, including Bhlumi, Bhwide, Babayaga.

Bhabha scattering process is simulated by Bhlumi^[82] and Bhwide^[83]. Bhlumi generator and Bhwide generator are suitable for generating low angle ($\theta < 6^\circ$) and wide angle ($\theta > 6^\circ$) Bhabha events, respectively. The ‘suitable’ means that these two generators will achieve the tagged precision level within their suitable region, but the precision will be poorer outside of that region. The precisions of Bhlumi are quoted as 0.11% and 0.25% at the LEP1 energy scale and LEP2 experiments^[82], respectively. The precision of the Bhwide is quoted as 0.3% at the Z boson peak and 1.5% at LEP2 energies.

Babayaga^[84] is applied to generate events for $e^+e^- \rightarrow e^+e^-, \mu^+\mu^-, \gamma\gamma$ and $\pi^+\pi^-$ processes with energy below 12 GeV. It is intended to be a generator for precise luminosity determinations of R measurements in the hadronic resonance region.

The accuracy of Babayaga is quoted as 0.1%^[78]. The current version of BABAYAGA used at BESIII is V3.5^[78].

4. Inclusive generators

In high-energy particle collisions, such as e^+e^- , pp , ep , it is commonly using PYTHIA program to generate inclusive event. The version currently available is PYTHIA 6.4.

A modified Lundcharm model has been accepted by BESIII to simulate J/ψ and $\psi(2S)$ inclusive decays in the BesEvtGen framework. This model has been taken into account C - and G -parity constraints and the comparison with experimental results were performed^[85]. A great advantage of the model is that branching fractions and models for known decays can be specified in the EvtGen decay dictionary, while unknown decays could be generated with the Lundcharm model. User is also allowed to access to the PYTHIA model with the model 'PYCONT' though EvtGen.

Chapter 3 The study of $J/\psi \rightarrow \gamma\eta_c, \eta_c \rightarrow \phi\phi(\omega\phi)$

In this section, The branching fraction measurement for $J/\psi \rightarrow \gamma\eta_c, \eta_c \rightarrow \phi\phi(\omega\phi)$ is presented. The analysis is based on the J/ψ data accumulated by BESIII at BEPCII from June 12th to July 23th 2009, the total number of events is determined to be 225.2 ± 2.8 million(M)^[86]. In addition, 42.6 pb^{-1} data collected at the energy 3.65 GeV from May 26th to June 3rd 2009 is used to estimate the background from QED processes. The BESIII Offline Software System (BOSS) version used to reconstruct data is BOSS 6.5.5. A 225 M inclusive J/ψ MC sample is used to study the background. It is generated with KKMC plus BesEvtGen, and the known branching ratios are fixed to PDG values^[87], while the unknown remainder ratios are generated according to the Lundcharm model^[85].

3.1 $J/\psi \rightarrow \gamma\eta_c, \eta_c \rightarrow \phi\phi, \phi \rightarrow K^+K^-$

3.1.1 Event selection

It is important to set reasonable selection criteria to obtain reliable result. In order to improve the efficiency of selection and to suppress the backgrounds, pre-selections for good photons and charged tracks are applied before the final analysis. A brief introduction to the selections will be presented, and then background will be studied. At last we will analyze the mass spectrum of $\phi\phi$ and the systematic errors.

3.1.1.1 General selection criteria

- Photon

Photon candidates are selected based on information of the EMC detector covering barrel and endcap;

- Angle cut

the angle between the photon and the closest charged track: $D_{ang} > 10^\circ$.

- TDC: [0, 14](in unit of 50 ns)

- Energy

$E_\gamma > 0.025 \text{ GeV}$ for the barrel of EMC ($|\cos\theta| < 0.8$) and $E_\gamma > 0.050 \text{ GeV}$ for the endcap of the EMC ($0.86 < |\cos\theta| < 0.92$)

- Charged tracks

Charged track candidates are selected based on the MDC information, i.e., the polar angle and vertex coordinate, where the vertex is defined as the one reconstructed minus the interaction point.

- polar angle

$$|\cos \theta| < 0.93$$

- Vertex cuts

$|V_z| < 10$ cm, $V_r < 1$ cm, where V_z and V_r are the closest distance of the charged track to the interaction point (IP) in the z direction and in the $x - y$ plane, respectively.

After photons and charged tracks are selected, it is required that the number of good photons must be larger than 1. Figure 3.1 shows a comparison of the number of good photons between MC and data. The distributions of MC and data are in good agreement with each other. For the charged tracks, the number of good tracks reconstructed in MDC must be equal to four with zero net charge.

To improve the resolution and to suppress backgrounds, a 4C-kinematical fit has been imposed on the $J/\psi \rightarrow \gamma K^+ K^- K^+ K^-$ hypothesis by looping over all selected photon candidates. After testing all the combinations, the combination of $\gamma K^+ K^- K^+ K^-$ with the minimum χ^2 value will be taken, and the χ^2 of 4C-kinematical fit must be smaller than 100. The distribution of χ^2 of MC is consistent with data within statistic error as figure 3.1 shows.

3.1.1.2 Final Selection

There are four good charged tracks taken as kaon, and all these tracks will be looped to reconstruct the best combination, which has the minimum value of $\sqrt{|M_{K^+K^-}^1 - M_\phi|^2 + |M_{K^+K^-}^2 - M_\phi|^2}$ where $M_{K^+K^-}^i$ ($i = 1, 2$) stand for the mass of the different combination of these kaons, and $M_\phi = 1.020$ GeV/c². Figure 3.3 shows the scatter plot of $M_{K^+K^-}^1$ versus $M_{K^+K^-}^2$ in data sample, and there are two bands corresponding to the two ϕ 's signals. The ϕ is selected with the requirement $|M_{K^+K^-} - M_\phi| < 0.02$ GeV/c² according to the optimization of $\frac{N_{signal}}{\sqrt{N_{signal} + N_{background}}}$, the backgrounds are estimated from inclusive MC sample. The optimization is shown in figures 3.3. In order to test

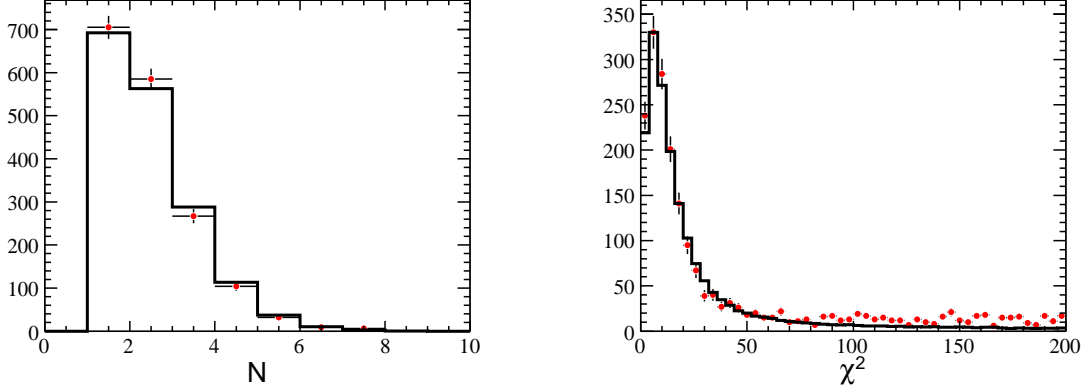


Figure 3.1 The distribution of N_γ and χ^2 for $J/\psi \rightarrow \gamma\eta_c, \eta_c \rightarrow \phi(K^+K^-)\phi(K^+K^-)$. Red dots denote data sample, while black histogram denotes exclusive MC sample. Left: The distribution of number of good photon(N_γ). Right: The distribution of χ^2 .

if the above selection criteria will cause ‘fake’ ϕ signal, the decay channel, $J/\psi \rightarrow \gamma\eta_c, \eta_c \rightarrow K^+K^-K^+K^-$, is generated according to phase space decay model. Figure 3.2 shows the $M_{K^+K^-}$ distribution of the MC sample using the same selections as for data. No peak is seen around the ϕ signal region.

Final event selection criteria are:

- χ^2 of the 4C-kinematic fitting
The $\chi^2 < 100$
- mass window of K^+K^-
 $|M_{K^+K^-} - 1.020| < 0.020 \text{ GeV}/c^2$

3.1.2 Angular distributions

The helicity frame for $J/\psi \rightarrow \gamma\eta_c \rightarrow \gamma\phi\phi \rightarrow \gamma K^+K^-K^+K^-$ is defined as illustrated in figure 3.4.

- For the first decay $J/\psi \rightarrow \gamma\eta_c$

The solid angle $\Omega_0(\theta_0, \phi_0)$ is defined as the opening angle between the momentum direction of η_c and the positron beam in the laboratory system, while the z_0 -axis is taken along as the momentum direction of positron, y_0 -axis is taken along arbitrary direction perpendicular to z_0 -axis, x_0 -axis is taken as the product of y_0 -axis cross

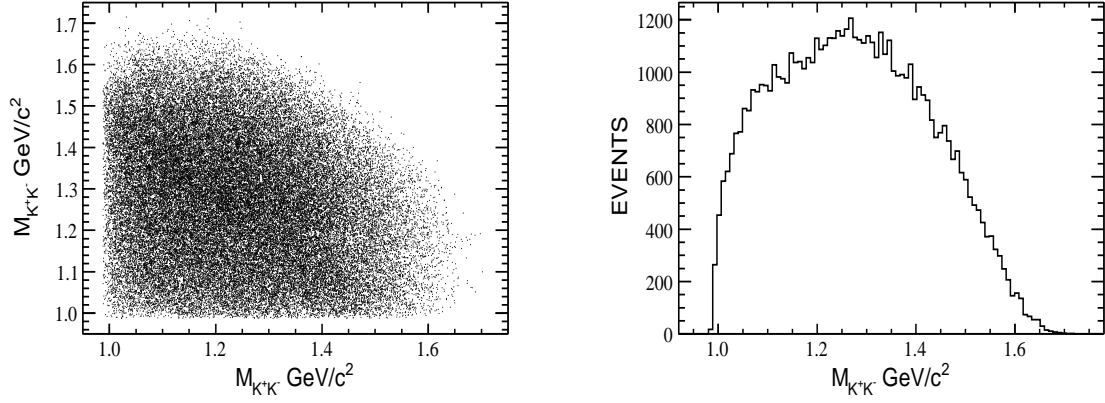


Figure 3.2 The $M_{K^+K^-}$ distribution of MC sample, $J/\psi \rightarrow \gamma\eta_c, \eta_c \rightarrow K^+K^-K^+K^-$. Left: The scatter plot between $M_{K^+K^-}$ and $M_{K^+K^-}$. Right: The distribution of $M_{K^+K^-}$.

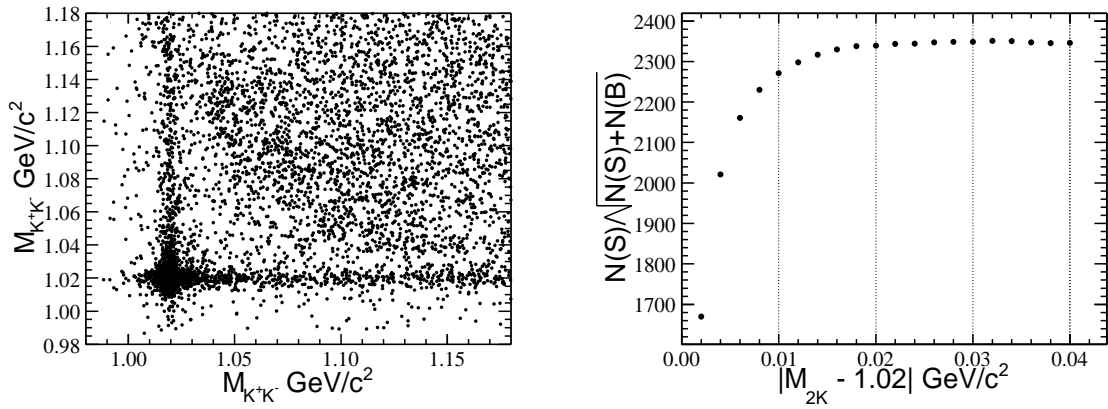


Figure 3.3 The scatter plot between $M_{K^+K^-}$ and $M_{K^+K^-}$ and the optimization of the mass window of $M_{K^+K^-}$. Left: The scatter plot between $M_{K^+K^-}$ and $M_{K^+K^-}$. Right: The optimization of $M_{K^+K^-}$.

z_0 -axis.

- For the second decay $\eta_c \rightarrow \phi\phi$

The z_1 -axis is taken along the outgoing direction of η_c in the J/ψ rest frame, the y_1 -axis is taken as the product of z_0 -axis cross z_1 -axis, while x_1 -axis is taken as the product of y_1 -axis cross z_1 -axis, the solid angles $\Omega_i(\theta_i, \phi_i)(i = 1, 2)$ are the angles of the daughter particles($\phi\phi$) referring to the η_c rest frame.

- For the third decay $\phi \rightarrow K^+K^-$

The z_2 -axis is defined as one of the two ϕ 's outgoing direction in η_c rest frame, the y_2 -axis is taken as the product of z_1 -axis cross z_2 -axis, while the x_2 -axis meets the right-hand assumption. The frame of the other ϕ has similar definition, and the solid angles $\Omega_i(\theta_i, \phi_i)(i = 3, 4)$ are the outgoing direction of kaons in their mother's rest frame.

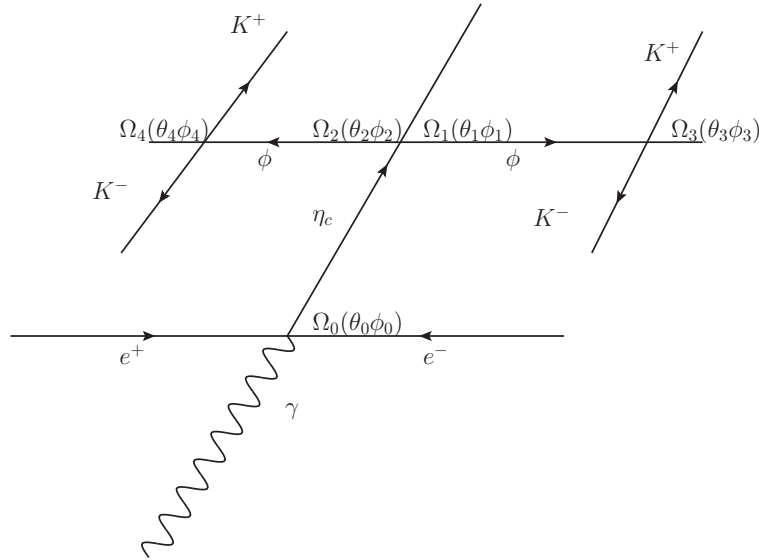


Figure 3.4 The definition of the helicity frame for $J/\psi \rightarrow \gamma\eta_c, \eta_c \rightarrow \phi(K^+K^-)\phi(K^+K^-)$.

The joint angular distribution reads:

$$\begin{aligned} \frac{d\sigma}{d\Omega} \propto & \sum_{\lambda_1, \lambda_2, \lambda_5(\lambda'_5), \lambda_6(\lambda'_6)} |F_{\lambda_1, \lambda_2}^{J_1} D_{M_1, \lambda_1 - \lambda_2}^{J_1*}(\Omega_0) [\sum_{\lambda_3, \lambda_4} B_{\lambda_3, \lambda_4}^{J_2} D_{M_2, \lambda_3 - \lambda_4}^{J_2*}(\Omega_1) \\ & \times E_{\lambda_5, \lambda_6}^{J_3} D_{M_3, \lambda_5 - \lambda_6}^{J_3*}(\Omega_3) H_{\lambda'_5, \lambda'_6}^{J_3'} D_{M'_3, \lambda'_5 - \lambda'_6}^{J_3'*}(\Omega_4)]|^2 \end{aligned} \quad (3-1)$$

where J_i denote the spin of J/ψ , η_c , $\phi(\phi)$ meson pair for $i = 1, 2, 3(3')$, respectively. $\lambda_1(\lambda_2)$ and $\lambda_3(\lambda_4)$ are the helicity values for $\gamma(\eta_c)$ and $\phi(\phi)$ meson. λ_5 and λ_6 are the helicity values of K^+ and K^- from ϕ meson, while λ'_5 and λ'_6 have the similar meaning

but their mother is the other ϕ meson. F , B , E and H are the helicity amplitudes of $J/\psi \rightarrow \gamma\eta_c, \eta_c \rightarrow \phi\phi, \phi \rightarrow K^+K^-$ and the other ϕ decay into K^+K^- .

The angular distributions of different particles in their mother's frames are obtained:

$$\frac{d\sigma}{d\cos\theta_0} \propto 1 + \cos^2\theta_0 \quad (3-2)$$

$$\frac{d\sigma}{d\cos\theta_i} \propto 1 - \cos^2\theta_i \quad (i = 3, 4) \quad (3-3)$$

$$\frac{d\sigma}{d\phi_3 d\phi_4} \propto 1 - \cos^2(\phi_3 + \phi_4) \quad (3-4)$$

Equations (3-2) and (3-3) indicate angular distributions of η_c and K^\pm in the J/ψ and ϕ helicity frame. Equation (3-4) indicates the spin-correlation between two ϕ s in the η_c helicity frame, which could be used to identify the spin parity of η_c ($J^P = 0^-$)^[58,88].

The helicity amplitude information is modeled in the event generator model HELAMP. Figure 3.5 shows the comparison of various angular distributions between data and MC. One can see that the angular distributions of selected data are in good agreement with MC distributions.

3.1.3 Background study

The background is studied with the inclusive MC sample. Table 3.1 shows the main backgrounds in the fitting range, from 2.70 GeV/c² to 3.10 GeV/c². According to the analysis, the surviving background contributions after applying the previously discussed selection criteria are mainly from $J/\psi \rightarrow \gamma\phi\phi$ and $J/\psi \rightarrow \gamma\eta(2225) \rightarrow \gamma\phi\phi$. Both of these decay channels have the same final states as the signal channel, fortunately, both of them are flat in the mass range of interest.

The potential peaking background comes from $J/\psi \rightarrow \gamma\eta_c(\phi K^+K^-)$. The non- ϕ backgrounds are estimated using the sideband boxes as indicated in figure 3.6, where the boxes A, B, C and D are defined as:

- $\phi\phi$ signal range(Zone A)
 $|M_{K^+K^-} - 1.02| < 0.02\text{GeV}/c^2$
- $\phi(K^+K^-)K^+K^-$ range(Zone B)
 $|M_{K^+K^-}^x - 1.080| < 0.020\text{ GeV}/c^2, |M_{K^+K^-}^y - 1.020| < 0.020\text{ GeV}/c^2$
- $\phi(K^+K^-)K^+K^-$ range(Zone C)
 $|M_{K^+K^-}^x - 1.020| < 0.020\text{ GeV}/c^2, |M_{K^+K^-}^y - 1.080| < 0.020\text{ GeV}/c^2$

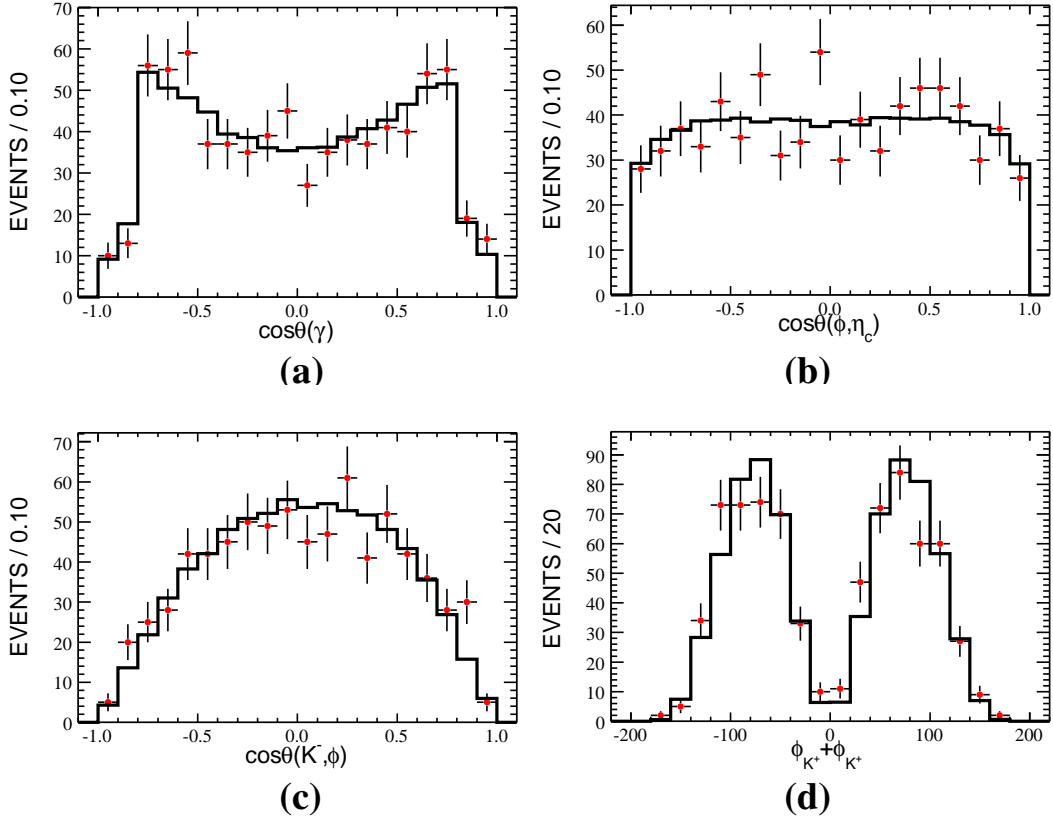


Figure 3.5 The helicity angular distribution of each particle in its mother rest frame. The red dots are data, and the black histogram is MC. (a) The helicity angular distribution of γ in J/ψ rest frame. (b) The helicity angular distribution of ϕ meson in η_c rest frame. (c) The helicity angular distribution of Kaon in ϕ rest frame. (d) The azimuthal angle of K^+ plus that of the other K^+ in their mother's rest frame.

Table 3.1 Summary of the main backgrounds in the mass range of interest

Type of decay channel	Decay chain	N_{event}
	$J/\psi \rightarrow \gamma\phi(K^+K^-)\phi(K^+K^-)$	1910
$J/\psi \rightarrow \gamma K^+K^-K^+K^-$	$J/\psi \rightarrow \gamma\eta_{2225}(\phi\phi)$	114
	$J/\psi \rightarrow \gamma\eta_c(\phi K^+K^-)$	19
	$J/\psi \rightarrow \gamma\phi(K^+K^-)K^+K^-$	12
$J/\psi \rightarrow \pi^0 K^+K^-K^+K^-$	$J/\psi \rightarrow f_{1420}(\pi^0 K^+K^-)\phi(K^+K^-)$	38
	$J/\psi \rightarrow \phi(K^+K^-)K^{*+}(K^+\pi^0)K^-$	8
	$J/\psi \rightarrow f_{1285}(\pi^0 K^+K^-)\phi(K^+K^-)$	7
	$J/\psi \rightarrow \phi(K^+K^-)K^{*-}(K^-\pi^0)K^-$	5
	$J/\psi \rightarrow \pi^0 K^+K^-K^+K^-$ (including other resonances)	4

- $K^+K^-K^+K^-$ range(Zone D)
 $|M_{K^+K^-}^x - 1.080| < 0.020 \text{ GeV}/c^2, |M_{K^+K^-}^y - 1.080| < 0.020 \text{ GeV}/c^2$
- the index x and y denote the x-axis and y-axis, respectively.

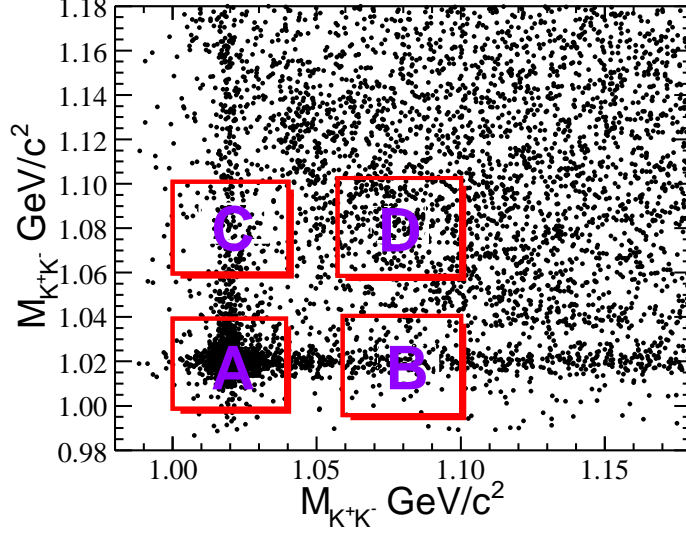


Figure 3.6 Two dimensional invariant-mass plot within the mass range of $\phi\phi$ (from $2.70 \text{ GeV}/c^2$ to $3.10 \text{ GeV}/c^2$). Both of the two axis denote the invariant mass of K^+K^- .

The panels in figure 3.7 show the distributions of the invariant-mass of 4 kaons corresponding to the selected regions shown in box A, B, C and D as labeled in figure 3.6, from which one can see that the distribution of $M_{2(K^+K^-)}$ is not flat. This implies that the normalization of sideband can not be simply scaled with the box area. So we will use MC information to scale the number of events in the sideband to the signal region. In order to obtain the scale factor, two main backgrounds, $J/\psi \rightarrow \gamma\eta_c \rightarrow \gamma\phi(K^+K^-)K^+K^-$ and $J/\psi \rightarrow \gamma\eta_c(K^+K^-K^+K^-)$, will be produced according to their branching fractions. Figures 3.8 show the $K^+K^-K^+K^-$ invariant mass distribution of MC sample in different mass region. The number of events in each box is listed in table 3.2. Using the scaled factors determined from MC sample, the number of backgrounds is estimated to be $\frac{1}{2}(102 \times \frac{1476}{1144} + 107 \times \frac{1476}{1152}) = 134$.

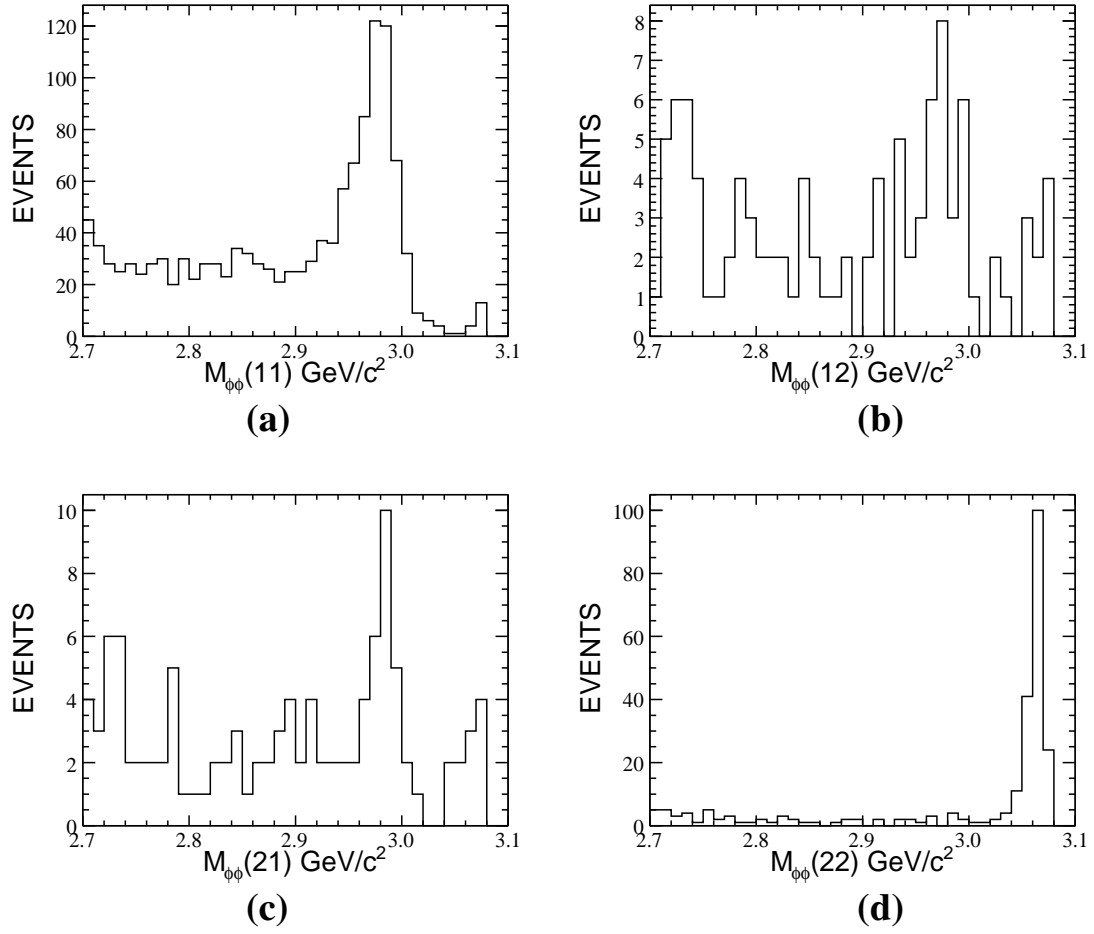


Figure 3.7 Invariant mass of $K^+K^-K^+K^-$ in different mass region of experimental data. The event number of boxA, boxB, boxC and boxD is 1276, 102, 107 and 245, respectively.

Table 3.2 Number of events corresponding to four regions(A, B, C, D) in figure 3.8

Zone	A	B	C	D	Normalized
Number of event	1476	1144	1152	177	134
Scale factor		$\frac{1476}{1144}$	$\frac{1476}{1152}$		

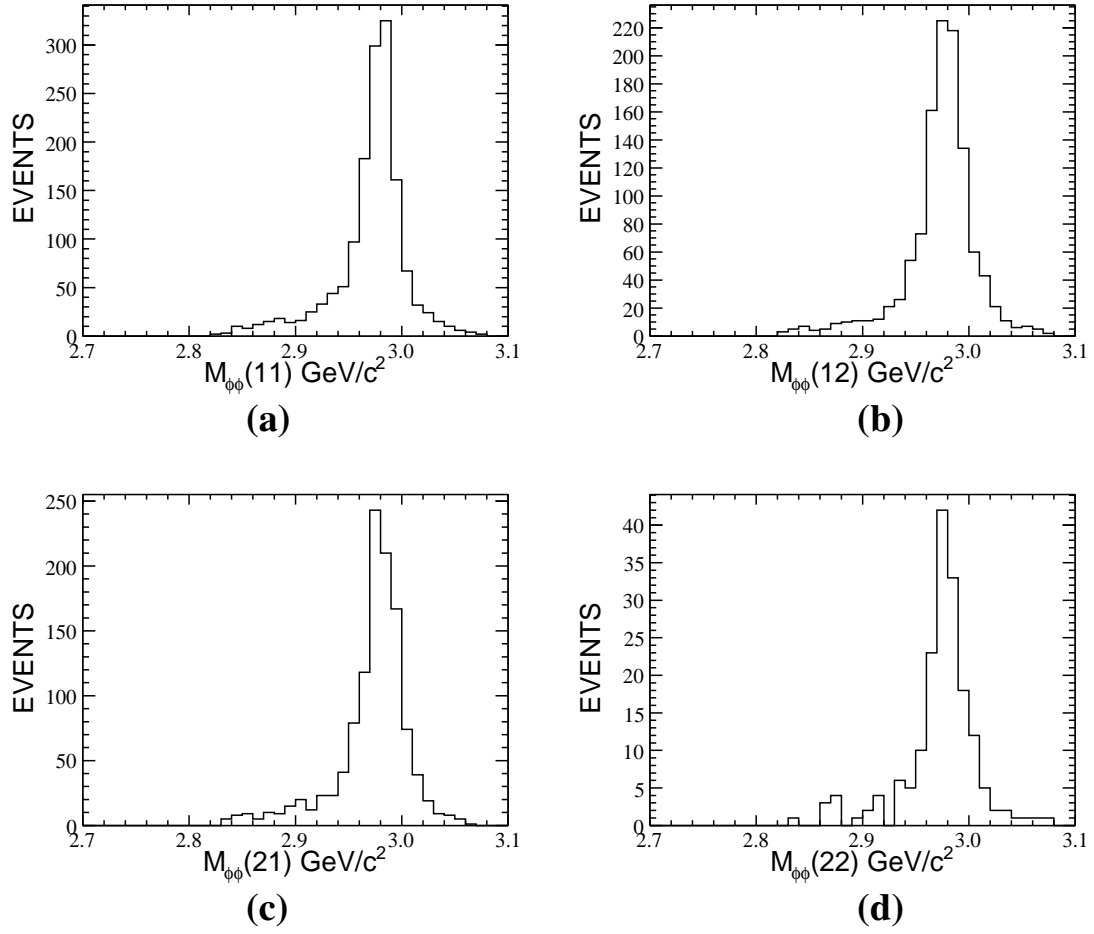


Figure 3.8 Invariant mass of $K^+K^-K^+K^-$ in different mass region of MC sample. The event number of boxA, boxB, boxC and boxD is 1476, 1144, 1152 and 177, respectively.

3.1.4 Fitting of the mass spectrum

3.1.4.1 Input-output check on the branching fraction

We performed an input-output check using the inclusive MC sample of 225 M J/ψ . The event selection criteria are the same as applied to the data sample. As the interference among different decay channels has not been considered, the signal is described by a Breit-Wigner function, while the background is described by a 2nd-order Chebychev function. With this fitting method, the number of observed events is found to be 519 ± 41 . The detection efficiency is determined to be 25.94%, the input branching fraction is $\text{Br}(\eta_c \rightarrow \phi\phi) = 2.7 \times 10^{-3}$. With the input branching fractions of $\text{Br}(J/\psi \rightarrow \gamma\eta_c) = 1.3\%$, $\text{Br}(\phi \rightarrow K^+K^-) = 49.2\%$, the output value of the branching fraction is $\text{Br}(\eta_c \rightarrow \phi\phi) = (2.82 \pm 0.22) \times 10^{-3}$, which is consistent with the input value within the statistical error. Figure 3.9 is the fitting result.

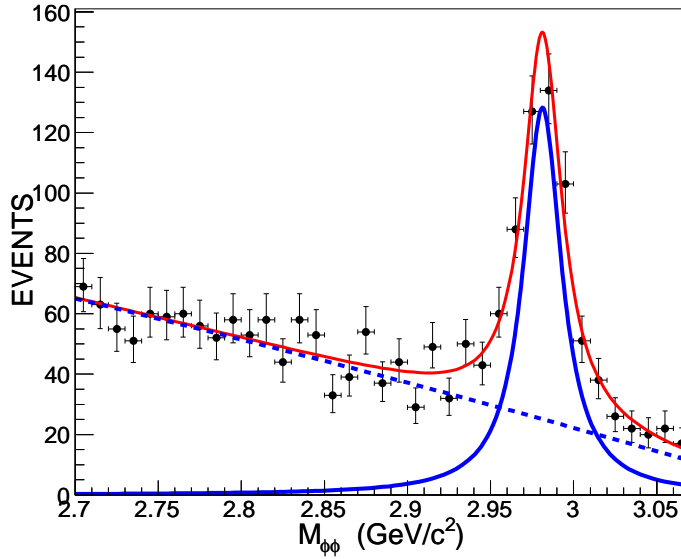


Figure 3.9 Fitting result of $M_{\phi\phi}$ for inclusive sample.

3.1.4.2 Fitting data

To extract the η_c signal events, a spin-parity analysis is applied to fit data event by event, which is similar to that commonly used in the partial wave analysis (PWA). The details are given in Appendix B.1. The probability distribution function is constructed using the helicity amplitude for the signal mode $J/\psi \rightarrow \gamma\eta_c \rightarrow \gamma\phi\phi$ and direct 3-body mode $J/\psi \rightarrow \gamma\phi\phi$, together with the non- ϕ backgrounds. Because we intend to extract the

signal decay using the events within the range of $2.70 \text{ GeV}/c^2 < M_{\phi\phi} < 3.10 \text{ GeV}/c^2$, the direct decay is here defined as the mixture mode including $J/\psi \rightarrow \gamma J^P \rightarrow \gamma\phi\phi$, where J^P denotes the non- η_c resonances. The possible non- η_c resonances may include the state with $J^P = 0^-, 0^+$ and 2^+ . For example, the candidates of non- η_c resonances include $\eta(2225)$, $f_0(1710)$ and $f_2(2340)$, and so on. Because under the η_c signal region, the line-shape of non- η_c resonance is smooth, we exclude the Breit-Wigner function for these non- η_c resonances, and their amplitudes are constructed only requiring the $\phi\phi$ -system having the quantum number $J^P = 0^+, 0^-$ and 2^+ . The potential interference among the signal and the non- η_c resonances are included in the amplitude to account for the η_c anomalous line shape observed by the CLEOc and BESIII collaboration^[89], recently. The background events are estimated with the ϕ -sideband as described in the previous section. Then the backgrounds are subtracted in the likelihood of the data. Here the non- ϕ background events do not interfere with the mode $J/\psi \rightarrow \gamma\phi\phi$. The mass and width of η_c have been fixed to the values ($M_{\eta_c} = 2.984 \text{ GeV}/c^2$, $\sigma_{\eta_c} = 0.032 \text{ GeV}/c^2$) measured by BESIII^[90]. Figure 3.10 shows the fitted results.

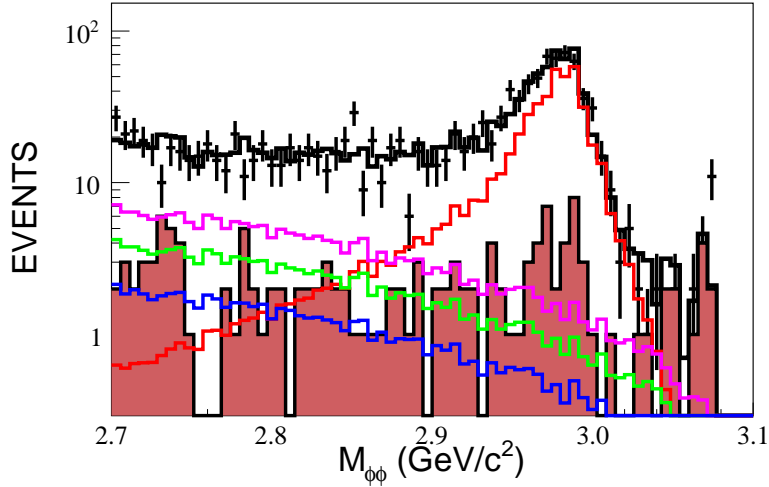


Figure 3.10 Fit results of mass spectrum $M_{\phi\phi}$ of the data. The black dots with error bars denote the data, the black histogram denotes the total fitting result, the red histogram is the η_c signal mode, the histogram with dark red shadow is the contribution from background events estimated with ϕ -sideband around the signal region, the light blue histogram, the pink histogram and the green histogram denote contributions from the non- η_c resonance decay with the quantum number of $J^P = 2^+, 0^+, 0^-$ for the $\phi\phi$ -system, respectively.

The number of signal event yielded from the fit is 494_{-28}^{+23} . The statistical errors are derived from the $S = -\ln \mathcal{L}$ (see Appendix B.1) distribution versus the number of fitted

events; one standard deviation corresponds to the interval that produce a change of log-likelihood of 0.5. The S -distribution for the number of η_c events is given in figure 3.11.

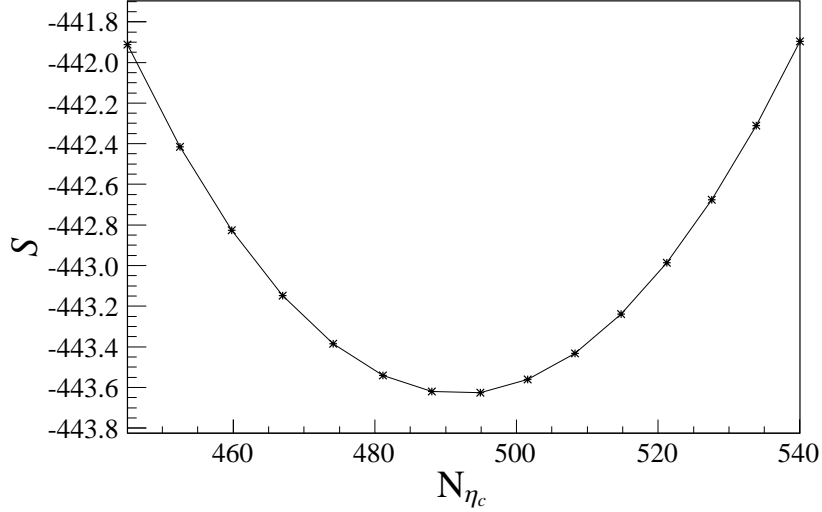


Figure 3.11 The S -distributions of the data, where $S = -\ln \mathcal{L}$.

3.1.4.3 Fit goodness

The goodness of the global fit is determined by calculating a χ^2_{all} defined by

$$\chi^2_{\text{all}} = \sum_{j=1}^5 \chi_j^2, \text{ with } \chi_j^2 = \sum_{i=1}^N \frac{(N_{ji}^{DT} - N_{ji}^{Fit})^2}{N_{ji}^{Fit}}, \quad (3-5)$$

where N_{ji}^{DT} and N_{ji}^{Fit} are the number of events in the i -th bin for the distribution of the j -th kinematic variable. If the measured values N_{ji}^{DT} are sufficiently large, then the χ^2_{all} statistic follows the χ^2 distribution function with the number of degrees of freedom (ndf) equal to the total number of bins in histograms ^① minus the number of fitted parameters; and the individual χ_j^2 gives a qualitative measure of the goodness of the fit for each kinematic variable.

For the 3-body decay $J/\psi \rightarrow \gamma\phi\phi$, there are 5-independent variables, which are selected as the mass of the $\phi\phi$ system ($M_{\phi\phi}$), the mass of the $\gamma\phi$ system ($M_{\gamma\phi}$), the polar angle for the γ (θ_γ), the polar angle for the ϕ (θ_ϕ), and the azimuthal angle for the ϕ (ϕ_ϕ), where the angles are defined in the J/ψ rest frame. Figure 3.12 compares the $M_{\gamma\phi}$

① In a histogram, bins with event entries less than 10 are combined as one bin.

distribution and angular distributions between the best fit solution and the data, and a good agreement can be observed. A sum of all these χ_j^2 values gives $\chi_{\text{all}}^2 = 207.22$, and the total number of degrees of freedom ($ndf = 189$) is taken as the sum of the total number of bins having non-zero events minus the total number of parameters in the PWA fit. The global fit goodness (χ_{all}^2/ndf) is 1.10.

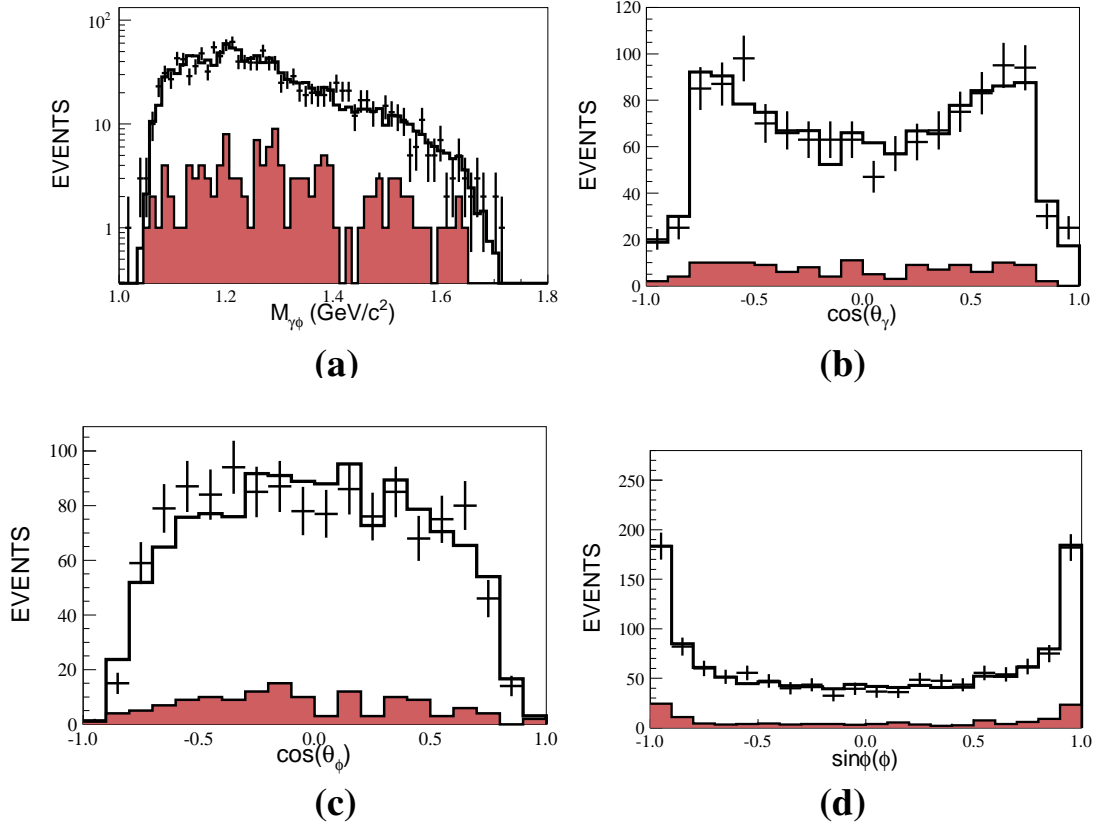


Figure 3.12 Fit results of the data, (a) the mass distributions of $M_{\gamma\phi}$, (b) the photon helicity angle distribution ($\cos \theta_\gamma$), (c) the helicity angle ($\cos \theta_\phi$) distribution for ϕ mesons, and (d) the helicity angle $\sin \phi(\phi)$ for ϕ mesons. In plots, the dots with error bars are the data, and the line histograms are the total fit results, and the shaded histograms are the backgrounds estimated with the ϕ sidebands.

3.1.5 Source of systematic error

The sources of systematic errors include the items listed below:

- Total number of J/ψ ,
- Photon reconstruction,

- Tracking Efficiency for K,
- 4C Kinematic Fitting,
- Branching fraction of $J/\psi \rightarrow \gamma\eta_c$,
- Branching fraction $\phi \rightarrow K^+K^-$,
- Mass(K^+K^-),
- Fitting method.

3.1.5.1 Total number of J/ψ

The error of the total number of J/ψ is 1.24%^[86].

3.1.5.2 photon reconstruction

One of the systematic errors is due to the difference of photon efficiency between MC and data. 1%^[91] will be used as the uncertainty.

3.1.5.3 Tracking Efficiency for kaon

The uncertainty of kaon tracking have been extensively studied at BOSS655^[92]. 1%^[92] will be used as the value of the systematic error of each kaon tracking.

3.1.5.4 4C Kinematic Fitting

We use a method of track parameter correction to estimate the uncertainty from kinematic fitting. A conventional method to estimate the error is dependent on the selection of control samples. However, it is difficult to find an appropriate reference mode with the similar final states and momentum distribution. In addition, it is difficult to obtain a high purity control sample not using kinematic constraints or selection criteria correlated with kinematic constraints, such as total energy, total momentum and so on. In order to estimate the uncertainty from the kinematic fitting, we try to correct the track helix parameters to narrow the gap between MC and data. In other words, it is independent on the decay channel, but relies on the track information. We choose $J/\psi \rightarrow \phi K^+K^-$ as our control sample to exact the correction factors of kaons from their pull distributions. The detailed information on this method is described in Appendix A.1.1.

Table A.1 shows the correction factors. The MC sample after correction are used to estimate the efficiency and fit the invariant mass spectrum. Figures 3.13 show the distribution of χ^2 between MC and data. As the plots shows, the difference between MC

and data reduced obviously but still exist because of the imperfect correction. Half of the difference of efficiency between before ($\varepsilon_1 = 25.94 \pm 0.06$) and after ($\varepsilon_2 = 25.89 \pm 0.06$) correction is taken as the systematic error of efficiency for 4C kinematic fitting as a conservative estimation, which is determined to be 0.10% ($\frac{|\varepsilon_1 - \varepsilon_2|}{2\varepsilon_2}$).

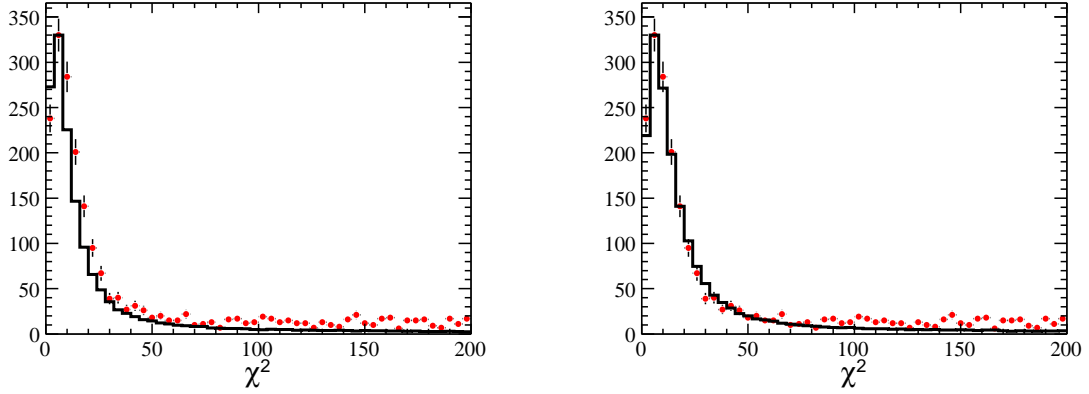


Figure 3.13 A comparison of χ^2 distribution between MC and data. The red dots are data, the black histogram represent MC. Left: Before correction. Right: After correction.

3.1.5.5 Branching fraction of $J/\psi \rightarrow \gamma\eta_c$

According to PDG2012, the uncertainty in the branching fraction of $J/\psi \rightarrow \gamma\eta_c$ is 23.53% ^[10].

3.1.5.6 Branching fraction of $\phi \rightarrow K^+K^-$

According to PDG2012, the uncertainty in the branching fraction of $\phi \rightarrow K^+K^-$ is 1.02% ^[10].

3.1.5.7 Mass window cut on the invariant mass of the two kaons

The previously discussed invariant-mass cut on K^+K^- is applied to select the two ϕ s. Uncertainties due to this requirement arise if the observed ϕ line shape in data is not consistent with that in MC. The consistency of the observed ϕ line shape is studied with the control data sample $\psi(2S) \rightarrow \gamma\chi_{cJ}, \chi_{cJ} \rightarrow \phi\phi$ ($J=0,1,2$).

The general selection for the good charged tracks and good photons are the same as used in data selection. In order to obtain this signal sample as pure as possible, a 4C-kinematic fitting is imposed on the $\psi(2S) \rightarrow \gamma K^+ K^- K^+ K^-$ hypothesis by looping all the selected photons candidates. The combination of $\gamma K^+ K^- K^+ K^-$ with a minimum χ^2 is finally taken. The selection criteria are listed below:

- Number of good photons
The number of good photons must be larger than 1, but must be smaller than 10.
- χ^2
The χ^2 of the 4C-kinematic fitting must be smaller than 100;
- Mass of $K^+ K^-$
restraining one of the two combination with $|M_{K^+ K^-} - 1.020| < 0.020 \text{ GeV}/c^2$, and the other one is floated.
- Mass of $\phi\phi$
 $M_{\phi\phi}, [3.40, 3.60] \text{ GeV}/c^2$

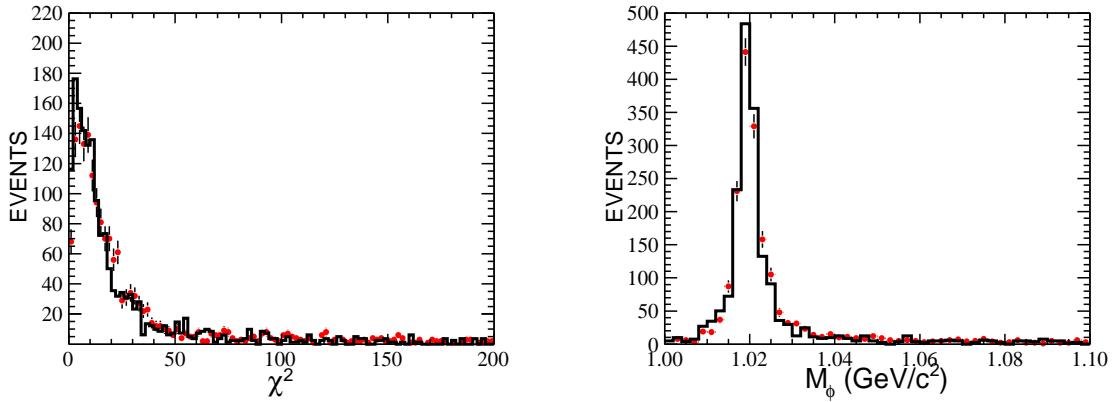


Figure 3.14 The comparison between data and MC. Left: The χ^2 of 4C kinematic fitting. Right: The mass spectrum of $M_{K^+ K^-}$.

As figure 3.14 and figure 3.15 show, a high purity of the channel can be obtained applied these selections. According to inclusive MC sample, the purity is up to 99%. Figures 3.16 show the comparison of $\phi\phi$ mass distributions between MC and data. And the uncertainty due to the mass window selection is found to be 0.71%.

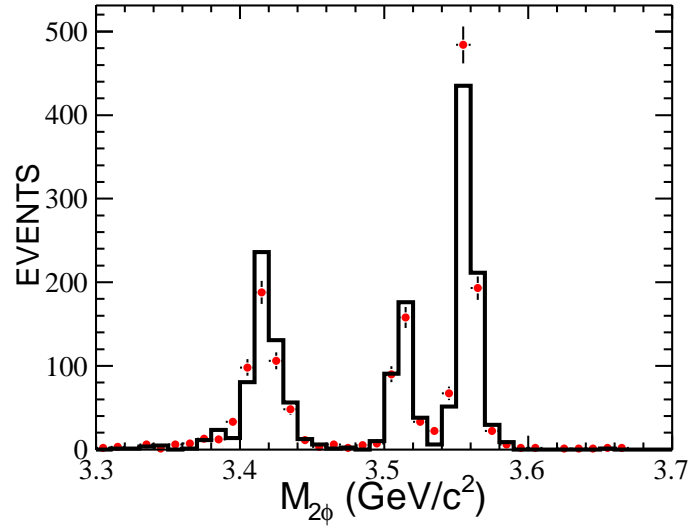


Figure 3.15 The mass spectrum of $\phi\phi$. The red error bars are data results, the black histograms are the MC results.

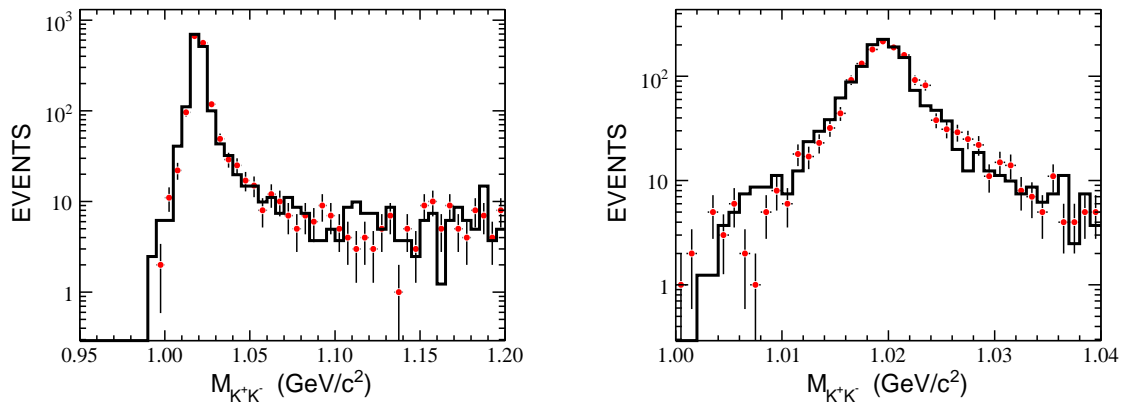


Figure 3.16 The comparison of $M_{K^+K^-}$ between data and MC. Left: Before applying the mass window selection. Right: After applying the mass window selection.

3.1.5.8 Fitting method

An uncertainty of fitting method is due to the uncertainty of non- η_c line shape, which is described with the non- η_c resonances with quantum number $J^P = 0^-, 0^+, 2^+$. As done in the partial wave analysis, the contribution from a state with a minimum statistical significance is counted as the systematic error. We check the statistical significance for each J^P state, and find that the state with $J^P = 0^+$ has the minimum value of statistical significance. So the uncertainty of fitting method is taken as the difference in the η_c signal yield obtained with and without the non- η_c state with $J^P = 0^+$. Figure 3.17 shows the fitting result obtained without the non- η_c state with $J^P = 0^+$. Figure 3.18 shows the scanning result of the number of signal η_c event, which gives the η_c yield of 426^{+23}_{-27} . So the uncertainty is determined to be 13.76%.

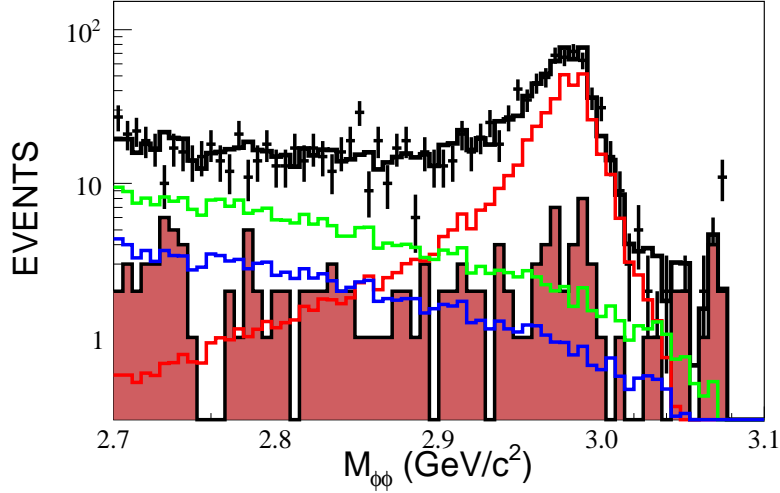


Figure 3.17 Fit results of mass spectrum $M_{\phi\phi}$ for the data. The black dots with error bars denote the data; the black histogram denotes the total fit result; the red histogram is the signal η_c mode; the histogram with dark red shadow denotes non- ϕ backgrounds estimated with ϕ sideband around the signal region; the blue histogram and the green histogram are the contributions from non- η_c resonance with $J^P = 2^+, 0^-$, respectively.

3.1.5.9 Summary of systematic errors

According to above analysis, table 3.3 summarizes these systematic errors.

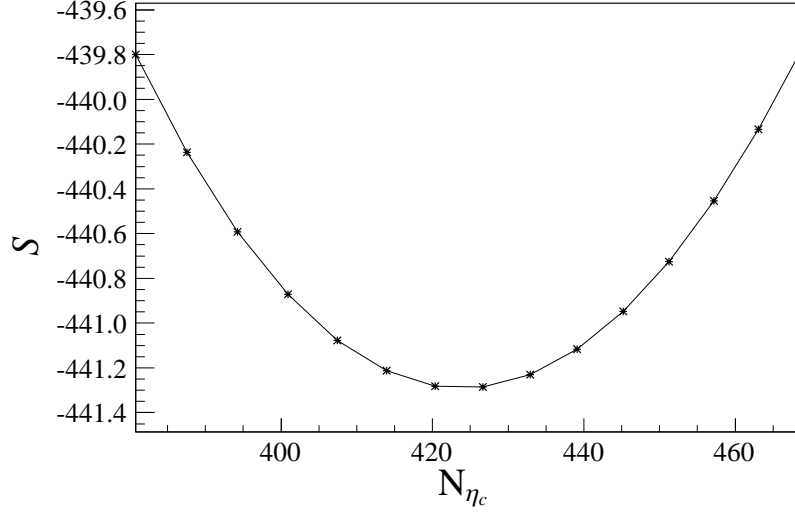

 Figure 3.18 The S – distributions of the data, where $S = -\ln \mathcal{L}$.

Table 3.3 Summary of systematic errors(%)

Source	Error(%)	Comment
$N_{J/\psi}$	1.24	Chin.Phys.C 36 , 915-925(2012)
Tracking	1.00×4	Chen Y. et al., DAQ meeting
Photon	1.00	Phys. Rev. D 83 , 112005(2011)
$B_r(J/\psi \rightarrow \gamma\eta_c)$	23.53	PDG2012 ^[10]
$B_r(\phi \rightarrow K^+K^-)$	1.02	PDG2012 ^[10]
4-C Fit	0.10	Correcting MC to data
$M(K^+K^-)$	0.71	$\psi' \rightarrow \gamma\chi_{cJ}(\phi\phi)(J=0,1,2)$
fitting method	13.76	Miss resonance (0^+)
Total	27.62	$\sqrt{\sum \sigma_i^2}$

3.1.6 Numerical result and Summary

For $\eta_c \rightarrow \phi\phi$, the branching fraction is calculated by

$$Br(\eta_c \rightarrow \phi\phi) = \frac{N_{signal}}{N_{J/\psi} \epsilon Br(J/\psi \rightarrow \gamma\eta_c) Br^2(\phi \rightarrow K^+K^-)} = (2.09^{+0.10}_{-0.12} \pm 0.58) \times 10^{-3}, \quad (3-6)$$

where $N_{signal} = 494^{+23}_{-28}$ and $\epsilon = (25.89 \pm 0.06)\%$ are the number of event and the detection efficiency, respectively. $N_{J/\psi} = 225 \times 10^6$ is the total decays of J/ψ . $Br(J/\psi \rightarrow \gamma\eta_c) = (1.70 \pm 0.40)\%$, $Br(\phi \rightarrow K^+K^-) = (48.90 \pm 0.50)\%$ are the branching fraction of each channel cited from PDG2012^[10]. Here the first and second errors are statistical and systematic ones, respectively. The systematic error is dominated by the branching fraction $Br(J/\psi \rightarrow \phi\phi)$.

The production of branching fraction of $Br(J/\psi \rightarrow \gamma\eta_c, \eta_c \rightarrow \phi\phi)$ is calculated by:

$$Br(J/\psi \rightarrow \gamma\eta_c, \eta_c \rightarrow \phi\phi) = \frac{N_{signal}}{N_{J/\psi} \epsilon Br^2(\phi \rightarrow K^+K^-)} = (3.55^{+0.16}_{-0.20} \pm 0.51) \times 10^{-5}, \quad (3-7)$$

where the first and second errors are statistical and systematic ones, respectively.

3.2 $J/\psi \rightarrow \gamma\eta_c, \eta_c \rightarrow \omega(\pi^0\pi^+\pi^-)\phi(K^+K^-)$

3.2.1 Event selection

3.2.1.1 General selection criteria

The final states of this decay channel are three photons and four charged tracks ($K^+K^-\pi^+\pi^-$). In order to obtain high quality data sample, the same pre-selections as before will set to select good photons and charged tracks. Events with three or more photons and four charged tracks with zero net charge are retained for further study.

In order to improve the resolution and to suppress background, the 4C-kinematical fit has been imposed on the $J/\psi \rightarrow \gamma\gamma\gamma K^+K^-\pi^+\pi^-$ hypothesis by looping over all selected photon candidates. After test all the combinations, the combination of $\gamma\gamma\gamma K^+K^-\pi^+\pi^-$ with a minimum χ^2 value will be survival. The decay channel, $J/\psi \rightarrow \gamma\eta_c, \eta_c \rightarrow \omega(\pi^0\pi^+\pi^-)\phi(K^+K^-)$ has been put into inclusive MC sample according to the value from PDG2012. Figures 3.21 show the comparison between inclusive MC sample and exclusive MC sample. The left one is the comparison between inclusive MC sample and exclusive MC sample, while the right one is the optimization with $\frac{N_{signal}}{\sqrt{N_{signal}+N_{background}}}$, the backgrounds are estimated from inclusive MC sample.

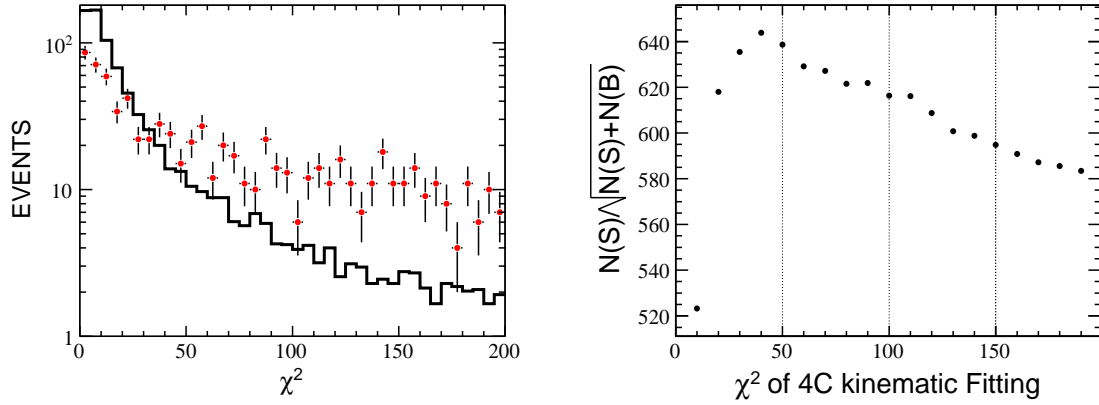


Figure 3.19 The comparison between inclusive MC sample and exclusive MC sample. The red dots are inclusive MC sample, while the black histogram is exclusive MC sample. Left: the distribution of χ^2 Right: the optimization of χ^2 .

3.2.1.2 Final Selection and the main background

Figure 3.20 shows the scatter plot of the invariant mass $M_{\pi^0\pi^+\pi^-}$ versus $M_{K^+K^-}$ after all the general selection criteria applied. There are clear bands corresponding to η , ω and ϕ . In order to suppress the background and obtain higher purity of signal sample, inclusive MC sample has been used to optimize the mass window of ω and ϕ . Figure 3.21 shows the optimization of mass window of $\gamma\gamma$, K^+K^- and $\pi^0\pi^+\pi^-$.

Final event selection criteria are:

- χ^2 of the 4C-kinematic fitting
 $\chi^2 < 40$;
- Mass window of $\pi^0\pi^+\pi^-$
 $|M_{\pi^+\pi^-\pi^0} - 0.783| < 0.030 \text{ GeV}/c^2$;
- Mass window of K^+K^-
 $|M_{K^+K^-} - 1.020| < 0.008 \text{ GeV}/c^2$.

The analysis with inclusive MC sample shows that the main background is from $J/\psi \rightarrow \eta'(\gamma\omega)\phi(K^+K^-)$. Table 3.4 is the summary of the main backgrounds.

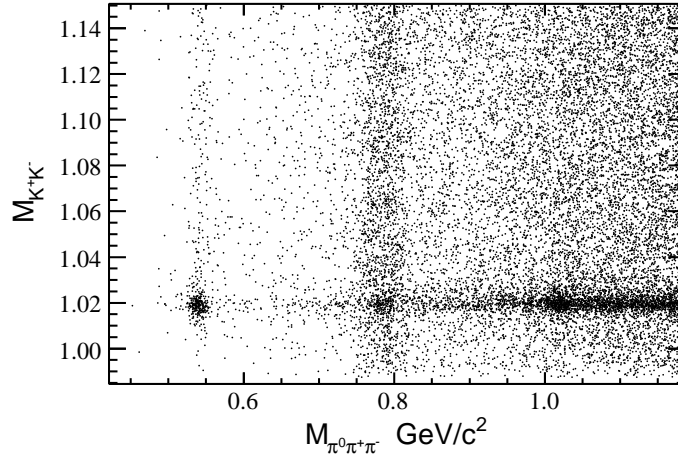


Figure 3.20 the scatter plot between $M_{\pi^0\pi^+\pi^-}$ and $M_{K^+K^-}$. horizontal coordinate: the mass of $\pi^0\pi^+\pi^-$. longitudinal coordinate: the mass of K^+K^- .

Table 3.4 Summary of the main decay channel within the mass range interested

The main decay chain	N_{event}
$J/\psi \rightarrow \eta'(\gamma\omega)\phi(K^+K^-)$	61
$J/\psi \rightarrow f_0(980)\omega(\pi^0\pi^+\pi^-), f_0(980) \rightarrow K^+K^-$	4
$J/\psi \rightarrow f_1(1420)\omega(\pi^0\pi^+\pi^-), f_1(1420) \rightarrow \pi^0 K^+K^-$	3
$J/\psi \rightarrow f_1(1285)\omega(\pi^0\pi^+\pi^-), f_1(1285) \rightarrow \pi^0 K^+K^-$	2
$J/\psi \rightarrow \pi^0\pi^+\pi^- K^+K^-$ (including other resonance)	5

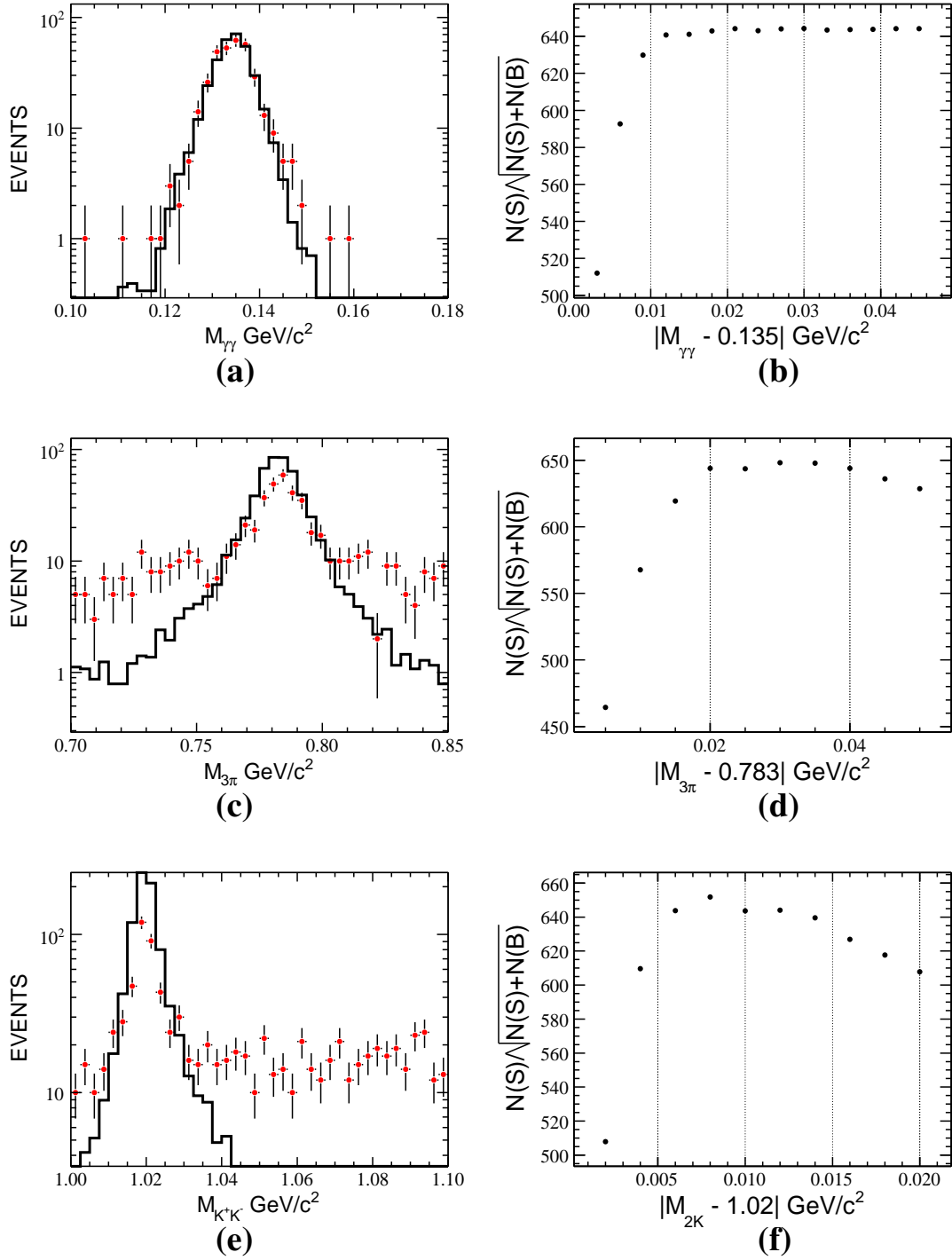


Figure 3.21 The comparison between inclusive MC sample and exclusive MC sample, the red error bars are inclusive MC sample, the black histograms are exclusive MC sample.

3.2.2 The uplimit calculation of the decay channel

The number of events of $J/\psi \rightarrow \gamma\eta_c \rightarrow \gamma\omega\phi$ is obtained by fitting to the mass distribution of $M_{\omega\phi}$, where the signal shape is obtained from MC simulation, and the background is described by a 2nd-order Chebychev function, whose parameters are floated. Figure 3.22 shows the fit result of the mass distribution of $M_{\omega\phi}$. Bayesian method is used to estimate the upper limit of number of the signal event because of no signal observed. Figure 3.23 shows the estimation of upper limit of $J/\psi \rightarrow \gamma\eta_c(\omega\phi)$, $\omega \rightarrow \pi^0\pi^+\pi^-$, $\phi \rightarrow K^+K^-$, at a 90% confidence level, the upper limit of the number of the signal is 24. The detection efficiency is $(6.03 \pm 0.06)\%$.

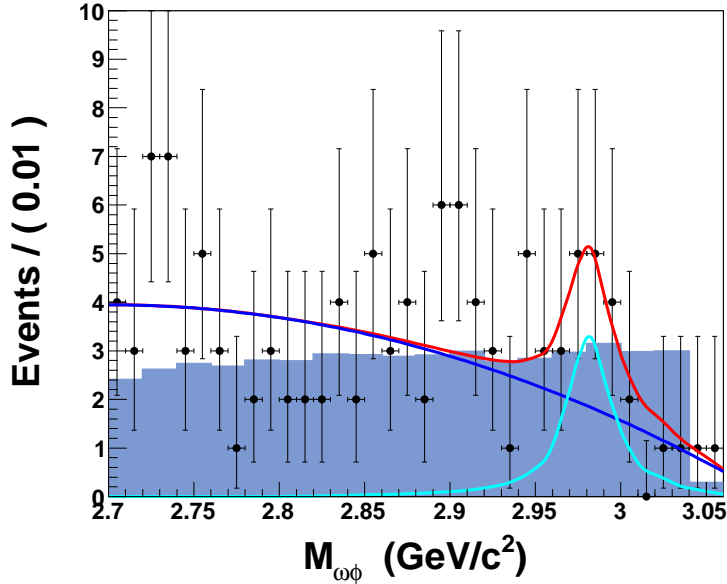


Figure 3.22 The fitting result of $M_{\omega\phi}$. The black dots are the distribution of data sample, the red line is the fitting result, the light blue line is the fitting result of background, the hatched histogram is estimated background($J/\psi \rightarrow \eta'\omega$)

3.2.3 Source of systematic error

The sources of systematic errors are including the several items:

- Total number of J/ψ ,
- Photon reconstruction,
- Tracking Efficiency,
- 4C Kinematic Fitting,
- Branching fraction of $J/\psi \rightarrow \gamma\eta_c$,

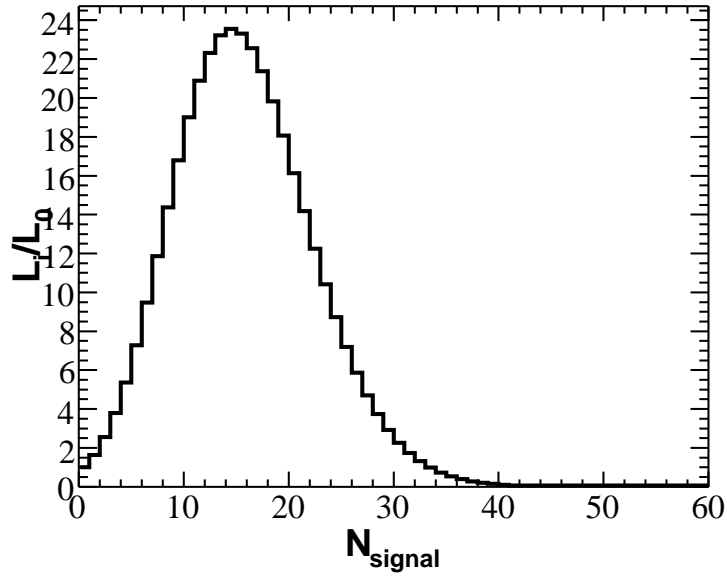


Figure 3.23 Estimation of the number of signal events with maximum likelihood method. horizontal coordinate: the event number of the signal. longitudinal coordinate: the likelihood value.

- Branching fraction $\phi \rightarrow K^+K^-$,
- Branching fraction $\pi^0 \rightarrow \gamma\gamma$,
- Branching fraction $\omega \rightarrow \pi^0\pi^+\pi^-$,
- Mass(K^+K^-),
- Mass($\pi^0\pi^+\pi^-$),
- Number of photon,
- Fitting Function for Background.

3.2.3.1 Total number of J/ψ

The error of the total number of J/ψ is 1.24%^[86].

3.2.3.2 photon reconstruction

One of the systematic errors is due to the difference of photon efficiency between MC and data. Here we cite 1%^[91] as the uncertainty.

3.2.3.3 Tracking efficiency and Particle Identification(PID)

The uncertainty associated with the tracking is taken to be 1%^[92]. Only K^+ and K^- are identified in the analysis, and the systematic error of identification is assigned as 2% for each kaon, then 4% is taken as the systematic error.

3.2.3.4 4C Kinematic Fitting

The method to estimate the uncertainty of 4C-kinematic fitting is same as the analysis of $J/\psi \rightarrow \gamma\eta_c(\phi\phi)$. The parameters of pion are obtained by the control sample, $J/\psi \rightarrow \omega(\pi^0\pi^+\pi^-)\eta(\pi^0\pi^+\pi^-)$. The detailed information on how to obtain the parameters from this control sample is described in Appendix A.1.2. Table A.2 shows the correction factors.

In this section, two control samples will be selected to estimate the uncertainty of 4C-kinematic fitting, one is $J/\psi \rightarrow \omega(\pi^0\pi^+\pi^-)K^+K^-$ with the final state $\pi^0\pi^+\pi^-K^+K^-$, the other one is $J/\psi \rightarrow \omega(\pi^0\pi^+\pi^-)\pi^0K^+K^-$ with the final state $\pi^0\pi^+\pi^-\pi^0K^+K^-$. After the general selection criteria applied to charged tracks and photons, PID information is used to identify kaon and pion, and there are two pions and two kaons must be identified for each control samples. A 4C kinematic fit is applied to each of these two control samples to select the photons with a minimum χ^2 . The number of good photon must be larger than 2 and larger than 4 for $J/\psi \rightarrow \omega(\pi^0\pi^+\pi^-)K^+K^-$ and $J/\psi \rightarrow \omega(\pi^0\pi^+\pi^-)\pi^0K^+K^-$, respectively. Figures 3.24 and figures 3.25 show the comparison between MC and the two control samples.

The final selection criteria are same for these two decays. Two π^0 s in the $J/\psi \rightarrow \pi^0\pi^+\pi^-\pi^0K^+K^-$ are reconstruct by minimizing the combination with the value $\sqrt{(M_{\gamma\gamma}^1 - 0.135)^2 + (M_{\gamma\gamma}^2 - 0.135)^2}$. After all selection criteria applied, the purity of $J/\psi \rightarrow \pi^0\pi^+\pi^-K^+K^-$ sample is nearly to 99.59% and that of $J/\psi \rightarrow \pi^0\pi^+\pi^-\pi^0K^+K^-$ is nearly to 99.00% obtained from inclusive MC sample.

- χ^2 of the 4C-kinematic fitting

$$\chi^2 < 110;$$

- Mass window of $\gamma\gamma$

$$|M_{\gamma\gamma} - 0.135| < 0.015 \text{ GeV}/c^2$$

- Identification of kaon and pion

Two pions and two kaons are required with particle identification based on the TOF and dE/dx information. The probability of pion candidate must be larger than that of any other particles hypothesis; similarly, the probability of kaon must be larger than that of any kinds of other particle hypothesis.

- Mass window of $\pi^0\pi^+\pi^-$ $|M_{\pi^0\pi^+\pi^-} - 0.783| < 0.050 \text{ GeV}/c^2$.

With the parameters obtained from $J/\psi \rightarrow \omega(\pi^0\pi^+\pi^-)\eta(\pi^0\pi^+\pi^-)$ and $J/\psi \rightarrow \phi(K^+K^-)K^+K^-$, the MC samples of $J/\psi \rightarrow \omega K^+K^-$ and $J/\psi \rightarrow \omega\pi^0 K^+K^-$ will be corrected to match data samples. Figures 3.26 and figures 3.27 are the comparison of χ^2 for

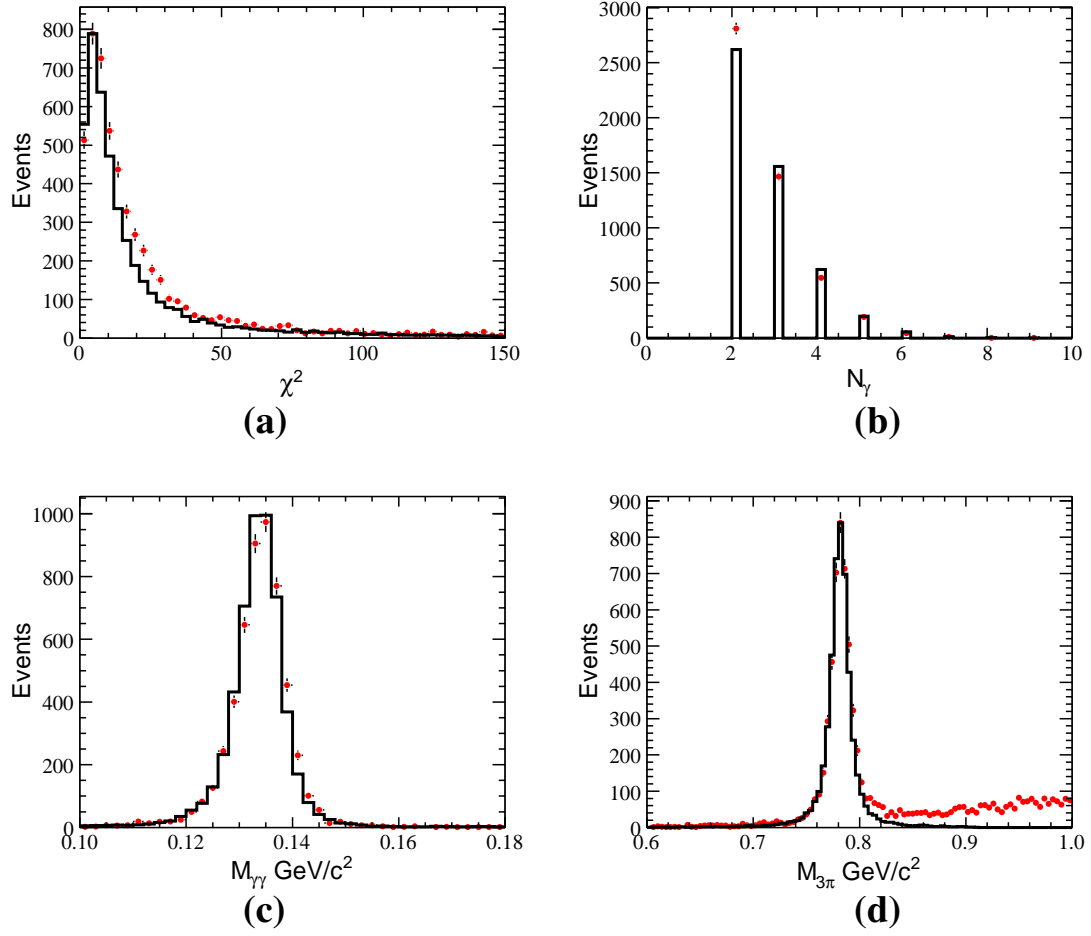


Figure 3.24 The comparison of $J/\psi \rightarrow \omega(\pi^0\pi^+\pi^-)K^+K^-$ between MC and data, the red error bars are data, the black histograms are MC.

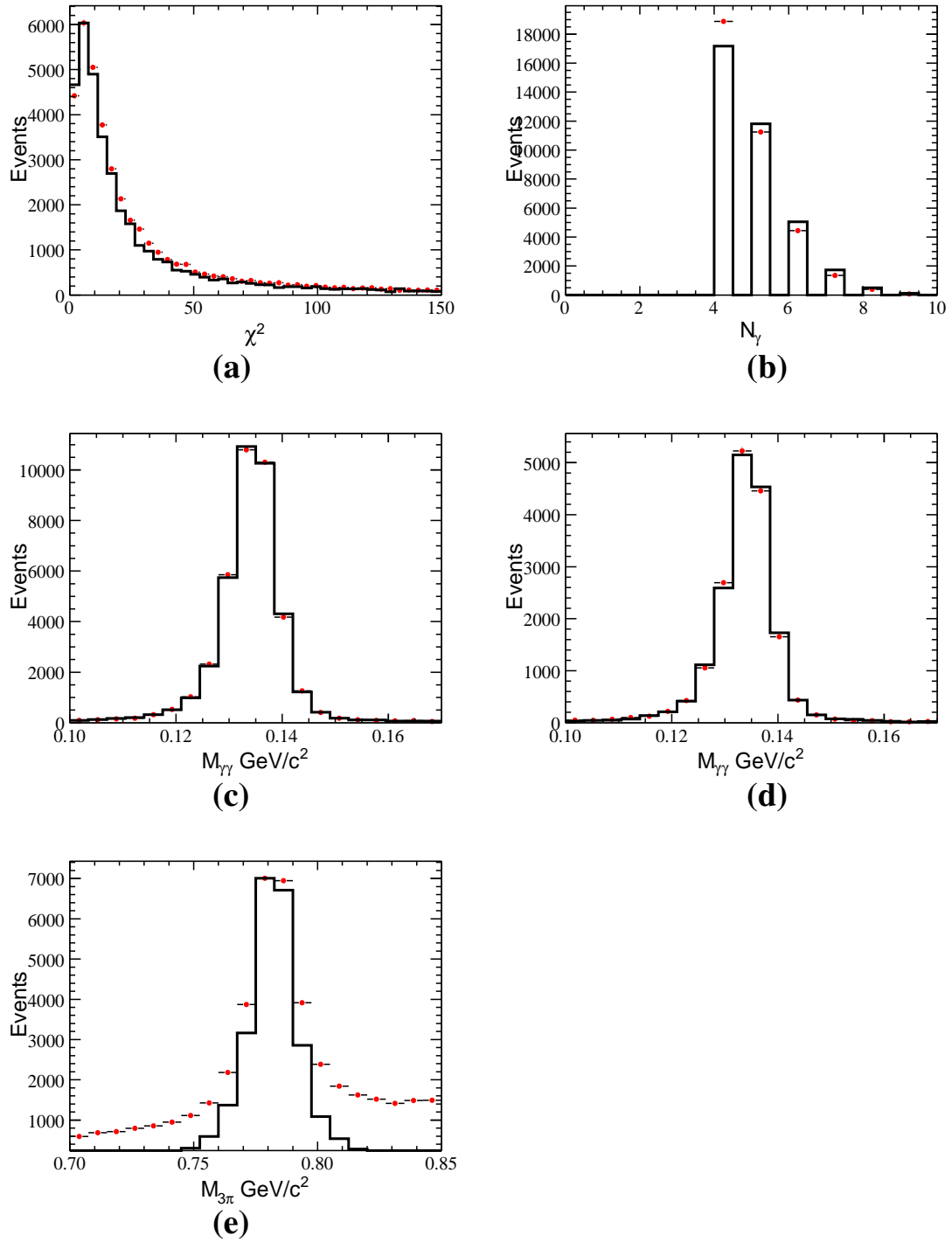


Figure 3.25 The comparison of $J/\psi \rightarrow \omega(\pi^0\pi^+\pi^-)\pi^0 K^+ K^-$ between MC and data, the red error bars are data, the black histograms are MC.

these two samples. The uncertainty are 0.44% and 0.68% for $J/\psi \rightarrow \omega(\pi^0\pi^+\pi^-)K^+K^-$ and $J/\psi \rightarrow \omega(\pi^0\pi^+\pi^-)\pi^0K^+K^-$, respectively. And the larger one, 0.68%, will be selected as the uncertainty of this analysis.

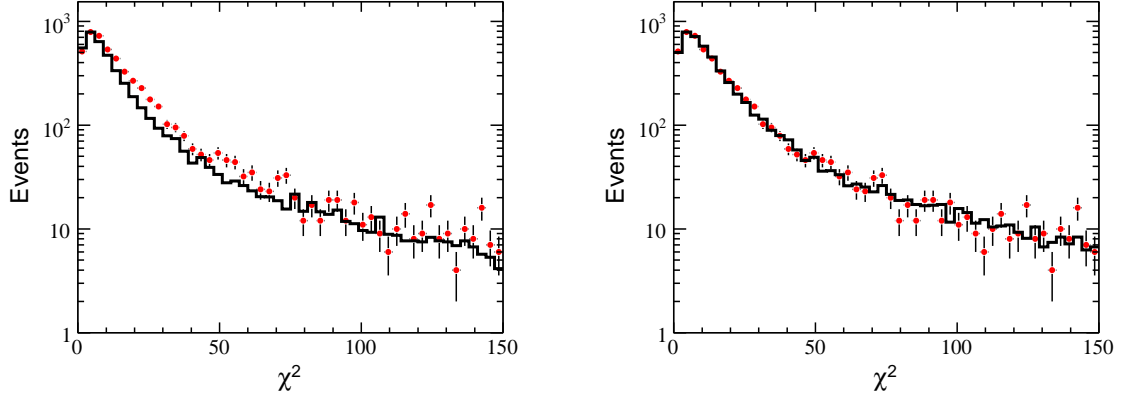


Figure 3.26 The comparison of χ^2 between data and MC for $J/\psi \rightarrow \omega(\pi^0\pi^+\pi^-)K^+K^-$. The red dots are data sample, while the black histogram is MC sample. Left: before correction Right: After correction.

3.2.3.5 Branching fraction of $J/\psi \rightarrow \gamma\eta_c$

According to the PDG2012, the uncertainty of $J/\psi \rightarrow \gamma\eta_c$ is 23.53%^[10].

3.2.3.6 Branching fraction of $\phi \rightarrow K^+K^-$

According to the PDG2012, the uncertainty of $\phi \rightarrow K^+K^-$ is 1.02%^[10].

3.2.3.7 Branching fraction of $\pi^0 \rightarrow \gamma\gamma$

According to the PDG2012, the uncertainty of $\pi^0 \rightarrow \gamma\gamma$ is 0.03%^[10].

3.2.3.8 Branching fraction of $\omega \rightarrow \pi^0\pi^+\pi^-$

According to the PDG2012, the uncertainty of $\omega \rightarrow \pi^0\pi^+\pi^-$ is 0.78%^[10].

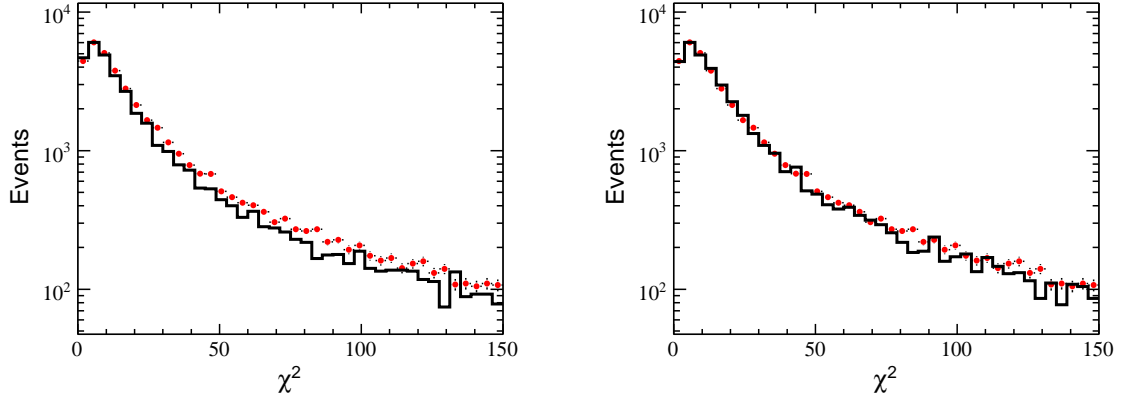


Figure 3.27 The comparison of χ^2 between data and MC for $J/\psi \rightarrow \omega(\pi^0\pi^+\pi^-)\pi^0 K^+K^-$. The red dots are data sample, while the black histogram is MC sample. Left: before correction Right: After correction.

3.2.3.9 Mass window of K^+K^-

The control sample, $\psi(2S) \rightarrow \gamma\chi_{cJ}, \chi_{cJ} \rightarrow \phi\phi$ ($J=0,1,2$), is used to estimate the uncertainty of the mass window of K^+K^- , all the selections are the same as before, except for the mass window cut. The uncertainty of K^+K^- is 1.13%. Figure 3.28 shows the comparison of the mass distribution of K^+K^- between data and MC sample.

3.2.3.10 Mass window of $\pi^0\pi^+\pi^-$

The uncertainty due to this requirement is estimated with the control sample $J/\psi \rightarrow \omega(\pi^0\pi^+\pi^-)\eta(\pi^0\pi^+\pi^-)$. All the selection criteria are the same as mentioned before. Two π^0 candidates are selected with the requirement of $|M_{\gamma\gamma} - M_{\pi^0}| < 0.015 \text{ GeV}/c^2$, then the η reconstructed by $\pi^0\pi^+\pi^-$ is restrained within the mass window from $0.52 \text{ GeV}/c^2$ to $0.57 \text{ GeV}/c^2$. The ω resonance is shown in figure 3.29 (left). The difference in the ω cut efficiency between the MC and the data is taken as the uncertainty due to this cut, which is determined to be 1.45%.

3.2.3.11 Background shape

The uncertainty due to the background shape is estimated with another fit method, and the difference in the signal yield is taken as the systematic error. The signal is described

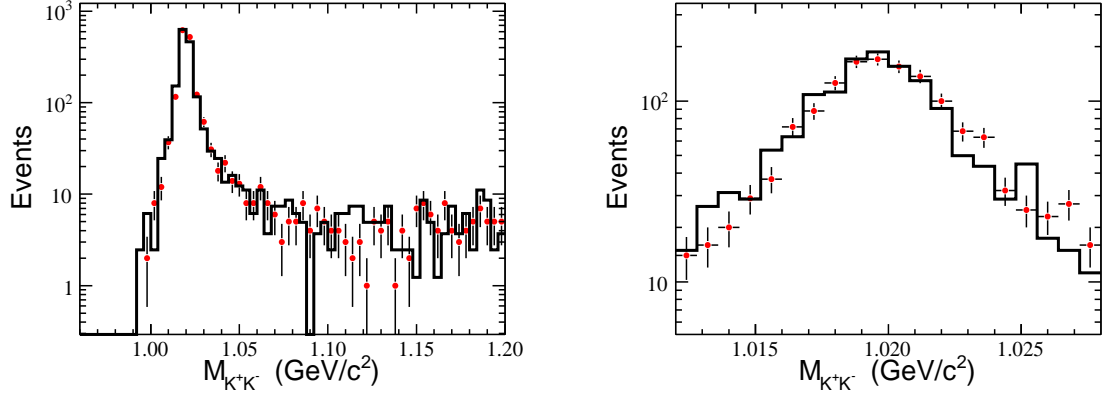


Figure 3.28 The comparison of $M_{K^+K^-}$ between data and MC. The red dots are data sample, while the black histogram is MC sample. Left: before put the mass window cut Right: After put the mass window cut.

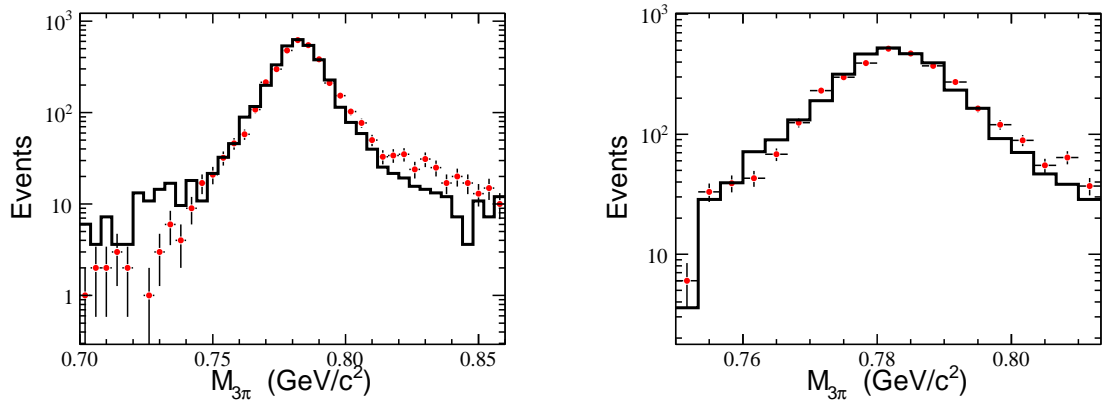


Figure 3.29 The comparison between data and MC. Left: before applied the selection on $M_{\pi^0\pi^+\pi^-}$ Right: after applied the selection on $M_{\pi^0\pi^+\pi^-}$.

with MC shape, and the background is described with a 3rd-order Chebychev function, whose parameters are floated. The sample procedure as before is applied to obtain the upper limit in the data analysis. The upper limit is determined to be 22 at a 90% C.L. Figure 3.30 shows the result. According to this number, 8.33% is taken as the uncertainty from the background shape.

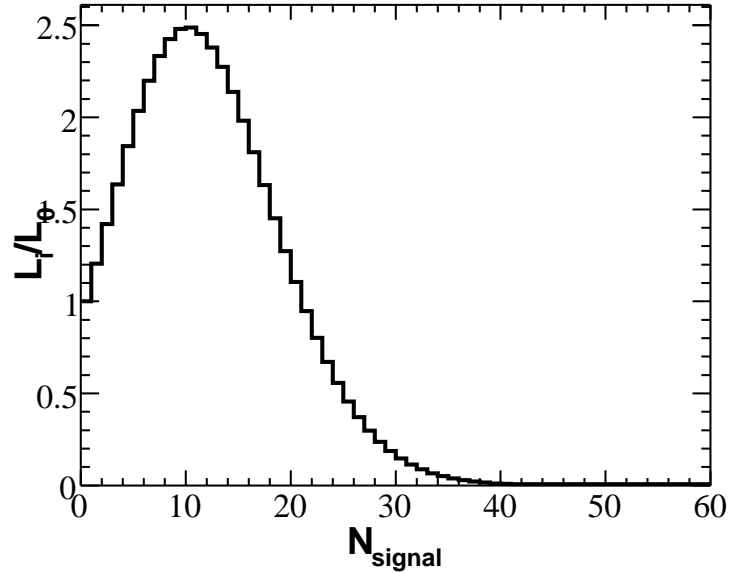


Figure 3.30 Estimation of the number of signal event with maximum likelihood for systematic. horizontal coordinate: the event number of the signal. longitudinal coordinate: the likelihood value

3.2.3.12 summary of the systematic errors

Table 3.5 summarizes the systematic errors in the analysis.

3.2.4 Numerical result

The upper limit of the branching fraction is calculated with

$$Br(\eta_c \rightarrow \omega\phi) < \frac{N_{uplimit}}{N_{J/\psi}\epsilon Br(J/\psi)Br(\phi)Br(\omega)Br(\pi^0)(1.00 - \sigma_{sys.})} = 3.26 \times 10^{-4}, \quad (3-8)$$

where $N_{uplimit} = 24$ and $\epsilon = (6.03 \pm 0.06)\%$ are the upper limit of signal yields and the detection efficiency, respectively. $\sigma_{sys.} = 25.90\%$ is the systematic error. $N_{J/\psi} = 225 \times 10^6$ is the total number of J/ψ . $Br(J/\psi) = Br(J/\psi \rightarrow \gamma\eta_c) = (1.70 \pm 0.40)\%$, $Br(\phi) = Br(\phi \rightarrow K^+K^-) = (48.90 \pm 0.50)\%$, $Br(\omega) = Br(\omega \rightarrow \pi^0\pi^+\pi^-) = (89.20 \pm 0.70)\%$ and

Table 3.5 Summary of systematic errors(%)

Source	Error(%)	Comment
$N_{J/\psi}$	1.24	Chin.Phys.C 36 , 915-925(2012)
Tracking	1.00×4	Chen Y. et al., DAQ meeting
Photon	1.00×3	Phys. Rev. D 83 , 112005(2011)
PID	2.00×2	Only identify K^+K^-
$B_r(J/\psi \rightarrow \gamma\eta_c)$	23.53	PDG2012 ^[10]
$B_r(\phi \rightarrow K^+K^-)$	1.02	PDG2012 ^[10]
$B_r(\pi^0 \rightarrow \gamma\gamma)$	0.03	PDG2012 ^[10]
$B_r(\omega \rightarrow \pi^0\pi^+\pi^-)$	0.78	PDG2012 ^[10]
4-C Fit	0.68	Correct MC to data
$M(K^+K^-)$	1.13	$\psi(2S) \rightarrow \gamma\chi_{cJ}(\phi\phi)$
$M(\pi^0\pi^+\pi^-)$	1.45	$J/\psi \rightarrow \omega(\pi^0\pi^+\pi^-)\eta(\pi^0\pi^+\pi^-)$
N_γ	–	Ignored
backgrounds shape	8.33	change to higher order Chebychev function
Total	25.90	$\sqrt{\sum_i \sigma_i^2}$

$Br(\pi^0) = Br(\pi^0 \rightarrow \gamma\gamma) = (98.82 \pm 0.03)\%$ are the branching fractions of each channel cited from PDG2012^[10].

3.2.5 Cross check

A new MC sample has been re-generated according to the result obtained from the last section. We use the new MC sample to optimize the selection. Figure 3.31 shows the optimization result. According to these optimization, new selections are applied to data sample. The final detection efficiency is $(5.26 \pm 0.06)\%$.

Final event selection criteria are:

- χ^2 of the 4C-kinematic fitting
 $\chi^2 < 40$
- Mass window of $\pi^0\pi^+\pi^-$
 $|M_{\pi^+\pi^-\pi^0} - 0.783| < 0.020 \text{ GeV}/c^2$
- Mass window of K^+K^-
 $|M_{K^+K^-} - 1.020| < 0.006 \text{ GeV}/c^2$

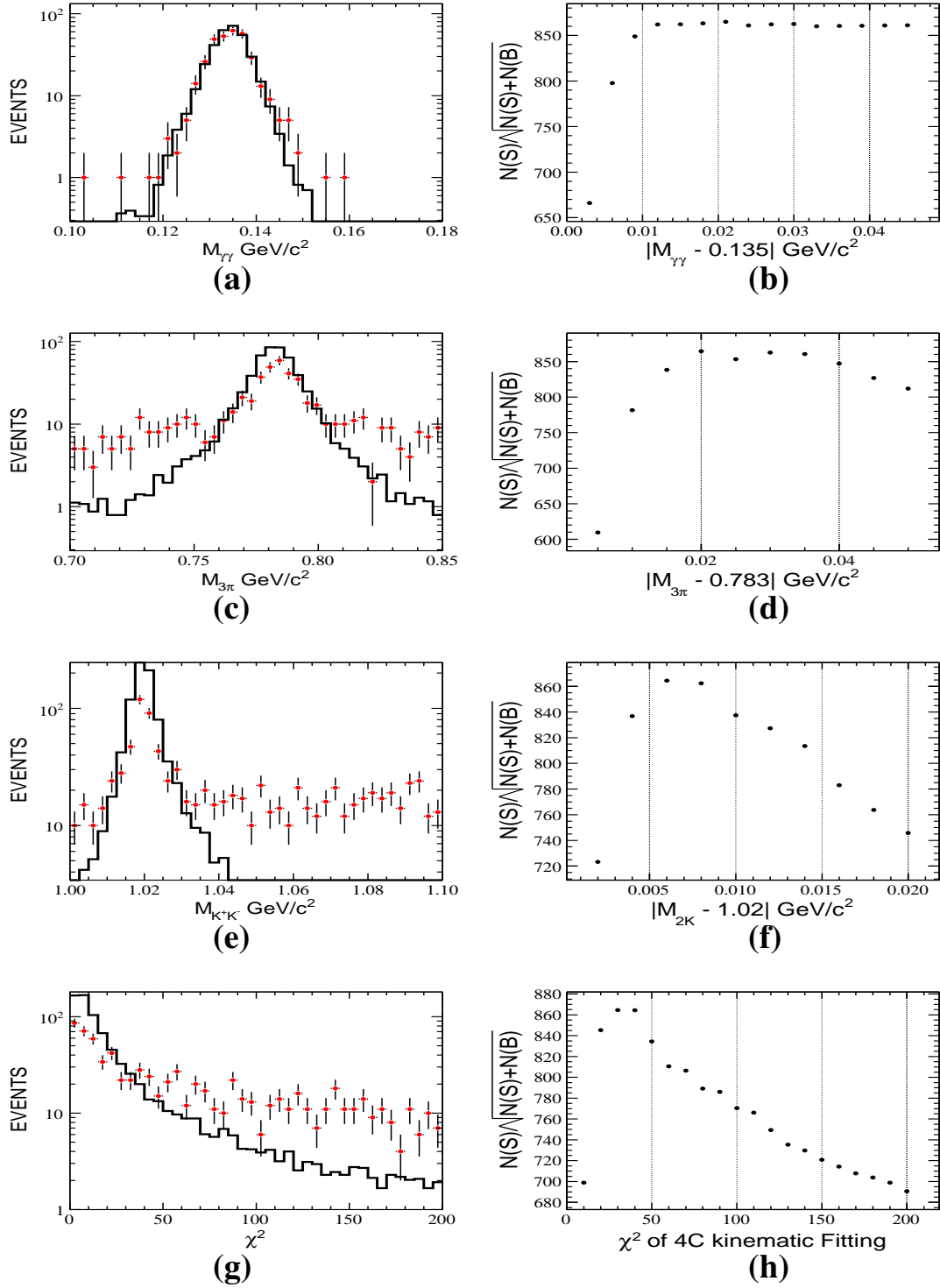


Figure 3.31 The comparison between inclusive MC sample and exclusive MC sample, the red error bars are inclusive MC sample, the black histograms are exclusive MC sample.

3.2.5.1 Numerical result

The same method is applied to estimate the event number of this decay channel. Figure 3.32 shows the fitting result. The upper limit of the number of the signal is 20 at 90% confidence level.

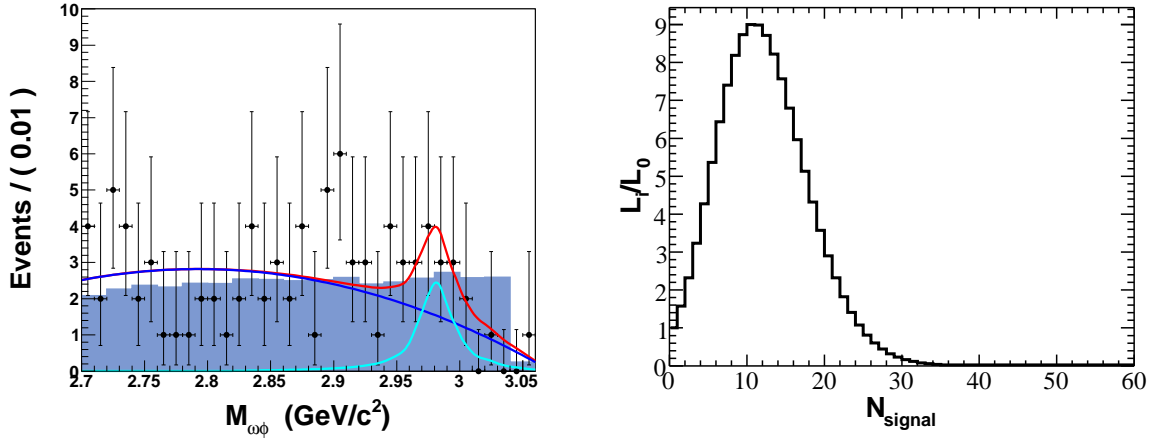


Figure 3.32 The fitting result of $M_{\omega\phi}$. Left: Mass spectrum fitting result. The black dots are the distribution of data sample, the red line is the fitting result, the light blue line is the fitting result of background, the hatched histogram is estimated background($J/\psi \rightarrow \eta'\omega$) Right: Estimation of upper limit.

The systematic errors is shown in table 3.6.

The upper limit of the branching fraction is calculated with

$$Br(\eta_c \rightarrow \omega\phi) < \frac{N_{uplimit}}{N_{J/\psi}\epsilon Br(J/\psi)Br(\phi)Br(\omega)Br(\pi^0)(1.00 - \sigma_{sys.})} = 3.14 \times 10^{-4}, \quad (3-9)$$

where $N_{uplimit} = 20$ and $\epsilon = (5.26 \pm 0.06)\%$ are the upper limit of signal yields and the detection efficiency, respectively. $\sigma_{sys.} = 26.51\%$ is the systematic error.

Table 3.6 Summary of systematic errors(%)

Source	Error(%)	Comment
$N_{J/\psi}$	1.24	Chin.Phys.C 36 , 915-925(2012)
Tracking	1.00×4	Chen Y. et al., DAQ meeting
Photon	1.00×3	Phys. Rev. D 83 , 112005(2011)
PID	2.00×2	Only identify K^+K^-
$B_r(J/\psi \rightarrow \gamma\eta_c)$	23.53	PDG2012 ^[10]
$B_r(\phi \rightarrow K^+K^-)$	1.02	PDG2012 ^[10]
$B_r(\pi^0 \rightarrow \gamma\gamma)$	0.03	PDG2012 ^[10]
$B_r(\omega \rightarrow \pi^0\pi^+\pi^-)$	0.78	PDG2012 ^[10]
4-C Fit	0.68	Correct MC to data
M(K^+K^-)	0.51	$\psi(2S) \rightarrow \gamma\chi_{cJ}(\phi\phi)$
M($\pi^0\pi^+\pi^-$)	2.06	$J/\psi \rightarrow \omega(\pi^0\pi^+\pi^-)\eta(\pi^0\pi^+\pi^-)$
N_γ	–	Ignored
backgrounds shape	10.00	Change to higher order Chebychev function
Total	26.51	$\sqrt{\sum_i \sigma_i^2}$

Chapter 4 Precision measurement on the branching fractions of $\psi(2S)$ hadronic transitions to J/ψ

This section will present measurements on the branching ratios of $\psi(2S) \rightarrow \pi^0(\eta)J/\psi$ using the $\psi(2S)$ data sample accumulated at BESIII from March 7th to April 4th 2009, the total number of events is 106 M and the integrated luminosity is $162.80 \pm 0.01 \text{ pb}^{-1}$. In addition, 42.6 pb^{-1} data collected at the energy 3.65 GeV from May 26th to June 3rd 2009 is used to estimate the background from the QED processes. The BESIII Offline Software System (BOSS) version used to reconstruct data is BOSS 6.5.5. A 106 M inclusive $\psi(2S)$ MC sample is used to study the background. It is generated with KKMC plus BesEvtGen, and the known branching ratios are taken from PDG value^[87], while the unknown remainder ratios are generated according to the Lundcharm model^[85].

4.1 $\psi(2S) \rightarrow \pi^0(\gamma\gamma)J/\psi(l^+l^-)$

4.1.1 Event selection and background study

4.1.1.1 General selection criteria

The final states include two photons and two leptons ($\mu^+\mu^-$ or e^+e^-). The pre-selected procedures for photons and charged tracks are the same as the last chapter. After tracks and photons are selected, it is required that the number of good photons must be larger than two. Figure 4.1 shows a comparison of the number of good photons between MC and data. The distributions of MC and data are in good agreement with each other. For the charged tracks, the number of good tracks reconstructed in MDC must be equal to two with zero net charge.

In order to improve the resolution and to suppress background, the 4C-kinematical fit has been imposed on the $\psi(2S) \rightarrow \gamma\gamma l^+l^-$ hypothesis by looping over all selected photon candidates, where $l = e$ or μ . After test all the combinations, the combination of $\gamma\gamma l^+l^-$ with a minimum χ^2 value will be survival. Figures 4.2 and 4.3 show the χ^2 distributions for $\psi(2S) \rightarrow \gamma\gamma e^+e^-$ and $\psi(2S) \rightarrow \gamma\gamma\mu^+\mu^-$, respectively. The left figure is the χ^2 distribution for each mode, and the right one is the optimization of the χ^2 with $\frac{N_{signal}}{\sqrt{N_{signal}+N_{background}}}$. The χ^2 distribution of data is consistent with that of the MC.

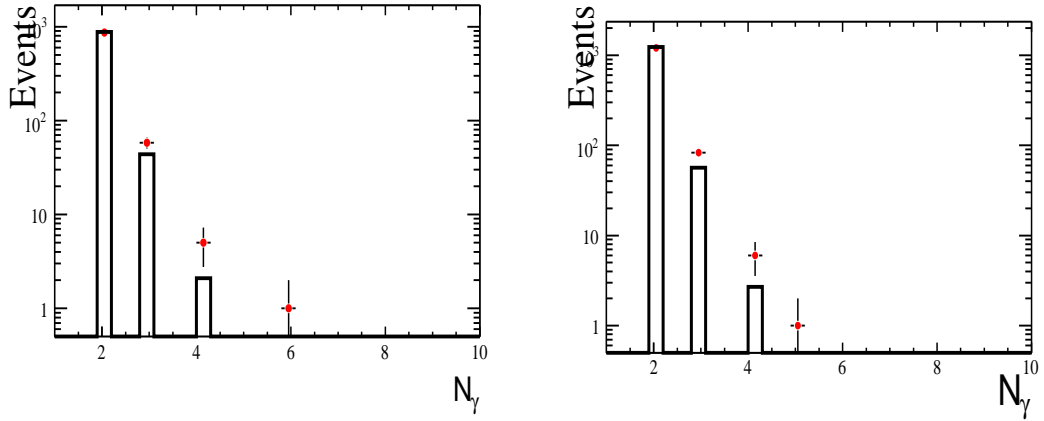


Figure 4.1 The number of good photon distribution for $\psi(2S) \rightarrow \pi^0 J/\psi$. Left: $J/\psi \rightarrow e^+e^-$. Right: $J/\psi \rightarrow \mu^+\mu^-$

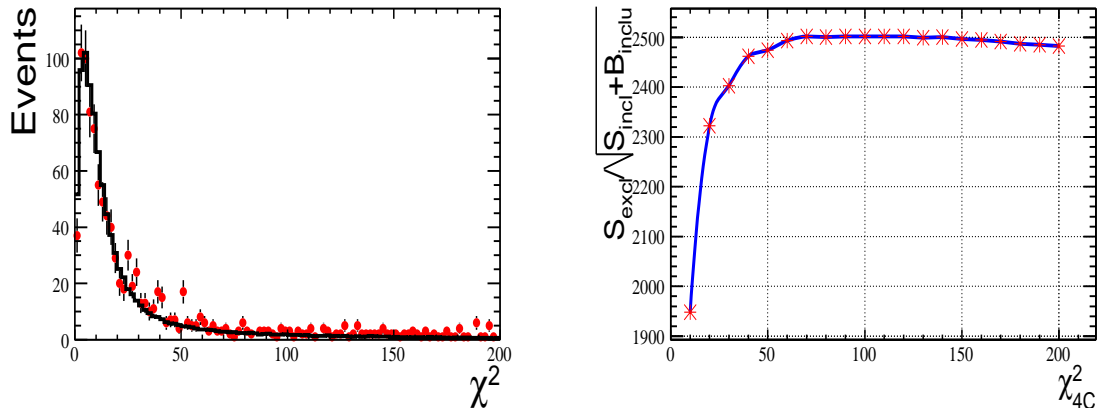


Figure 4.2 The χ^2 distribution for $\psi(2S) \rightarrow \pi^0 J/\psi$. Left: The χ^2 distribution of $J/\psi \rightarrow e^+e^-$. Right: The optimization of χ^2 .

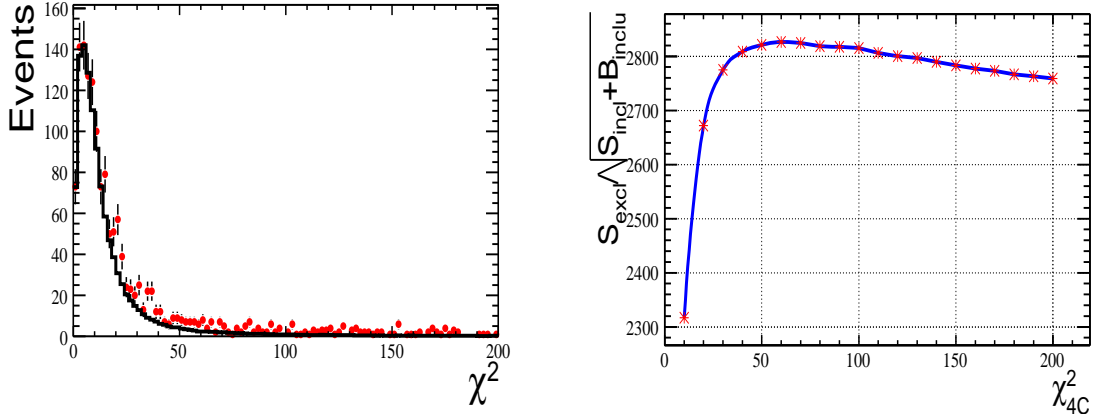


Figure 4.3 The χ^2 distribution for $\psi(2S) \rightarrow \pi^0 J/\psi$. Left: The χ^2 distribution of $J/\psi \rightarrow \mu^+ \mu^-$. Right: The optimization of χ^2 .

4.1.1.2 Final Selection and background study

The lepton can be selected according to the ratio of deposited energy measured in the EMC to the momentum measured in the MDC (E/p). Figure 4.4 shows the comparison of the E/p ratio between MC and data sample. There the red dots are the distribution of data, while the black histogram is that of exclusive MC sample. One can see that they are in a good agreement with each other. If the E/p ratio of the charged particles is larger than 0.8, tracks are selected as electrons, and the tracks are identified as muons if their E/p ratio is larger than 0.08 and less than 0.22. Figure 4.5 shows the distribution of the invariant mass of two leptons (electron or muon). In order to constrain the two leptons to the J/ψ signal range, it is required that the invariant mass of these two leptons is larger than $3.05 \text{ GeV}/c^2$ and less than $3.15 \text{ GeV}/c^2$.

To obtain the high purity of the signal, the χ^2 of kinematical fitting is required less than 100 and 60 for $\gamma\gamma e^+ e^-$ and $\gamma\gamma\mu^+ \mu^-$, respectively, according to the χ^2 optimization as shown in figure 4.2 and 4.3. The photon coming from π^0/η with higher energy is tagged as γ_1 while the other one with lower energy tagged as γ_2 . The potential background channels are studied with an inclusive MC sample. After applying the same selection criteria to data, we find that the dominant backgrounds come from $\psi(2S) \rightarrow \gamma\chi_{cJ}, \chi_{cJ} \rightarrow \gamma J/\psi$ as shown in figure 4.6. From the scatter plot of $M_{\gamma_1\gamma_2}$ versus $M_{\gamma_1 J/\psi(e^+e^-)}$, one can clearly see that there are several bands corresponding to the $\chi_{c1,2}, \pi^0$ and η resonances. Due to the η

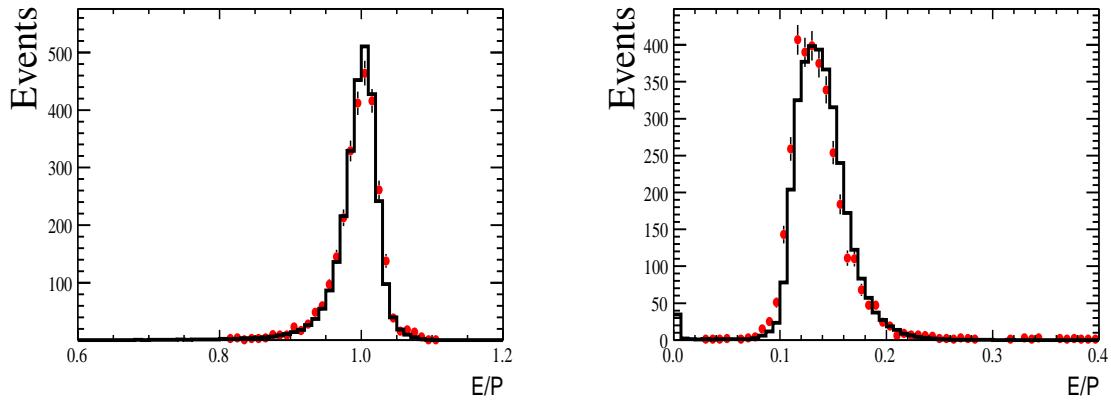


Figure 4.4 The distribution of E/p for data vs MC, the black histogram is the result of MC sample, while points with red error bars denote data sample. Left: For $\psi(2S) \rightarrow \pi^0(\gamma\gamma)J/\psi(e^+e^-)$. Right: For $\psi(2S) \rightarrow \pi^0(\gamma\gamma)J/\psi(\mu^+\mu^-)$;

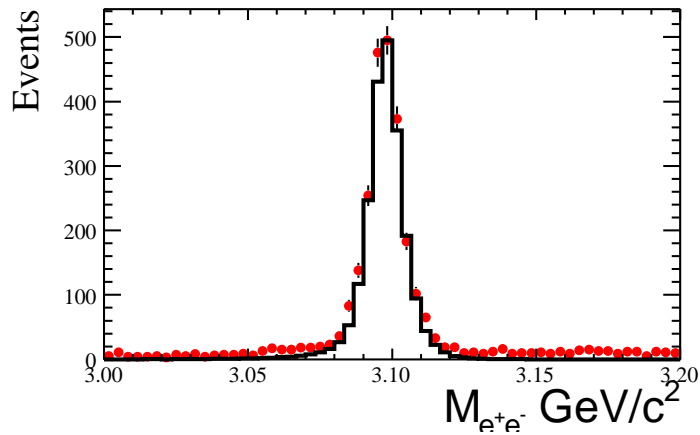


Figure 4.5 The invariant-mass distribution of leptons for data vs MC for $\psi(2S) \rightarrow \pi^0(\gamma\gamma)J/\psi(l^+l^-)$. The red error bars are data results, the black histograms are the MC results.

situated far away from the π^0 , the contamination of η to π^0 mode is negligible. In order to suppress this type of background from χ_{cJ} decays, it is required that the mass of $M_{\gamma_1 J/\psi}$ must be less than $3.50 \text{ GeV}/c^2$ or larger than $3.57 \text{ GeV}/c^2$. Except for this background, the inclusive MC sample shows that the decay $\psi(2S) \rightarrow \gamma\gamma J/\psi(l^+l^-)$ can contribute a few background events to our signal range, but the contamination level is much lower than the one from χ_{cJ} modes. In addition, the non-resonant background $\psi(2S) \rightarrow \gamma\gamma e^+e^-$ are estimated by the sideband of J/ψ with the real data. Figure 4.7 shows the two photon invariant mass distribution $m_{\gamma\gamma}$ for data and background as mentioned above. One can see that the $m_{\gamma\gamma}$ distribution of this background is flat.

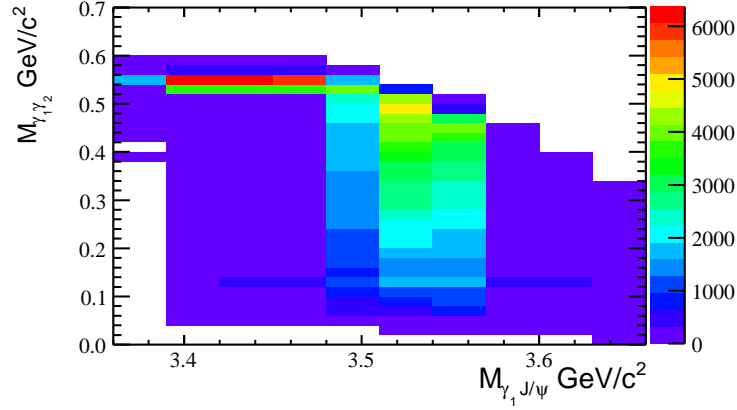


Figure 4.6 The scatter plot of $M_{\gamma_1 \gamma_2}$ vs $M_{\gamma_1 J/\psi(l^+l^-)}$ for data. The x -axis is the invariant mass of high energy photon and leptons (constrained to the J/ψ mass window), the y -axis is the two photons invariant mass.

According to the above analysis, the final selection criteria are set as follows:

- $2 \leq N_\gamma \leq 4$;
- $E/p > 0.8$ (for electron);
- $E/p > 0.08$ and $E/p < 0.22$ (for muon);
- $\chi_{4c}^2 < 100$ for $\gamma\gamma e^+e^-$, $\chi_{4c}^2 < 60$ for $\gamma\gamma\mu^+\mu^-$;
- $3.05 \text{ GeV} < M_{l^+l^-} < 3.15 \text{ GeV}$;
- $M_{\gamma_1, l^+l^-} < 3.50 \text{ GeV}$ or $3.57 \text{ GeV} < M_{\gamma_h, l^+l^-}$.

Background sources are estimated with exclusive MC samples as listed in table 4.1 and table 4.2, where N_{gen} is total number of exclusive MC sample, N_{sca} is the expected number of events in 106 M $\psi(2S)$ real data sample, which is determined by a normalization of background events observed with a ratio of the expected number in the total $\psi(2S)$

decays to that of generated events, and ε is the detection efficiency. Figure 4.7 shows the distribution of the mass of the two photons, where the red error points indicate the distribution of data, while the color histograms correspond to background sources estimated with the exclusive MC samples, continuum data sample and the sideband of J/ψ .

 Table 4.1 Summary of the background decays for $\psi(2S) \rightarrow \pi^0(\gamma\gamma)J/\psi(e^+e^-)$

Channel	N_{gen}	$\varepsilon(\%)$	$N_{sca.}$
$\psi(2S) \rightarrow \gamma\chi_{c0} \rightarrow \gamma\gamma J/\psi(e^+e^-)$	2.0×10^5	2.46	173
$\psi(2S) \rightarrow \gamma\chi_{c1} \rightarrow \gamma\gamma J/\psi(e^+e^-)$	4.0×10^5	0.15	304
$\psi(2S) \rightarrow \gamma\chi_{c2} \rightarrow \gamma\gamma J/\psi(e^+e^-)$	4.0×10^5	0.53	571
$\psi(2S) \rightarrow \gamma\gamma J/\psi \rightarrow \gamma\gamma e^+e^-$	1.4×10^6	0.78	16
Total number			1064

 Table 4.2 Summary of the background decays for $\psi(2S) \rightarrow \pi^0(\gamma\gamma)J/\psi(\mu^+\mu^-)$

Channel	N_{gen}	$\varepsilon(\%)$	$N_{sca.}$
$\psi(2S) \rightarrow \gamma\chi_{c0} \rightarrow \gamma\gamma J/\psi(\mu^+\mu^-)$	2.0×10^5	3.08	233
$\psi(2S) \rightarrow \gamma\chi_{c1} \rightarrow \gamma\gamma J/\psi(\mu^+\mu^-)$	6.0×10^5	0.16	328
$\psi(2S) \rightarrow \gamma\chi_{c2} \rightarrow \gamma\gamma J/\psi(\mu^+\mu^-)$	6.0×10^5	0.58	608
$\psi(2S) \rightarrow \gamma\gamma J/\psi \rightarrow \gamma\gamma\mu^+\mu^-$	4.0×10^5	3.49	70
Total number			1239

4.1.2 Fit to mass spectrum of π^0 in data

The signal yields are obtained by performing a fit to the distribution of two photon invariant mass ($m_{\gamma\gamma}$). Figure 4.9 shows the comparison of the distribution of $m_{\gamma\gamma}$ between MC and data for the $\psi(2S) \rightarrow \pi^0 J/\psi(e^+e^-)$ and $\psi(2S) \rightarrow \pi^0 J/\psi(\mu^+\mu^-)$. Except for the signal decay channel, the MC sample also include the main backgrounds mentioned before, the event number of MC sample has scaled to that of data. The π^0 MC line shape is consistent with data, but the resolution of MC better than that of data. In fitting to the data, we use the π^0 line shape obtained from MC simulation. To account for differences between the data and MC, the line shape is modified by convoluting with a

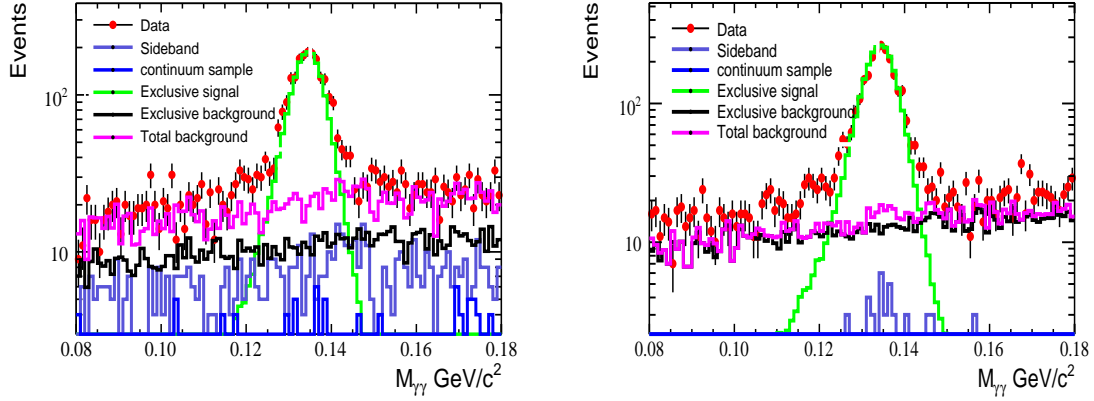


Figure 4.7 The distribution of two photon mass for the data. The red error points are for data, the blue histogram is for the continuum sample, the light blue histogram is the contribution of the sideband around J/ψ in the data sample, the green histogram and the black histogram are the Exclusive signal MC sample and Exclusive background MC sample, respectively; And the pink is the total background. left: for $\psi(2S) \rightarrow \pi^0(\gamma\gamma)J/\psi(e^+e^-)$; right: for $\psi(2S) \rightarrow \pi^0(\gamma\gamma)J/\psi(\mu^+\mu^-)$.

Gaussian function, i.e. the PDF is taken as $\text{PDF} = \text{PDF}(\pi^0) \otimes \text{Gaussian}(m_{\gamma\gamma} - \delta m, \sigma) + bg$, where δm and σ correct the π^0 mass and resolution, respectively, in simulation, and bg denotes backgrounds, which includes the known background contributions obtained from MC simulation and unknown background contributions modeled as the first order of polynomial. The fitting results are shown in figure 4.10. The fit yields 1823 ± 49 events for the $\psi(2S) \rightarrow \pi^0(\gamma\gamma)J/\psi(e^+e^-)$ with $\chi^2/ndf = 0.85$, and 2268 ± 55 events for $\psi(2S) \rightarrow \pi^0(\gamma\gamma)J/\psi(\mu^+\mu^-)$ with $\chi^2/ndf = 0.86$.

The detection efficiencies are determined with the MC simulation on the $\psi(2S) \rightarrow \pi^0 J/\psi$ and $J/\psi \rightarrow e^+e^-/\mu^+\mu^-$ decays, the amplitude information is used in event generation. Figure 4.8 shows the angular distribution of J/ψ and the helicity angle distribution of e or μ with the requirement that the mass of the two photons must be within the mass window of π^0 , from $0.125 \text{ GeV}/c^2$ to $0.145 \text{ GeV}/c^2$. Here the helicity angle is defined as the angle between the lepton momentum in J/ψ CM system and the J/ψ momentum in $\psi(2S)$ CM system. The angular distributions agree with each other between the data and MC. To reduce the uncertainty from the kinematic fit, the detector efficiencies are determined with the charged track parameter correction (see section 4.3.3), which are determined to be $(23.05 \pm 0.05)\%$ and $(29.11 \pm 0.06)\%$ for $J/\psi \rightarrow e^+e^-$ and $J/\psi \rightarrow \mu^+\mu^-$,

respectively.

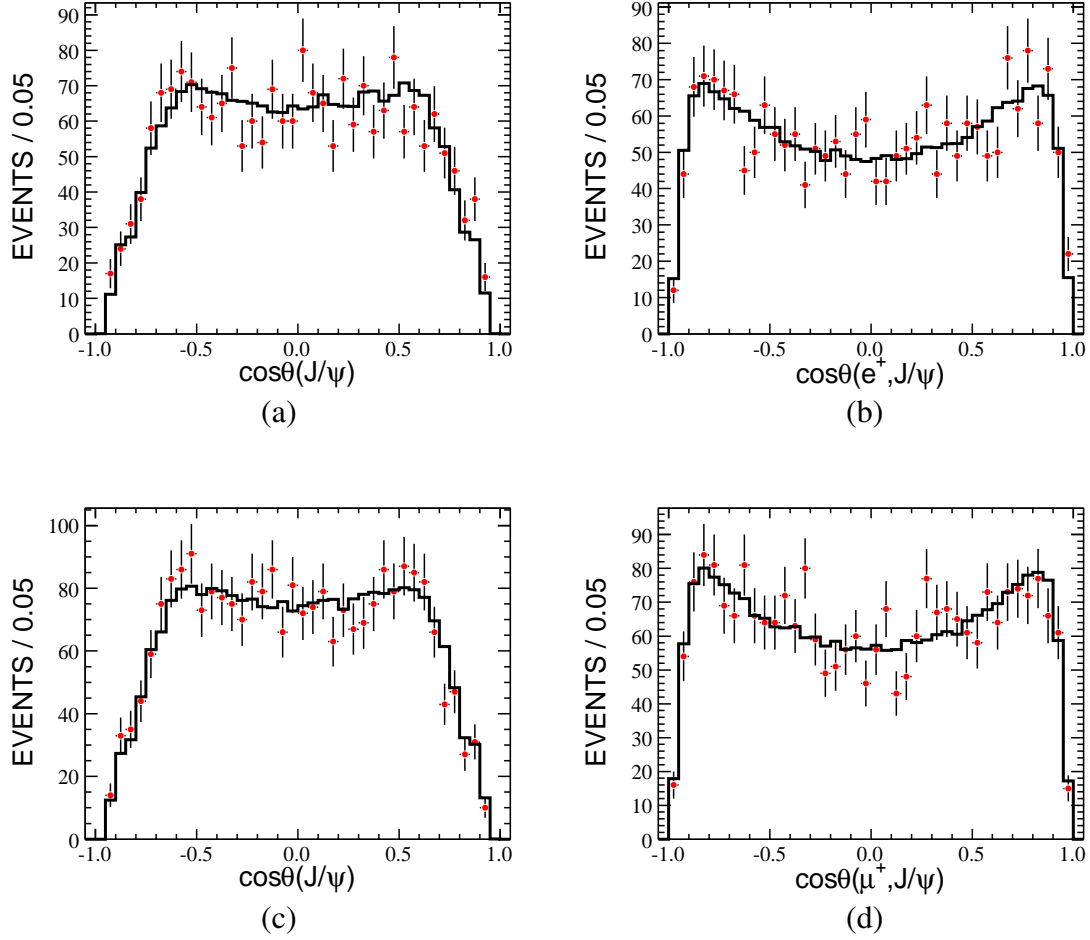


Figure 4.8 Comparison of angular distributions between exclusive MC sample and Data sample. (a) and (b) are for $\psi(2S) \rightarrow \pi^0(\gamma\gamma)J/\psi(e^+e^-)$; (c) and (d) are for $\psi(2S) \rightarrow \pi^0(\gamma\gamma)J/\psi(\mu^+\mu^-)$. Here the angle $\cos\theta(J/\psi)$ is the angular distribution of J/ψ in $\psi(2S)$ CM system, and the helicity angle $\cos\theta(l^-, J/\psi)$ is defined as the angle between the lepton (l^-) momentum in J/ψ CM system and the J/ψ momentum in $\psi(2S)$ CM system.

The branching fraction is calculated with

$$Br[\psi(2S) \rightarrow \pi^0 J/\psi] = \frac{N^{obs}}{N_{\psi(2S)}\epsilon Br(\pi^0 \rightarrow \gamma\gamma)Br(J/\psi \rightarrow l^+l^-)} \quad (4-1)$$

where N^{obs} and ϵ are the signal yields and the detection efficiency, respectively. $N_{\psi(2S)}$ is the total decays of $\psi(2S)$, and $N_{\psi(2S)} = 106 \times 10^6$. The branching fractions are calculated to be $(1.267 \pm 0.034) \times 10^{-3}$ and $(1.250 \pm 0.030) \times 10^{-3}$ for $J/\psi \rightarrow e^+e^-$, and $J/\psi \rightarrow \mu^+\mu^-$,

for $J/\psi \rightarrow e^+e^-$, and $J/\psi \rightarrow \mu^+\mu^-$, respectively. Here the errors are statistical only.

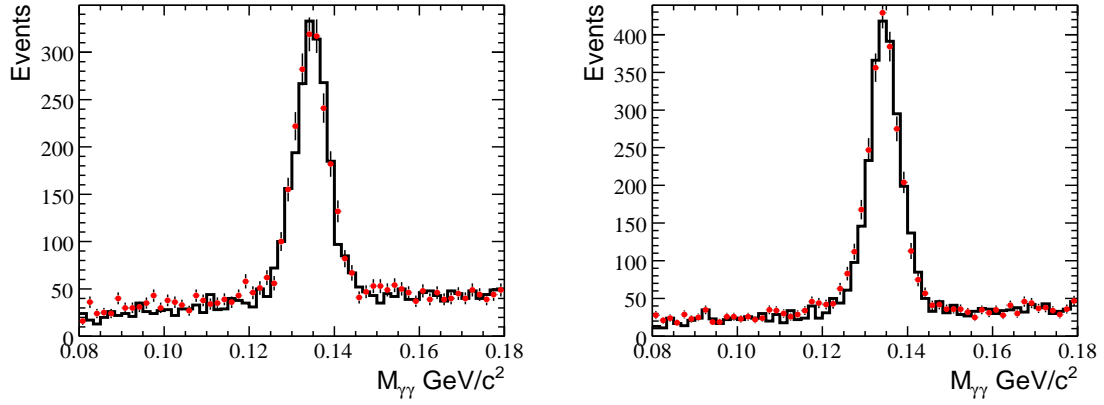


Figure 4.9 The comparison of the mass of the two photons between MC sample and Data sample. The red error bars are data results, while the black histogram is MC sample. Left: for $\psi(2S) \rightarrow \pi^0(\gamma\gamma)J/\psi(e^+e^-)$. Right: for $\psi(2S) \rightarrow \pi^0(\gamma\gamma)J/\psi(\mu^+\mu^-)$.

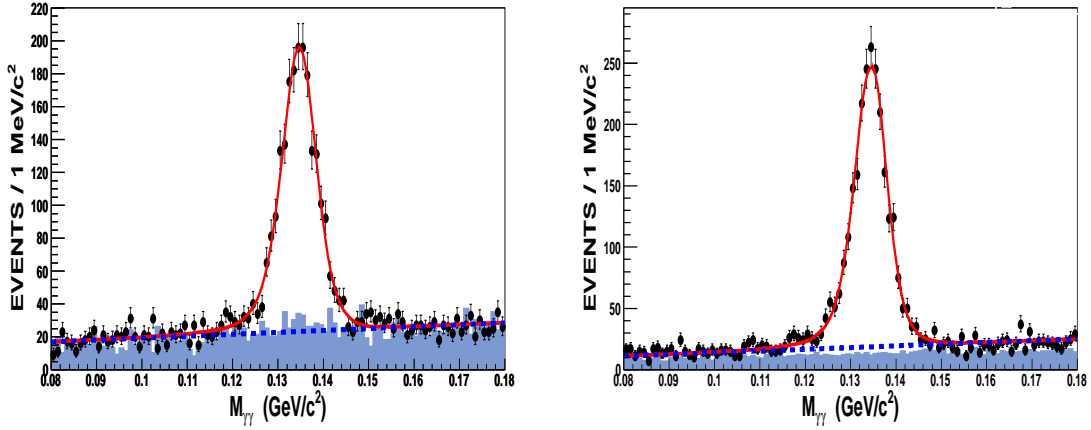


Figure 4.10 The fitting result for data. The signal is described by exclusive signal MC-shape convoluted with a Gaussian function, while the background is described by background MC-shape plus a 1-order polynomial function. Left: for $\psi(2S) \rightarrow \pi^0(\gamma\gamma)J/\psi(e^+e^-)$. Right: for $\psi(2S) \rightarrow \pi^0(\gamma\gamma)J/\psi(\mu^+\mu^-)$.

4.2 $\psi(2S) \rightarrow \eta(\gamma\gamma)J/\psi(l^+l^-)$

4.2.1 Event selection and background study

4.2.1.1 General selection criteria

The final states of this decay are the same as that of $\psi(2S) \rightarrow \pi^0 J/\psi(l^+l^-)$, including two photons and two leptons, so the charged tracks and photons are selected with the same selection criteria as in the previous analysis. The η candidates are reconstructed with the two selected photons. After the good charged tracks and photons are selected, it is required that the number of the good photons must be greater than two and the number of good charged tracks reconstructed in MDC must be equal to two with net charge zero. Figure 4.11 shows the comparison of the number of good photons between MC and data. One can see that the N_γ distribution of MC and data are in a good agreement.

In order to improve the resolution and to suppress the background, the 4C-kinematical fit has been imposed on the $\psi(2S) \rightarrow \gamma\gamma l^+l^-$ hypothesis by looping over all selected photon candidates, where $l = e$ or μ . After test all the combinations, the combination of $\gamma\gamma l^+l^-$ with a minimum χ^2 value will be survival. Figures 4.12 and 4.13 shows the χ^2 distributions for $\psi(2S) \rightarrow \gamma\gamma e^+e^-$ and $\psi(2S) \rightarrow \gamma\gamma \mu^+\mu^-$, respectively. The χ^2 distribution of data is consistent with that of MC.

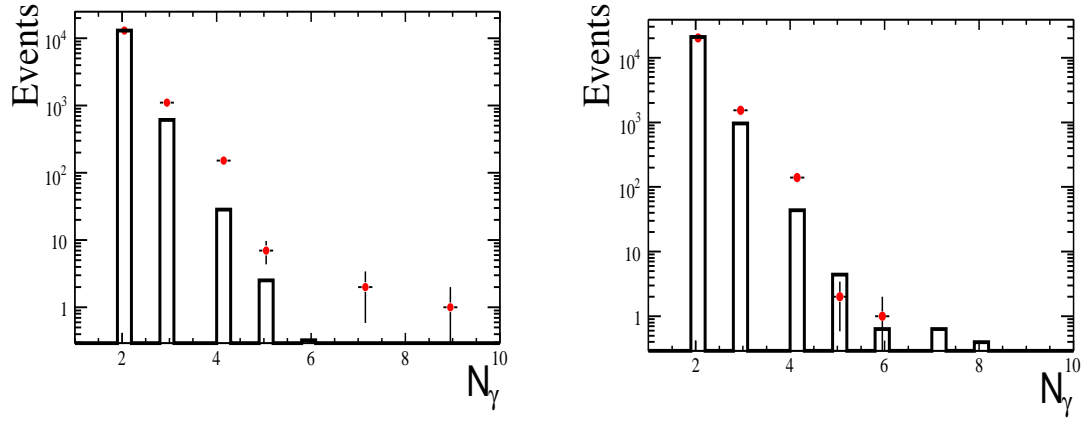


Figure 4.11 The number of good photon distribution for $\psi(2S) \rightarrow \eta J/\psi$. Left: $J/\psi \rightarrow e^+e^-$. Right: $J/\psi \rightarrow \mu^+\mu^-$

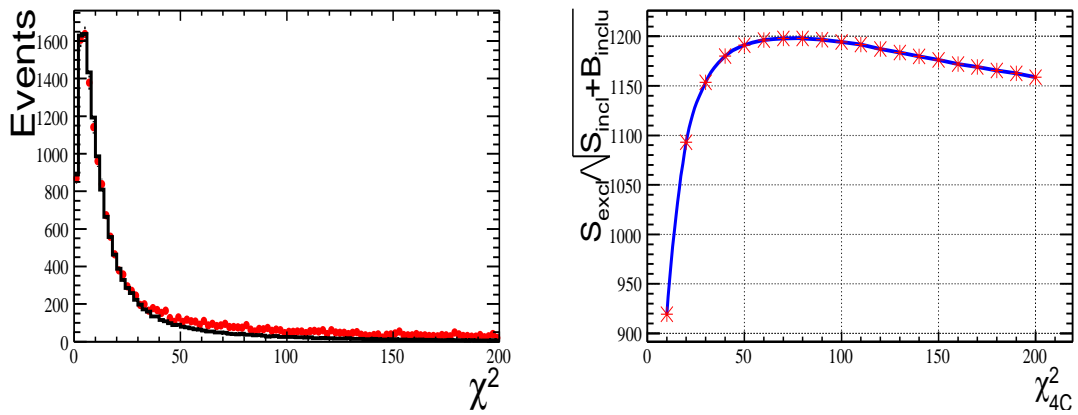


Figure 4.12 The χ^2 distribution for $\psi(2S) \rightarrow \eta J/\psi(e^+e^-)$. Left: The χ^2 distribution. Right: The optimization of the χ^2 .

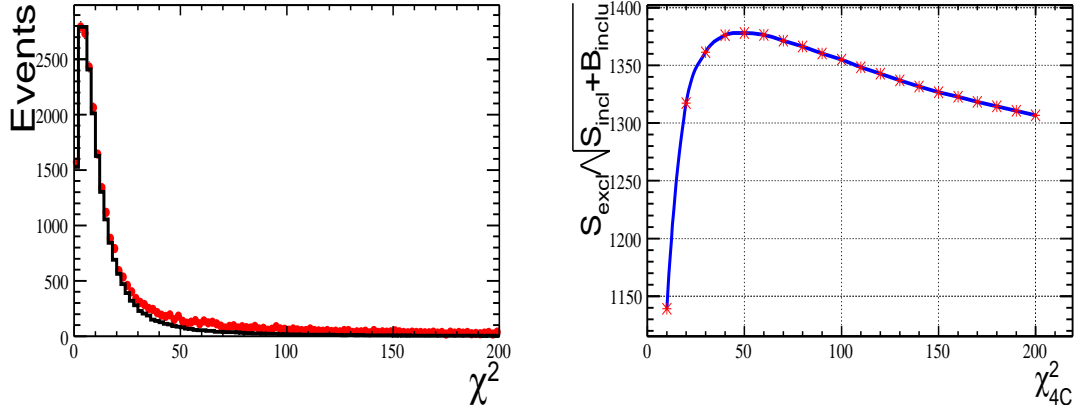


Figure 4.13 The χ^2 distribution for $\psi(2S) \rightarrow \eta J/\psi(\mu^+\mu^-)$. Left: The χ^2 distribution. Right: The optimization of the χ^2 .

4.2.1.2 Final Selection and background study

As in the previous analysis, electron and muon candidates are identified using the E/p ratio. Figure 4.14 shows the distribution of the invariant mass of the selected lepton pairs (electron or muon). In order to constrain the two leptons produced from J/ψ decays, it is required the invariant mass of these two leptons is larger than $3.05 \text{ GeV}/c^2$ and less than $3.15 \text{ GeV}/c^2$. To suppress the backgrounds from the J/ψ hadronic decays, e.g. $J/\psi \rightarrow \pi^0 n(\pi^+\pi^-)$ ($n = 1, 2, 3$), it is required that $\chi^2 < 70$ for $\psi(2S) \rightarrow \gamma\gamma e^+e^-$ and $\chi^2 < 50$ for $\psi(2S) \rightarrow \gamma\gamma\mu^+\mu^-$. The χ^2 cuts are determined by optimizing the χ^2 distribution as shown in figure 4.12 and figure 4.13.

As shown in figure 4.6, the dominant backgrounds come from decays of $\psi(2S) \rightarrow \gamma\chi_{c1,2}$. Due to the large mass difference between π^0 and η , the contamination from $\psi(2S) \rightarrow \pi^0 J/\psi$ is negligible. Potential background is studied using the 106 M $\psi(2S)$ generic MC sample. Events are selected with the same selection criteria as applied to the data. It is found that the decay $\psi(2S) \rightarrow \pi^0\pi^0 J/\psi$ and $\psi(2S) \rightarrow \gamma\gamma J/\psi$ can also contribute background events. These decays are exclusively simulated, and then normalized to the $\psi(2S)$ data with the branching fractions available from PDG^[10]. The non-resonant background is estimated with the J/ψ sideband cut. The contribution of each background component to the $m_{\gamma\gamma}$ spectrum is plotted in figure 4.15, where the red points with error bars are data, and the color histograms are the exclusive MC, and the QED backgrounds estimated with the continuum data taken at 3.65 GeV , and the sideband contribution are

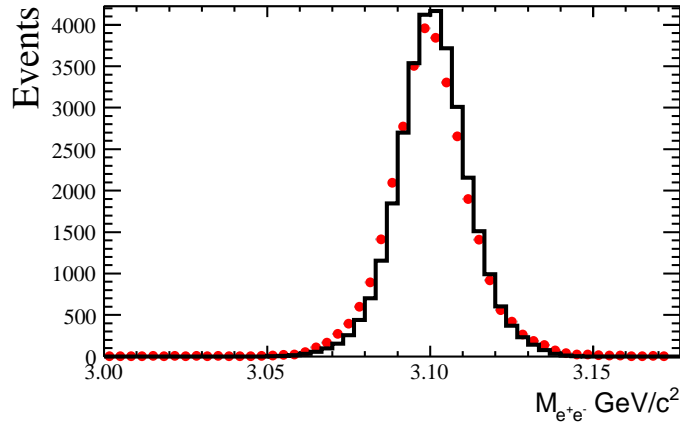


Figure 4.14 The invariant-mass distribution of leptons for data vs MC for $\psi(2S) \rightarrow \eta(\gamma\gamma)J/\psi(l^+l^-)$. The red error bars are the data results, the black histograms are the MC results.

also shown in the plot. The number of background events and the decay modes are listed in table 4.3 and table 4.4, where N_{gen} is total number of exclusive MC sample, $N_{sca.}$ is the expected number of background events in the $\psi(2S)$ data sample, and ε is the detection efficiency. The total number of observed background events are 4305 and 4231 for $\psi(2S) \rightarrow \eta(\gamma\gamma)J/\psi(e^+e^-)$ and $\psi(2S) \rightarrow \eta(\gamma\gamma)J/\psi(\mu^+\mu^-)$, respectively.

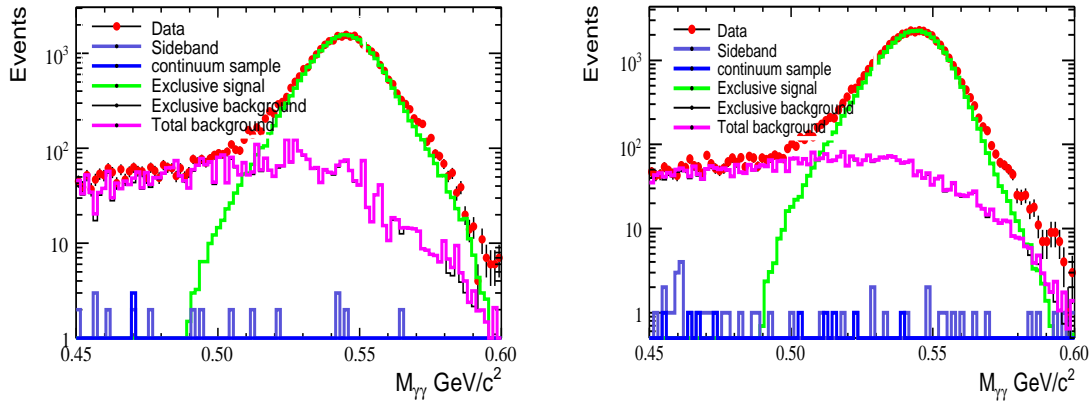


Figure 4.15 The distribution of two γ mass for data and background. The red error points are for data, the blue histogram is for the continuum sample, the light blue histogram is the contribution of the sideband around J/ψ in the data sample, the green histogram and the black histogram are the Exclusive signal MC samples and Exclusive background MC sample, respectively; And the pink is the total background. Left: for $\psi(2S) \rightarrow \eta(\gamma\gamma)J/\psi(e^+e^-)$; Right: for $\psi(2S) \rightarrow \eta(\gamma\gamma)J/\psi(\mu^+\mu^-)$;

According to the above analysis, the final selection criteria are set as follows:

- $2 \leq N_\gamma \leq 4$;
- $E/p > 0.8$ (for electron), $E/p > 0.08$ and $E/p < 0.22$ (for muon);
- $\chi_{4c}^2 < 70$ for $\gamma\gamma e^+e^-$, and $\chi_{4c}^2 < 50$ for $\gamma\gamma\mu^+\mu^-$;
- $3.05 \text{ GeV}/c^2 < M_{l^+l^-} < 3.15 \text{ GeV}/c^2$;
- $M_{\gamma 1, J/\psi} < 3.50 \text{ GeV}/c^2$.

Table 4.3 Summary of the background decays for $\psi(2S) \rightarrow \eta(\gamma\gamma)J/\psi(e^+e^-)$

Channel	N_{gen}	$\varepsilon(\%)$	$N_{sca.}$
$\psi(2S) \rightarrow \gamma\chi_{c0} \rightarrow \gamma\gamma J/\psi(e^+e^-)$	2.0×10^5	11.28	793
$\psi(2S) \rightarrow \gamma\chi_{c1} \rightarrow \gamma\gamma J/\psi(e^+e^-)$	4.0×10^5	0.37	740
$\psi(2S) \rightarrow \pi^0\pi^0 J/\psi \rightarrow \gamma\gamma J/\psi(e^+e^-)$	4.0×10^6	0.25	2728
$\psi(2S) \rightarrow \gamma\gamma J/\psi \rightarrow \gamma\gamma e^+e^-$	1.4×10^6	2.17	44
Total number			4305

Table 4.4 Summary of the background decays for $\psi(2S) \rightarrow \eta(\gamma\gamma)J/\psi(\mu^+\mu^-)$

Channel	N_{gen}	$\varepsilon(\%)$	$N_{sca.}$
$\psi(2S) \rightarrow \gamma\chi_{c0} \rightarrow \gamma\gamma J/\psi(\mu^+\mu^-)$	2.0×10^5	14.75	1115
$\psi(2S) \rightarrow \gamma\chi_{c1} \rightarrow \gamma\gamma J/\psi(\mu^+\mu^-)$	6.0×10^5	0.30	590
$\psi(2S) \rightarrow \pi^0\pi^0 J/\psi \rightarrow \gamma\gamma J/\psi(\mu^+\mu^-)$	1.2×10^6	0.23	2345
$\psi(2S) \rightarrow \gamma\gamma J/\psi \rightarrow \gamma\gamma\mu^+\mu^-$	4.0×10^5	9.02	181
Total number			4231

4.2.2 Fit to mass spectrum of η in Data

The signal yields are obtained by performing a fit to the distribution of two photon invariant mass ($m_{\gamma\gamma}$). Figure 4.17 shows the comparison of the distribution of $m_{\gamma\gamma}$ between MC and data for the $\psi(2S) \rightarrow \eta J/\psi(e^+e^-)$ and $\psi(2S) \rightarrow \eta J/\psi(\mu^+\mu^-)$. Except for the signal decay channel, the MC sample also include the main backgrounds mentioned before, the event number of MC sample has scaled to that of data. One can see that the

resolution of MC is better than data. In fitting to the data, we use the η line shape obtained from MC simulation. To account for the difference between the data and MC, the η line shape is modified by convoluting with a Gaussian function, i.e. the PDF is taken as $\text{PDF} = \text{PDF}(\eta) \otimes \text{Gaussian}(m_{\gamma\gamma} - \delta m, \sigma) + bg$, where δm and σ correct the η mass and resolution, respectively, in simulation, and bg denotes background, which includes the known background obtained from MC simulation and unknown background modeled as the second order of polynomial function. The fitting results are shown in Figure 4.18. The fit yields 29598 ± 202 events for the $\psi(2S) \rightarrow \eta(\gamma\gamma)J/\psi(e^+e^-)$ with $\chi^2/ndf = 1.33$, and 38572 ± 280 events for $\psi(2S) \rightarrow \eta(\gamma\gamma)J/\psi(\mu^+\mu^-)$ with $\chi^2/ndf = 0.96$.

The detection efficiencies are determined with the MC simulation on the $\psi(2S) \rightarrow \eta J/\psi$ and $J/\psi \rightarrow e^+e^-/\mu^+\mu^-$ decays, in which the helicity amplitude information is used. Figure 4.16 shows the angular distribution of J/ψ and the helicity angle distribution of e or μ with the requirement that the mass of the two photons must be within the mass window of η , from $0.52\text{GeV}/c^2$ to $0.60\text{GeV}/c^2$. Here the helicity angle is defined as the angle between the lepton momentum in J/ψ CM system and the J/ψ momentum in $\psi(2S)$ CM system. The angular distributions are in good agreement with each other between the data and MC. To reduce the uncertainty from the kinematic fit, the detector efficiencies are determined with the charged track parameter correction (see section 4.3.3), which are determined to be $(35.41 \pm 0.06)\%$ and $(46.28 \pm 0.06)\%$ for $J/\psi \rightarrow e^+e^-$ and $\mu^+\mu^-$, respectively.

The branching fraction is calculated with

$$Br[\psi(2S) \rightarrow \eta J/\psi] = \frac{N^{obs}}{N_{\psi(2S)} \epsilon Br(\eta \rightarrow \gamma\gamma) Br(J/\psi \rightarrow l^+l^-)} \quad (4-2)$$

where N^{obs} and ϵ are the signal yields and the detection efficiency, respectively. $N_{\psi(2S)}$ is the total decays of $\psi(2S)$, and $N_{\psi(2S)} = 106 \times 10^6$. The branching fractions are calculated to be $(33.77 \pm 0.23) \times 10^{-3}$ and $(33.73 \pm 0.24) \times 10^{-3}$ for $J/\psi \rightarrow e^+e^-$, and $J/\psi \rightarrow \mu^+\mu^-$, respectively. Here the errors are statistical only.

4.3 Source of systematic error

The Sources of systematic errors are including the several items as listed below:

- Total number of $\psi(2S)$,
- Trigger Efficiency,

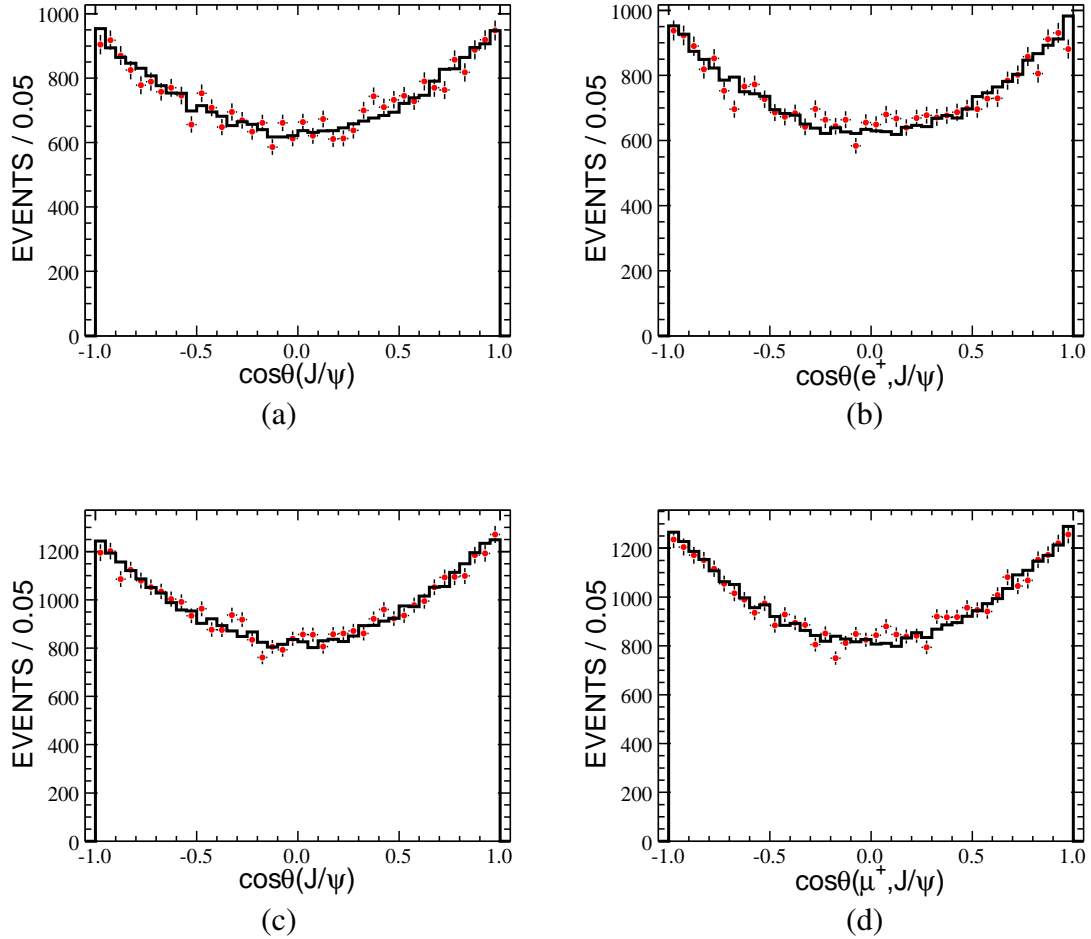


Figure 4.16 The comparison of angular distributions between exclusive MC sample and Data sample. (a) and (b) are for $\psi(2S) \rightarrow \eta(\gamma\gamma)J/\psi(e^+e^-)$; (c) and (d) are for $\psi(2S) \rightarrow \eta(\gamma\gamma)J/\psi(\mu^+\mu^-)$. Here the angle $\cos\theta(J/\psi)$ is the angular distribution of J/ψ in $\psi(2S)$ CM system, and the helicity angle $\cos\theta(l^-, J/\psi)$ is defined as the angle between the lepton (l^-) momentum in J/ψ CM system and the J/ψ momentum in $\psi(2S)$ CM system.

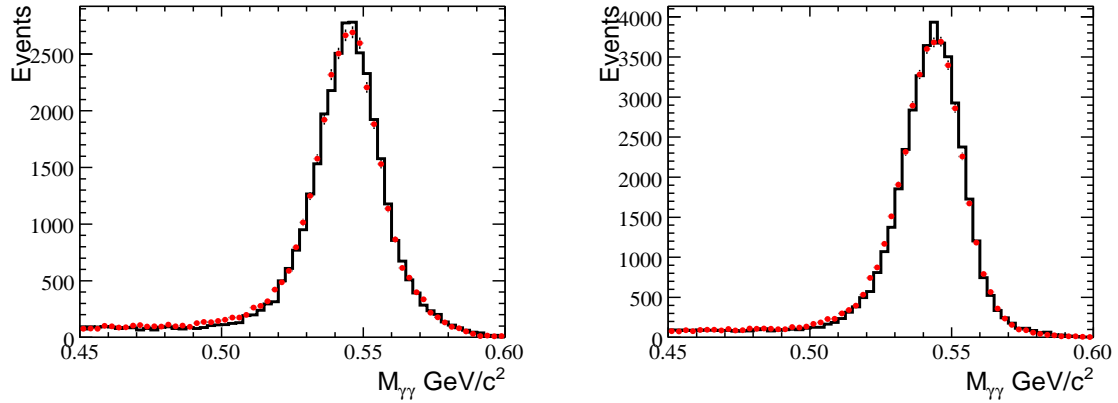


Figure 4.17 The comparison of the mass of the two photons between MC sample and Data sample. The red error bars are data results, while the black histogram is MC sample. Left: for $\psi(2S) \rightarrow \eta(\gamma\gamma)J/\psi(e^+e^-)$. Right: for $\psi(2S) \rightarrow \eta(\gamma\gamma)J/\psi(\mu^+\mu^-)$.

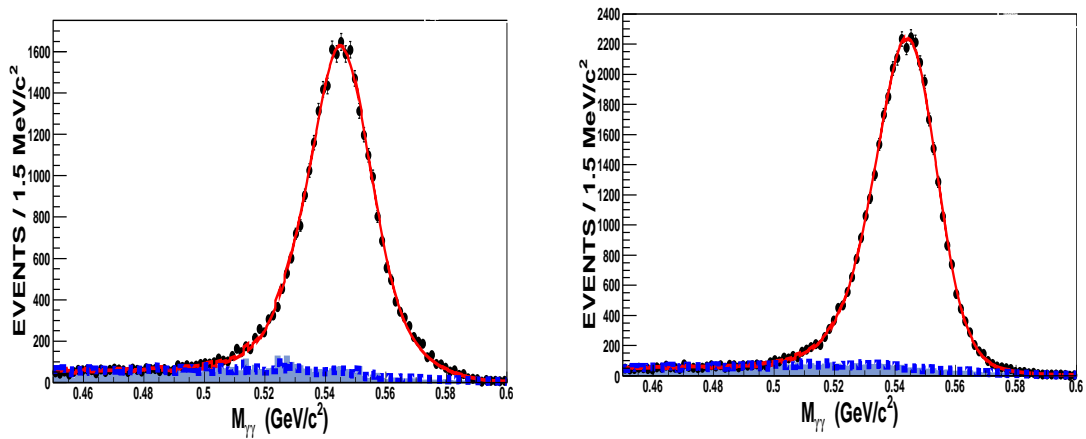


Figure 4.18 The comparison of the mass of the two photons between exclusive MC sample and Data sample. Left: for $\psi(2S) \rightarrow \eta(\gamma\gamma)J/\psi(e^+e^-)$. Right: for $\psi(2S) \rightarrow \eta(\gamma\gamma)J/\psi(\mu^+\mu^-)$.

- Tracking Efficiency for e/μ ,
- Photon reconstruction efficiency for π^0/η ,
- 4C Kinematic Fitting,
- Branching ratio of $J/\psi \rightarrow e^+e^-/\mu^+\mu^-$,
- Branching ratio $\pi^0/\eta \rightarrow \gamma\gamma$,
- E/p,
- Mass(2 leptons),
- Mass(γ 2 leptons),
- Fitting range,
- Fitting Function for Background.

4.3.1 Total number of $\psi(2S)$

The error of the total number of $\psi(2S)$ is 0.71% , which comes from Wangzhiyong's work^[93].

4.3.2 Tracking Efficiency

In the following section differences in the tracking efficiencies between data and MC simulation are studied for the estimation of systematic errors. The tracking efficiency of leptons is studied using the decay channel $\psi(2S) \rightarrow \pi^+\pi^- J/\psi$, $J/\psi \rightarrow l^+l^-$ ($l = e, \mu$). The tracking efficiency of data is studied using the full 106M $\psi(2S)$ data set, for exclusive MC separate samples of 500K events for $l = e, \mu$ were generated, for inclusive MC a sample of 100M events of $\psi(2S) \rightarrow anything$ was used.

The tracking efficiency ϵ is calculated with

$$\epsilon = N_{full}/N_{all}$$

where N_{full} indicates the number of events of $\pi^+\pi^-l^+l^-$ with all final tracks reconstructed successfully; N_{all} indicates the number of events with one or both charged lepton tracks successfully reconstructed in addition to the pion-pair. In the case if one charged track is lost identification of the decay channel is still possible and the information on the missing track is available from the missing momenta method: $p_{l,missing} = p_{\psi(2S)} - p_{\pi^+} - p_{\pi^-} - p_{l,detected}$, where p is a 4-momentum of the particle.

The following event selection criteria are applied:

- No photons have to be present.

- At least three charged tracks.
- Two of the charged tracks have to be identified as pion.
- Invariant mass of a pion pair $M_{\pi^+\pi^-}$ has to be in the range of $[0.35, 0.65] \text{ GeV}/c^2$.
- Recoil mass of the pion pair $M_{\pi^+\pi^- \text{ recoil}}$ has to be in the range of $[3.07, 3.115] \text{ GeV}/c^2$.
- Lepton identification is based on ratio of deposited energy measured in EMC to the momentum measured in MDC (E/p): track is labeled as electron if its $E/p > 0.8$ and as muon if $0.08 < E/p < 0.22$.

In the case of muon identification requirement $0.08 < E/p < 0.22$ can introduce additional systematic error, since E/p for kaons and protons is in the same range. In order to cut away possible background from misidentified charged tracks from other two-body decays of J/ψ , such as $J/\psi \rightarrow K\bar{K}^*(892)$ (see Fig. 4.19) additional requirement for muons was introduced: momentum of detected muon in the rest frame of reconstructed J/ψ should be bigger than $1.45 \text{ GeV}/c$.

This selection leaves a relatively pure sample, which is then divided into angular or transverse momentum (p_t) bins. The number of events in each bin is estimated using a fitting procedure: event histograms of recoil mass of the pion pair, $M_{\pi^+\pi^- \text{ recoil}}$ are fitted with double Gaussian for the signal plus zero-order polynomial for the background (the polynomial fit is shown on figure 4.20) and then the integral of the polynomial is subtracted from the total number of events. This is done separately for e and μ candidates.

A comparison of efficiencies reconstructed from the recoil and from the identified tracks is shown in figure 4.21 and figure 4.22. The resulting efficiency curves show a slightly lower efficiency for data than for simulation, an effect which is more pronounced at low transverse momenta.

In order to investigate the size of the discrepancies over the whole phase space, MC events have been divided into p_t and $|\cos\theta|$ bins. The maps of $\epsilon_{Data}/\epsilon_{MC}$ for electrons and muons and maps of statistical errors are shown on figure 4.23 and figure 4.24, respectively. Bins have non-uniform width: regions with the same values of $\epsilon_{Data}/\epsilon_{MC}$ share the same bin in order to minimize the statistical error per bin. Note from the figures that there are a few bins for which we could not determine the efficiency, since the channel $\psi(2S) \rightarrow \pi^+\pi^- J/\psi (J/\psi \rightarrow l^+l^-)$ does not cover that part of the phase space. The coverage in phase space is comparable for the channel of interest as shown on figure 4.25. We,

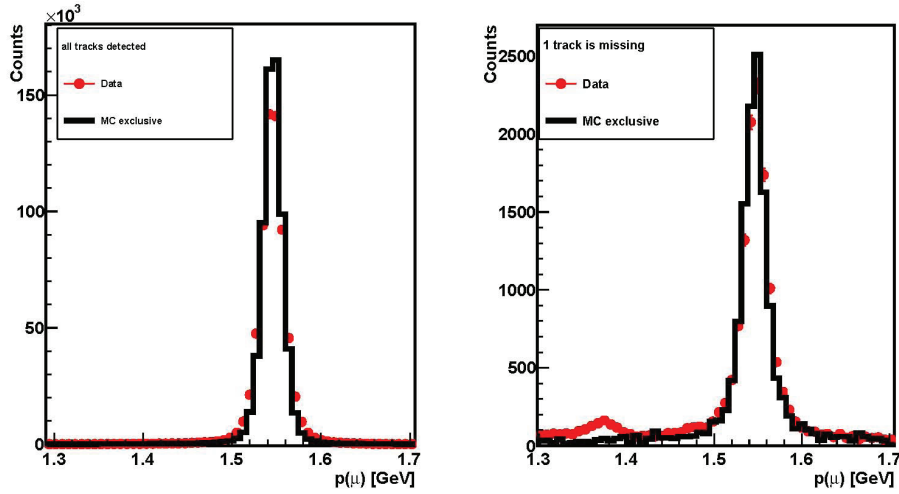


Figure 4.19 Momentum of identified muon in the rest frame of reconstructed J/ψ . Left: in the case if all charged tracks are detected, right: 1 charged track is missing. Red dots represent beam data, black histogram is exclusive MC.

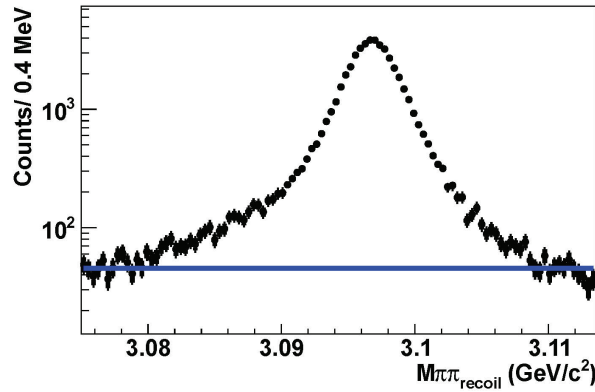


Figure 4.20 The recoil mass spectrum of a pion pair (dots). Estimated background is fitted with polynomial function (blue).

therefore, can safely ignore the bins with a missing efficiency.

Systematic error of the tracking was estimated using the formula

$$\Delta = \frac{\sum_{ij} f_{ij} N_{ij}}{N}$$

where indexes ij stand for p_t and $|\cos\theta|$ bins, $f_{ij} = 1 - (\epsilon_{Data}/\epsilon_{MC})_{ij}$, N_{ij} is a number of events in a histogram bin, $N = \sum_{ij} N_{ij}/\epsilon_{Data,ij}$ is a total number of events in a histogram.

Table 4.5 shows the summary of corrected efficiencies and their systematic errors. The influence of the choice of the choice of background function was studied. In the case

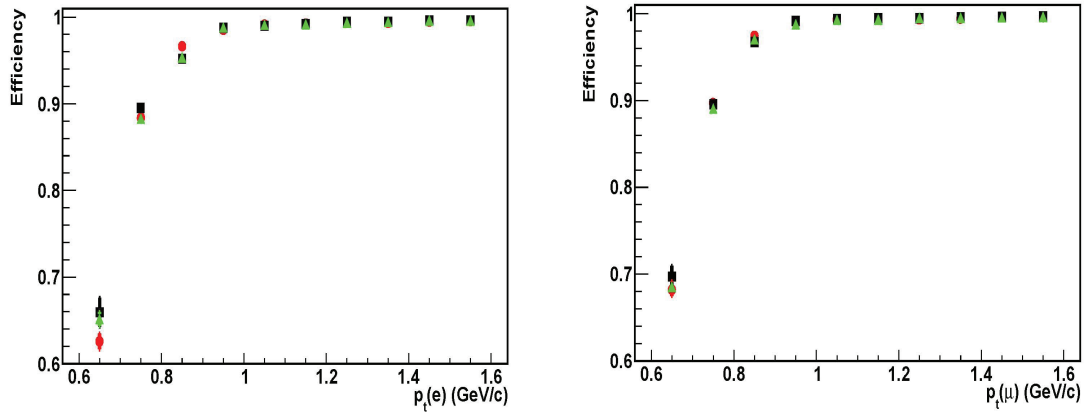


Figure 4.21 Tracking efficiency vs p_t for (a) electrons and (b) muons. Red points are data, black squares are exclusive MC and green triangles are inclusive MC. Errors in efficiency are statistical errors.

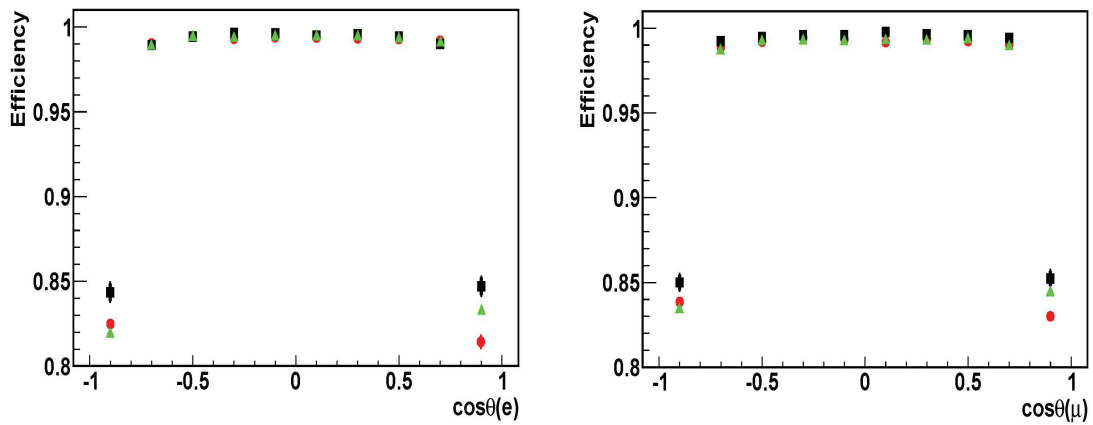


Figure 4.22 Tracking efficiency vs $\cos\theta$ for (a) electrons and (b) muons. Red points are data, black squares are exclusive MC and green triangles are inclusive MC. Errors in efficiency are statistical errors.

if no background subtraction was performed the difference between corrected efficiencies was smaller than the systematic error.

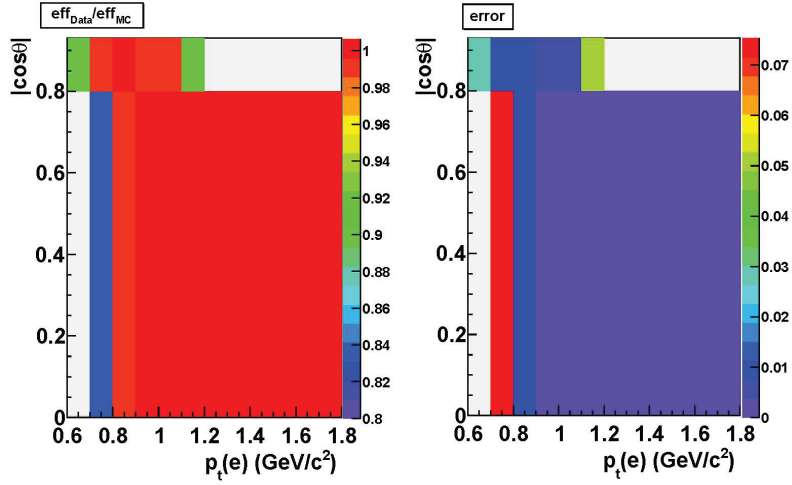


Figure 4.23 Map of $\epsilon_{Data}/\epsilon_{MC}$ for exclusive MC for electrons (left) and its error (right).

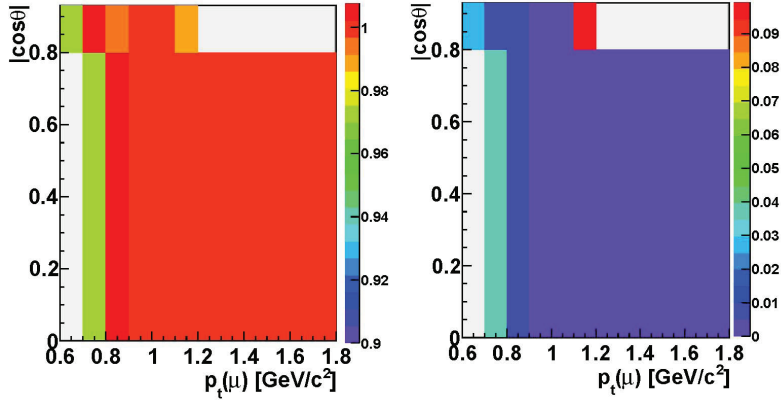


Figure 4.24 Map of $\epsilon_{Data}/\epsilon_{MC}$ for exclusive MC for muons (left) and its error (right).

Table 4.5 Systematic error due to the tracking efficiency for the branching ratios of the channels of interest

Model	$\psi(2S) \rightarrow \eta J/\psi$	$\psi(2S) \rightarrow \pi^0 J/\psi$
Final states	$\gamma\gamma e^+e^-$ $\gamma\gamma\mu^+\mu^-$	$\gamma\gamma e^+e^-$ $\gamma\gamma\mu^+\mu^-$
Systematic error (%)	0.16 0.19	0.14 0.20

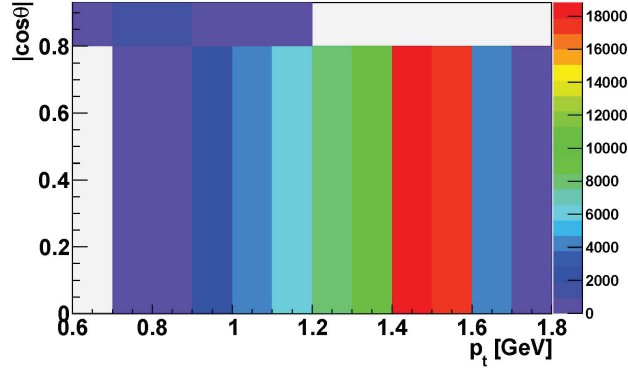


Figure 4.25 Original distribution of events with respect to p_t and $|\cos\theta|$ for the channel $\psi(2S) \rightarrow \eta J/\psi (J/\psi \rightarrow e^+e^-)$.

4.3.3 4C Kinematic Fitting

The method to estimate the uncertainty of 4C kinematic fitting is same as used for the chapter 2. In this section, $\psi(2S) \rightarrow \pi^+\pi^- J/\psi (e^+e^-/\mu^+\mu^-)$ are selected as the control sample to extract the correction factors of μ^\pm and e^\pm from their pull distributions. The detailed information on this method is described in appendix A.1.3. Table 4.6 shows the correction factors. The MC sample after correction are used to estimate the efficiency and fit the invariant mass spectrum.

Table 4.6 Correction factors extracted from the pull distribution

	ϕ_0		κ		$\tan \lambda$	
	$m^{data} - m^{MC}$	$\sigma^{data}/\sigma^{MC}$	$m^{data} - m^{MC}$	$\sigma^{data}/\sigma^{MC}$	$m^{data} - m^{MC}$	$\sigma^{data}/\sigma^{MC}$
μ^+	0.003	1.273	0.092	1.218	0.579	1.255
μ^-	0.037	1.275	-0.030	1.220	0.578	1.264
e^+	-0.001	1.207	0.137	1.117	0.578	1.186
e^-	0.037	1.202	-0.065	1.101	0.579	1.179

Figure 4.26 shows the distributions between MC and data for $\psi(2S) \rightarrow \pi^0 J/\psi (e^+e^-/\mu^+\mu^-)$. The left figure is the distribution for $\psi(2S) \rightarrow \pi^0 J/\psi (e^+e^-)$, while the right one is for $\psi(2S) \rightarrow \pi^0 J/\psi (\mu^+\mu^-)$. The correction parameters are obtained from the control sample, whose details are described in Appendix A.1.3.

Similarly, figure 4.27 shows the χ^2 distributions of MC and data for $\psi(2S) \rightarrow \eta J/\psi (e^+e^-/\mu^+\mu^-)$. The detection efficiencies for the χ^2 cut value for different decay

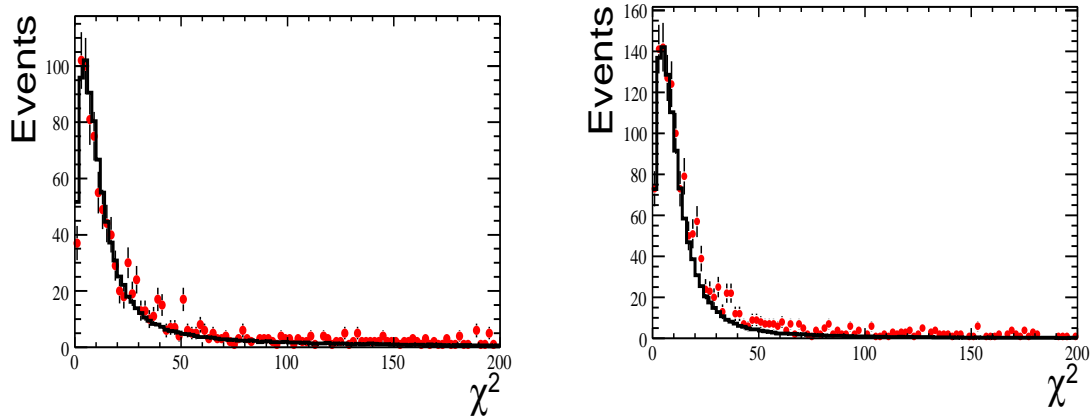


Figure 4.26 A comparison of χ^2 between MC and data for $\psi(2S) \rightarrow \pi^0 J/\psi$. The red error dots are data, the black histogram is MC. Left: $J/\psi \rightarrow e^+ e^-$; Right: $J/\psi \rightarrow \mu^+ \mu^-$

modes are listed in table 4.7, where ε_1 is the efficiency before the correction, while ε_2 is the efficiency after the correction, and $\Delta\varepsilon/\varepsilon_2$ is the difference between the corrected and not corrected events, a half of the $\Delta\varepsilon/\varepsilon_2$ is taken as the uncertainty of the kinematic fitting.

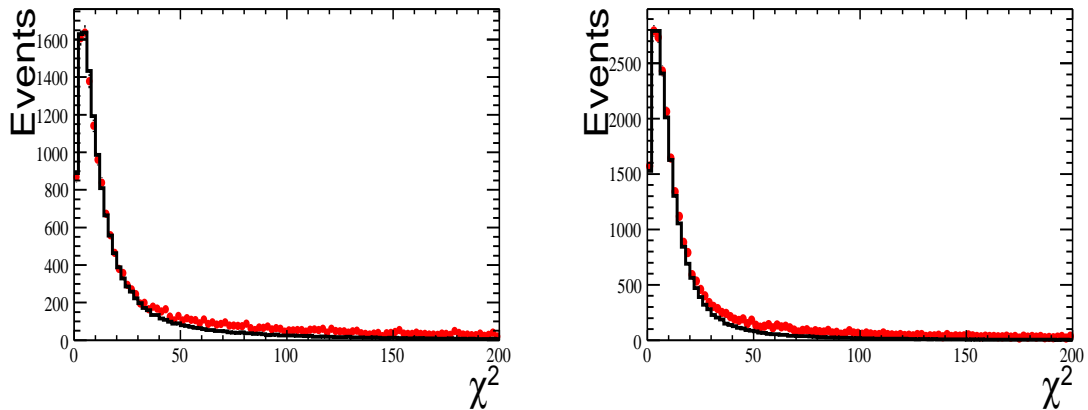


Figure 4.27 A comparison of χ^2 between MC and data for $\psi(2S) \rightarrow \eta J/\psi$. The red error dots are data, the black histogram is MC. Left: $J/\psi \rightarrow e^+ e^-$; Right: $J/\psi \rightarrow \mu^+ \mu^-$

Table 4.7 The detector efficiency of different decay channels

Decay channels	$\varepsilon_1(\%)$	$\varepsilon_2(\%)$	$\frac{1}{2}\Delta\varepsilon/\varepsilon_2(\%)$
$\psi(2S) \rightarrow \pi^0 J/\psi(e^+e^-)$	23.12	23.05	0.15
$\psi(2S) \rightarrow \pi^0 J/\psi(\mu^+\mu^-)$	29.22	29.11	0.19
$\psi(2S) \rightarrow \eta J/\psi(e^+e^-)$	35.55	35.41	0.20
$\psi(2S) \rightarrow \eta J/\psi(\mu^+\mu^-)$	46.54	46.28	0.28

4.3.4 E/p ratios

In the analysis, we use the E/p ratio to identify charged tracks as leptons. If there exists a difference of E/p between MC and data, the E/p cut may be a source of the systematic error.

The uncertainty from the E/p ratio cut is determined with the control sample of $\psi(2S) \rightarrow \pi^+\pi^- J/\psi(l^+l^-)$. All the selection criteria are the same as described in Appendix A.1.3 except for the requirement of the E/p ratio.

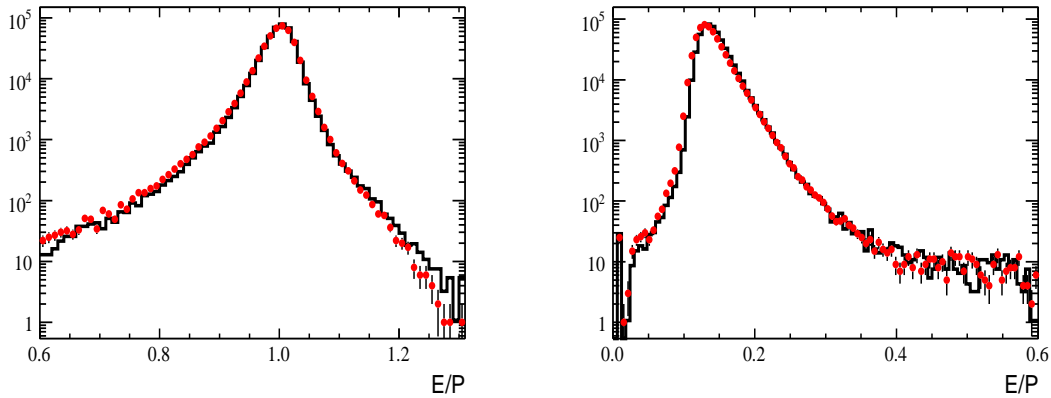


Figure 4.28 Comparison between data and MC simulation events of the distribution E/p ratio in the wider mass range. The red dot with error bar is the data and the black histogram is MC. Left: $J/\psi \rightarrow e^+e^-$. Right: $J/\psi \rightarrow \mu^+\mu^-$

After the selection, two samples with a high purity are obtained. The systematic error caused by E/p cut are 0.06 and 0.05, for $J/\psi \rightarrow e^+e^-$ and $J/\psi \rightarrow \mu^+\mu^-$, respectively. The details are summarized in the table 4.8.

Table 4.8 Summary of the systematical error of E/p ratio

Decay channels	event(data/MC)	with E/p cut	$\Delta\epsilon(\%)$
$\psi(2S) \rightarrow \pi^+\pi^- J/\psi(e^+e^-)$	437123/404967	435750/403953	0.06
$\psi(2S) \rightarrow \pi^+\pi^- J/\psi(\mu^+\mu^-)$	569896/529532	559577/520194	0.05

4.3.5 Mass window cut on the invariant mass of the two leptons

The systematic error caused by the J/ψ mass window cut has been studied with the same control sample as selected for studies of the E/p ratio. The control sample is selected by applying all selection criteria except for the J/ψ mass window. After the event selection, the background levels for this two decay channels are very low, both of them less than 0.05% and 0.20%, respectively. When the mass cut is applied to this sample, the difference between MC and the data is 0.06%, and 0.06%, respectively. The details are summarized in the table 4.9.

Table 4.9 Summary of the systematical error of mass cut

Decay channels	event(data/MC)	with E/p cut	$\Delta\epsilon(\%)$
$\psi(2S) \rightarrow \pi^+\pi^- J/\psi(e^+e^-)$	436273/404262	435818/404096	0.06
$\psi(2S) \rightarrow \pi^+\pi^- J/\psi(\mu^+\mu^-)$	562708/522439	561885/521995	0.06

4.3.6 Mass window cut on the invariant mass of $M_{\gamma l^+ l^-}$

The uncertainty due to the mass window set on the invariant mass $M_{\gamma l^+ l^-}$ is estimated by increasing the widths of the $\chi_{c1/c2}$ to match the data. The control sample $\psi(2S) \rightarrow \gamma\chi_{c1,2}(\gamma J/\psi)$ is used to determine the value of the width of $\chi_{c1,2}$. As the final states of the control sample is same as $\psi(2S) \rightarrow \pi^0(\eta)J/\psi$, the same selection criteria are applied to the data sample. In order to obtain the residual values of $\chi_{c1,2}$ widths in data, we use a Gaussian function to convolute with the $\chi_{c1/c2}$ line shape obtained from MC simulation. The intrinsic widths of the $\chi_{c1/c2}$ in the MC simulation are set to the PDG values. The background shape is described by a 2^{nd} -order polynomial function. The left and the right plots in Fig. 4.29 shows the fit results for $\psi(2S) \rightarrow \gamma\chi_{c1,2}(\gamma J/\psi)$. For the e^+e^- channel, the difference in resolution between MC and data are 2.53 MeV and 1.89 MeV for χ_{c1}

and χ_{c2} , respectively. For the $\mu^+\mu^-$ channel, the difference in resolution between MC and data are 2.61 MeV and 1.27 MeV for χ_{c1} and χ_{c2} , respectively.

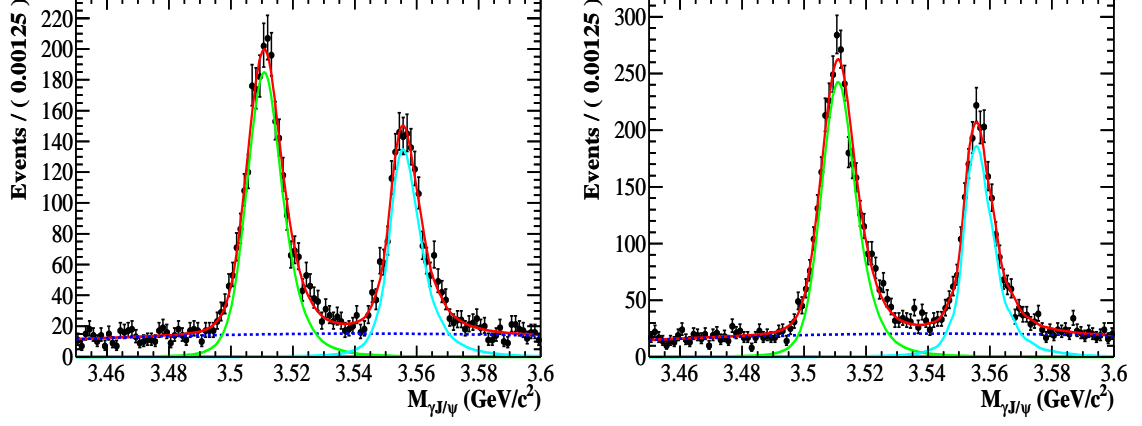


Figure 4.29 The fit results of the mass of $\gamma J/\psi$ in $\psi(2S) \rightarrow \gamma\chi_{c1,2}(\gamma J/\psi)$. Left: $J/\psi \rightarrow e^+e^-$; Right: $J/\psi \rightarrow \mu^+\mu^-$

And then, these values will be used to increase the widths of χ_{c1} and χ_{c2} . Note that, to transform the Gaussian resolution to the Breit-Wigner width, one needs to multiply it by a factor of 1.17 because of the width of Breit-Wigner defined as a half height width of the line shape. We use the new cuts as listed the following:

- $M_{\gamma e^+e^-} < 3.50 - 0.00253 \times 1.17$ or $M_{\gamma e^+e^-} > 3.57 + 0.00189 \times 1.17$.
- $M_{\gamma \mu^+\mu^-} < 3.50 - 0.00261 \times 1.17$ or $M_{\gamma \mu^+\mu^-} > 3.57 + 0.00127 \times 1.17$.

Then we perform the same procedure as described before to fit the mass of $\gamma\gamma$ distribution to obtain the number of π^0 and η . The fit results are listed in table 4.10. The differences in the π^0 and η signal yields are less than 1%; they are taken as systematic errors.

4.3.7 The background shape

In our analysis, an unbinned fitting is applied to the mass spectrum of the two photons. The uncertainty due to the signal line shape is negligible, because the modified MC-shape is used to remove the difference of line shape between the MC and data. The uncertainty due to the shape of unknown background is estimated by replacing it with

Table 4.10 Summary of the fitting result for changing the mass window of $\gamma J/\psi$

Decay channel	N_{fit}	$\varepsilon(\%)$	$Br(10^{-3})$	$ 1 - \frac{Br}{Br_{mean}} (\%)$
$\pi^0 J/\psi(e^+e^-)$	1767 ± 47	22.46	1.264	0.551
$\pi^0 J/\psi(\mu^+\mu^-)$	2213 ± 52	28.45	1.252	0.159
$\eta J/\psi(e^+e^-)$	29466 ± 199	35.29	33.734	0.109
$\eta J/\psi(\mu^+\mu^-)$	38678 ± 236	46.03	34.006	0.818

a higher order polynomial. We change the unknown background function to a 2nd-order polynomial function for $\psi(2S) \rightarrow \pi^0 J/\psi(e^+e^- \text{ or } \mu^+\mu^-)$, and to a 3rd-order polynomial function for $\psi(2S) \rightarrow \eta J/\psi(e^+e^- \text{ or } \mu^+\mu^-)$. The systematical errors are determined to be 0.16%(0.22%) and 1.10%(0.10%) for $\psi(2S) \rightarrow \pi^0 J/\psi(e^+e^- \text{ or } \mu^+\mu^-)$ and $\psi(2S) \rightarrow \eta J/\psi(e^+e^- \text{ or } \mu^+\mu^-)$, respectively. For the $\psi(2S) \rightarrow \eta J/\psi(e^+e^-)$, the goodness of fit becomes worse ($\chi^2/ndf = 1.66$). Figures 4.30 and 4.31 show the fitting results after changing the fitting function for $\psi(2S) \rightarrow \pi^0 J/\psi$ and $\psi(2S) \rightarrow \eta J/\psi$, respectively.

In addition, in order to estimate the uncertainty from the fitting range, we change the fitting range from (0.08, 0.18) to (0.10, 0.16) and from (0.45, 0.60) to (0.48, 0.60) for $\psi(2S) \rightarrow \pi^0 J/\psi$ and $\psi(2S) \rightarrow \eta J/\psi$, respectively.

The fitting values are listed in the table 4.11.

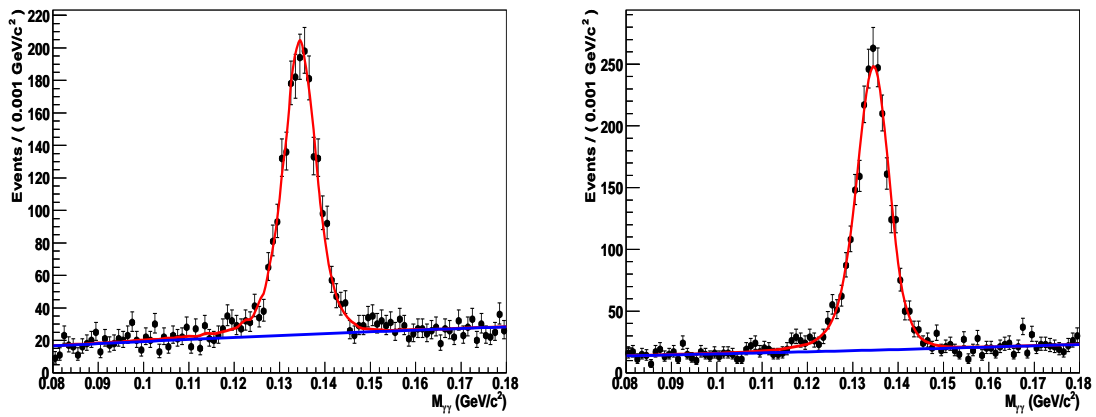


Figure 4.30 The fitting result of the mass of the two photons. Left: $J/\psi \rightarrow e^+e^-$. Right: $J/\psi \rightarrow \mu^+\mu^-$

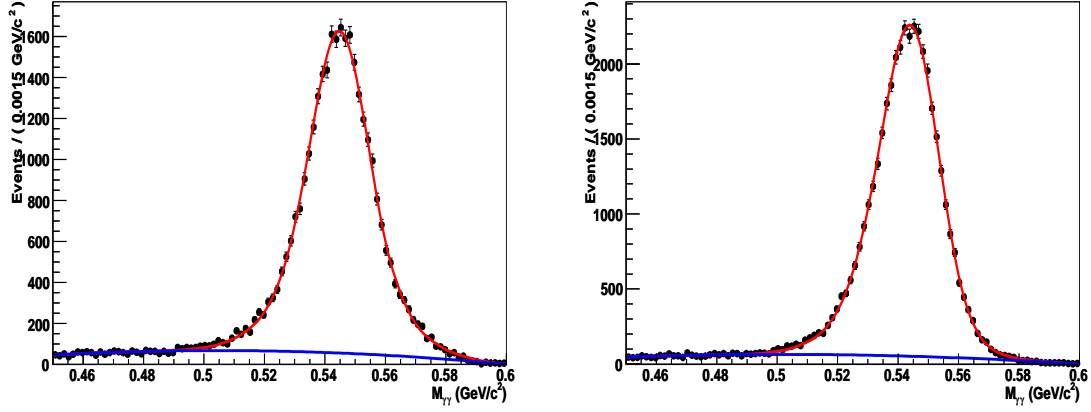


Figure 4.31 The fitting result of the mass of the two photons. Left: $J/\psi \rightarrow e^+e^-$. Right: $J/\psi \rightarrow \mu^+\mu^-$

Table 4.11 Summary of the fitting results for changing background shape and fitting range

Model	Source	$\epsilon(\%)$	N	Br(10^{-03})	$ 1 - \frac{Br}{Br_{mean}} (\%)$
$\psi(2S) \rightarrow \pi^0 J/\psi(e^+e^-)$	Background shape	23.05	1828 ± 52	1.274 ± 0.036	0.236
	Fit range	22.92	1802 ± 45	1.263 ± 0.031	0.629
$\psi(2S) \rightarrow \pi^0 J/\psi(\mu^+\mu^-)$	Background shape	29.11	2273 ± 55	1.257 ± 0.030	0.239
	Fit range	29.01	2278 ± 55	1.264 ± 0.030	0.797
$\psi(2S) \rightarrow \eta J/\psi(e^+e^-)$	Background shape	35.41	29936 ± 206	34.156 ± 0.235	1.14
	Fit range	35.40	29751 ± 213	33.955 ± 0.243	0.545
$\psi(2S) \rightarrow \eta J/\psi(\mu^+\mu^-)$	Background shape	46.28	38612 ± 217	33.765 ± 0.189	0.104
	Fit range	46.24	38760 ± 294	33.924 ± 0.257	0.575

4.3.8 Summary of systematic errors

According to the above analysis, table 4.12 summarizes the systematic errors in the analysis.

Table 4.12 Summary of systematic errors(%)

Sources	$\pi^0(\gamma\gamma)J/\psi(e^+e^-)$	$\pi^0(\gamma\gamma)J/\psi(\mu^+\mu^-)$	$\eta(\gamma\gamma)J/\psi(e^+e^-)$	$\eta(\gamma\gamma)J/\psi(\mu^+\mu^-)$
$N_{\psi(2S)}$	0.81	0.81	0.81	0.81
Trigger	0.15	0.15	0.15	0.15
Tracking	0.14	0.20	0.16	0.19
Photon	2.00	2.00	2.00	2.00
4-C Fit	0.15	0.19	0.20	0.28
$B_r(J/\psi \rightarrow l^+l^-)$	1.01	1.01	1.01	1.01
$B_r(\pi^0/\eta \rightarrow \gamma\gamma)$	0.03	0.03	0.51	0.51
M(l^+l^-) cut	0.06	0.06	0.06	0.06
M(γl^+l^-)	0.55	0.16	0.11	0.82
E/p	0.06	0.05	0.06	0.05
Backgrounds shape	0.24	0.24	1.14	0.10
Fitting range	0.63	0.80	0.55	0.58
Total	2.55	2.55	2.77	2.66

4.4 Summary and discussion

The decays of $\psi(2S) \rightarrow \pi^0 J/\psi$ and $\eta J/\psi$ are measured using the 106 M $\psi(2S)$ decays collected at BEPCII/BESIII in 2009. The measured branching fractions are summarized in table 4.13. The precision of branching fractions of this measurement is highly improved comparing to PDG values.

For the branching fractions of $\psi(2S) \rightarrow \pi^0/\eta J/\psi$, we combine the measurements in the decays $J/\psi \rightarrow e^+e^-$ and $J/\psi \rightarrow \mu^+\mu^-$ with the method of weighted average as used in the PDG table. If the branching fraction is expressed by:

$$Br^i = X^i + \delta_{sta}^i + \delta_{sys-com}^i + \delta_{sys-unc}^i, \quad (4-3)$$

$$= X^i + \delta_{uncor}^i + \delta_{sys-com}^i, \quad (4-4)$$

where $i = 1, 2$ correspond to the channel $J/\psi \rightarrow e^+e^-$ and $J/\psi \rightarrow \mu^+\mu^-$, respectively. δ_{sta}^i , $\delta_{sys-com}^i$ and $\delta_{sys-unc}^i$ are the statistical error, the common systematic error and the

uncommon systematic error, respectively. The total uncorrelated error δ_{uncor}^i is given by

$$\delta_{uncor}^i = \sqrt{(\delta_{sta}^i)^2 + (\delta_{sys-unc}^i)^2},$$

Then the average value and errors are evaluated with

$$\bar{X} = \frac{\sum w_i x_i}{\sum w_i}, \text{ with } w_i = 1/(\delta_{uncor}^i)^2 \quad (4-5)$$

$$\bar{\delta}_{sta} = \left[\sum 1/(\delta_{sta}^i)^2 \right]^{-1/2}, \quad (4-6)$$

$$\bar{\delta}_{sys-un} = \left[\sum 1/(\delta_{sys-un}^i)^2 \right]^{-1/2}. \quad (4-7)$$

$$(4-8)$$

Where the sum runs over $i = 1, 2$.

Combined the common and uncommon systematic errors, one has:

$$\bar{\delta}_{sys} = \bar{X} \left[\left(\frac{\bar{\delta}_{sys-un}}{\bar{X}} \right)^2 + \left(\frac{\delta_{sys-com}^i}{X^i} \right)^2 \right]^{1/2}.$$

Where $\delta_{sys-com}^i/X^i$ is the common part, which is accounted once. It's value is the same for $i = 1$ or 2 .

The averaged branching fraction is given by

$$\bar{B}r = \bar{X} + \bar{\delta}_{sta} + \bar{\delta}_{sys}.$$

The common systematic uncertainties include two photon reconstruction, $\psi(2S)$ number and the branching fractions for $\pi^0/\eta \rightarrow \gamma\gamma$ and $M(l^+l^-)$ cuts. The averaged branching fraction for $\psi(2S) \rightarrow \pi^0/\eta J/\psi$ are given in the table 4.13.

Table 4.13 Summary of measurement results

Mode	$\psi(2S) \rightarrow \pi^0 J/\psi$		$\psi(2S) \rightarrow \eta J/\psi$		
Final states	$\gamma\gamma e^+ e^-$	$\gamma\gamma\mu^+\mu^-$	$\gamma\gamma e^+ e^-$	$\gamma\gamma\mu^+\mu^-$	
$N_{tot}(\times 10^6)$	106	106	106	106	
N_{sig}	1823 \pm 49	2268 \pm 55	29598 \pm 202	38572 \pm 280	
$\varepsilon(\%)$	23.05 \pm 0.05	29.11 \pm 0.06	35.41 \pm 0.06	46.28 \pm 0.06	
Br($\times 10^{-3}$)	This work	1.27 \pm 0.03 \pm 0.03	1.25 \pm 0.03 \pm 0.03	33.77 \pm 0.23 \pm 0.93	33.73 \pm 0.24 \pm 0.90
	BESII	1.39 \pm 0.20 \pm 0.12	1.47 \pm 0.19 \pm 0.13	29.10 \pm 1.20 \pm 2.10	30.60 \pm 1.40 \pm 2.50
	CLEOc	1.33 \pm 0.08 \pm 0.03		34.30 \pm 0.40 \pm 0.89	
	PDG2010	1.30 \pm 0.10		32.80 \pm 0.70	
	This work	1.26 \pm 0.02 \pm 0.03		33.75 \pm 0.17 \pm 0.86	

Chapter 5 Conclusions

Based on the data sample accumulated at BEPCII/BESIII in 2009, including 225 million of J/ψ data sample and 106 million of $\psi(2S)$ data sample, $J/\psi \rightarrow \gamma\eta_c$, $\eta_c \rightarrow \phi\phi(\omega\phi)$ and $\psi(2S) \rightarrow \pi^0(\eta)J/\psi$ have been studied in this thesis and the improve measurements on the branching fractions of the channels have been presented.

5.1 Summary

5.1.1 $J/\psi \rightarrow \gamma\eta_c$, $\eta_c \rightarrow \phi\phi(\omega\phi)$

Table 5.1 shows the comparison of our results with different experiments. The branching fraction of $\eta_c \rightarrow \phi\phi$ of our measurement is consistent with previous measurements performed by BESI, BESII and DM2 collaborations, and the precision is improved with a factor of about 1.7, and the dominated error is from the uncertainty of branching fraction for $J/\psi \rightarrow \gamma\eta_c$. For the $J/\psi \rightarrow \gamma\eta_c$, $\eta_c \rightarrow \phi\phi$, the precision of branching fraction is improved with a factor of 1.6.

Table 5.1 Comparison of $Br(\eta_c \rightarrow \phi\phi)$ to other measurements

$Br(J/\psi \rightarrow \gamma\eta_c, \eta_c \rightarrow \phi\phi)(10^{-5})$	$Br(\eta_c \rightarrow \phi\phi) (10^{-3})$	Comment
$3.55^{+0.16}_{-0.20} \pm 0.51$	$2.09^{+0.10}_{-0.12} \pm 0.58$	this measurement
$3.25 \pm 0.65 \pm 0.65$	$2.53 \pm 0.51 \pm 0.91$	BESII ^[60]
$3.3 \pm 0.6 \pm 0.6$	2.6 ± 0.9	BESII ^[61]
$3.9 \pm 0.9 \pm 0.9$	$3.1 \pm 0.7 \pm 0.4$	DM2 ^[59]
—	1.94 ± 0.30	PDG2012 ^[10]

The OZI double suppressed decay $\eta_c \rightarrow \omega\phi$ is not observed, and the upper limit is set as $Br(\eta_c \rightarrow \omega\phi) < 3.14 \times 10^{-4}$ at 90% confidence level. This upper limit is lower than the PDG2012 value 1.7×10^{-3} ^[10] by one order of magnitude.

According to hadronic helicity conservation^[33], there are many decays of charmonium are forbidden^[34], but some of these decays have been observed^[10], such as $J/\psi \rightarrow K^*\bar{K}^*$, $J/\psi \rightarrow \rho\pi$, $\eta_c \rightarrow \phi\phi$, $\eta_c \rightarrow \rho\rho$ and so on. Our result will make the theorist to re-build a reliable model to describe this phenomenon.

5.1.2 Hadronic transitions from $\psi(2S)$ to J/ψ

Using the measured branching fractions,

- $\mathcal{B}(\psi(2S) \rightarrow \pi^0 J/\psi) = (1.26 \pm 0.02 \pm 0.03) \times 10^{-3}$
- $\mathcal{B}(\psi(2S) \rightarrow \eta J/\psi) = (33.75 \pm 0.17 \pm 0.86) \times 10^{-3}$,

the ratio $R = \mathcal{B}(\psi(2S) \rightarrow \pi^0 J/\psi) / \mathcal{B}(\psi(2S) \rightarrow \eta J/\psi)$ is determined to be $R = (3.74 \pm 0.06 \pm 0.04) \times 10^{-2}$. As the result shown in table 5.2, our result on the R -ratio is consistent with previous world average values with a precision improvement of about a factor of 5. These precise measurements of the $\psi(2S) \rightarrow \pi^0 J/\psi$ and $\eta J/\psi$ branching fractions permit the study of isospin violation mechanisms in the $\psi(2S) \rightarrow \pi^0 J/\psi$ transition.

Table 5.2 Summary for the ratio $R = \frac{Br_{\psi(2S) \rightarrow \pi^0 J/\psi}}{Br_{\psi(2S) \rightarrow \eta J/\psi}}$

Final state	Ratio(%)	
	$\gamma\gamma e^+ e^-$	$\gamma\gamma\mu^+\mu^-$
Theory	3.1±1.6	
This work	3.76±0.09±0.06	3.71±0.09±0.05
Combined	3.74±0.06±0.04	
PDG2010	3.96±0.42	
CLEO-c	3.88±0.23±0.05	

These precise measurements of the $\psi(2S) \rightarrow \pi^0 J/\psi$ and $\eta J/\psi$ branching fractions permit the study of isospin violation mechanisms in the $\psi(2S) \rightarrow \pi^0 J/\psi$ transition. As shown in literature^[68], the axial anomaly does not adequately explain the observed isospin violation, while contributions from charmed meson loops would be a possible mechanism for additional isospin violation sources. Confirmation of sizeable contributions from charmed-meson loops would be an indication that non-perturbative effects play an important role in the charmonium energy region.

5.2 Outlook

With the good performance of BEPCII/BESIII and more and more high quality data sample, a higher precision measurement on these channels could be obtained for theory study. In order to make a comprehensive understanding of QCD theory, more decay channels of these kinds should be studied. In order to understand HSR, the study of $\eta_c \rightarrow VV$ should

include other channels, such as $\eta_c \rightarrow \omega\omega$, $\eta_c \rightarrow \rho\rho$, $\eta_c \rightarrow K^*\bar{K}^*$, etc.. If one analyzes $\eta_c \rightarrow \omega\omega$, the combinatorial backgrounds should be studied as there are many combination with different π s. As the large width of ρ ($149 \text{ MeV}/c^2$)^[10] and K^* ($46 \text{ MeV}/c^2$)^[10], the backgrounds of these two decay channels are abundant, and the interferences between background and signal are more complicated than $\eta_c \rightarrow \phi\phi$.

Reference

- [1] Zweig G. AN SU(3) MODEL FOR STRONG INTERACTION SYMMETRY AND ITS BREAKING. PT. 2. Developments in the Quark Theory of Hadrons, 1964, 1:22.
- [2] Gell-Mann M. A Schematic Model of Baryons and Mesons. Phys.Lett., 1964, 8:214–215.
- [3] Gross D, Wilczek F. Ultraviolet Behavior of Nonabelian Gauge Theories. Phys.Rev.Lett., 1973, 30:1343–1346.
- [4] Politzer H D. Reliable Perturbative Results for Strong Interactions? Phys.Rev.Lett., 1973, 30:1346–1349.
- [5] Bettini A. Introduction to elementary particle physics. CAMBRIDGE UNIVERSITY.
- [6] Aubert J, et al. Experimental Observation of a Heavy Particle J. Phys.Rev.Lett., 1974, 33:1404–1406.
- [7] Augustin J, et al. Discovery of a Narrow Resonance in $e^+ e^-$ Annihilation. Phys.Rev.Lett., 1974, 33:1406–1408.
- [8] Yoh J. The Discovery of the b Quark at Fermilab in 1977: The Experiment Coordinators Story. <http://lss.fnal.gov/archive/1997/conf/Conf-97-432-E.pdf>.
- [9] Abe F, et al. Observation of Top Quark Production in $p\bar{p}$ Collisions with the Collider Detector at Fermilab. Phys.Rev.Lett., 1995, 74:2626–2631.
- [10] Beringer J, et al. Review of Particle Physics (RPP). Phys.Rev., 2012, D86:010001.
- [11] Bjorken J, Glashow S. Elementary Particles and SU(4). Phys.Lett., 1964, 11:255–257.
- [12] Gell-Mann M, Neeman Y. The Eightfold way: a review with a collection of reprints. 1964..
- [13] Abrams G, Briggs D, Chinowsky W, et al. The Discovery of a Second Narrow Resonance in $e^+ e^-$ Annihilation. Phys.Rev.Lett., 1974, 33:1453–1455.
- [14] Rosner J, et al. Observation of $h(c)(P(1)-1)$ state of charmonium. Phys.Rev.Lett., 2005, 95:102003.
- [15] Choi S, et al. Observation of a narrow charmonium - like state in exclusive $B^\pm \rightarrow K^\pm \pi^+ \pi^- J/\psi$ decays. Phys.Rev.Lett., 2003, 91:262001.
- [16] Abazov V, et al. Observation and properties of the $X(3872)$ decaying to $J/\psi \pi^+ \pi^-$ in $p\bar{p}$ collisions at $\sqrt{s} = 1.96$ TeV. Phys.Rev.Lett., 2004, 93:162002.
- [17] Aubert B, et al. Measurements of the absolute branching fractions of $B^\pm \rightarrow K^\pm X(c\bar{c})$. Phys.Rev.Lett., 2006, 96:052002.
- [18] Abe K, et al. Observation of a near-threshold omega J/ψ mass enhancement in exclusive $B \rightarrow K$ omega J/ψ decays. Phys.Rev.Lett., 2005, 94:182002.
- [19] Aubert B, et al. Observation of a broad structure in the $\pi^+ \pi^- J/\psi$ mass spectrum around 4.26-GeV/ c^2 . Phys.Rev.Lett., 2005, 95:142001.
- [20] Okubo S. Phi meson and unitary symmetry model. Phys.Lett., 1963, 5:165–168.
- [21] Barnes T, et al. CHARMONIUM PHYSICS. CCAST-WL WORKSHOP, 2003.

Reference

- [22] Caswell W, Lepage G. Effective Lagrangians for Bound State Problems in QED, QCD, and Other Field Theories. *Phys.Lett.*, 1986, B167:437.
- [23] Lepage G P, Magnea L, Nakhleh C, et al. Improved nonrelativistic QCD for heavy quark physics. *Phys.Rev.*, 1992, D46:4052–4067.
- [24] Bodwin G T, Braaten E, Lepage G P. Rigorous QCD analysis of inclusive annihilation and production of heavy quarkonium. *Phys.Rev.*, 1995, D51:1125–1171.
- [25] Braaten E, Fleming S. Color octet fragmentation and the psi-prime surplus at the Tevatron. *Phys.Rev.Lett.*, 1995, 74:3327–3330.
- [26] Cacciari M, Greco M, Mangano M L, et al. Charmonium production at the Tevatron. *Phys.Lett.*, 1995, B356:553–560.
- [27] Braaten E, Chen Y Q. Signature for color octet production of J/ψ in e^+e^- annihilation. *Phys.Rev.Lett.*, 1996, 76:730–733.
- [28] Qiao C F, Chao K T. Introduction to Charm Physics. CCAST-WL WORKSHOP, 2007.
- [29] Adloff C, et al. Search for QCD instanton induced processes in deep inelastic scattering at HERA. *Eur.Phys.J.*, 2002, C25:495–509.
- [30] Abulencia A, et al. Polarization of J/ψ and $\psi(2S)$ mesons produced in $p\bar{p}$ collisions at $\sqrt{s} = 1.96$ -TeV. *Phys.Rev.Lett.*, 2007, 99:132001.
- [31] Kopke L, Wormes N. J/ψ Decays. *Phys.Rept.*, 1989, 174:67.
- [32] Kwong W, Rosner J L, Quigg C. Heavy Quark Systems. *Ann.Rev.Nucl.Part.Sci.*, 1987, 37:325–382.
- [33] Brodsky S J, Lepage G P. Helicity Selection Rules and Tests of Gluon Spin in Exclusive QCD Processes. *Phys.Rev.*, 1981, D24:2848.
- [34] Chernyak V, Zhitnitsky A. Exclusive Decays of Heavy Mesons. *Nucl.Phys.*, 1982, B201:492.
- [35] Chernyak V, Zhitnitsky A. Asymptotic Behavior of Exclusive Processes in QCD. *Phys.Rept.*, 1984, 112:173.
- [36] Anselmino M, Murgia F. $\chi_{c0,c2} \rightarrow \rho\rho$ decays and the rho polarization: Massless versus constituent quarks. *Phys.Rev.*, 1993, D47:3977–3983.
- [37] Bolz J, Kroll P, Schuler G A. Color octet contributions to exclusive charmonium decays. *Phys.Lett.*, 1997, B392:198–206.
- [38] Appelquist T, Politzer H D. Orthocharmonium and e^+e^- Annihilation. *Phys.Rev.Lett.*, 1975, 34:43.
- [39] Lipkin H, Rubinstein H, Isgur N. WHERE IS THE η_c ? *Phys.Lett.*, 1978, B78:295.
- [40] Schnitzer H J. Hyperfine Splitting of Ground State Charmonium. *Phys.Rev.*, 1976, D13:74.
- [41] Barbieri R, Kogerler R, Kunszt Z, et al. Meson Masses and Widths in a Gauge Theory with Linear Binding Potential. *Nucl.Phys.*, 1976, B105:125.
- [42] Novikov V, Okun L, Shifman M A, et al. Sum Rules for the Decays of the C Even Charmonium States. *Phys.Lett.*, 1977, B67:409.
- [43] Shifman M A, Vainshtein A, Zakharov V I. QCD and Resonance Physics: Applications. *Nucl.Phys.*, 1979, B147:448–518.

Reference

- [44] Braunschweig W, et al. Radiative Decays of the J/ψ and Evidence for a New Heavy Resonance. *Phys.Lett.*, 1977, B67:243.
- [45] Partridge R, Peck C, Porter F, et al. THE DECAY $J/\psi \rightarrow 3\gamma$ AND A SEARCH FOR THE $\eta(c)$. *Phys.Rev.Lett.*, 1980, 44:712.
- [46] Partridge R, Peck C, Porter F, et al. Observation of an $\eta(c)$ Candidate State with Mass 2978-MeV \pm 9-MeV. *Phys.Rev.Lett.*, 1980, 45:1150–1153.
- [47] Himel T, Trilling G, Abrams G, et al. OBSERVATION OF THE $\eta(c)$ (2980) PRODUCED IN THE RADIATIVE DECAY OF THE ψ -prime (3684). *Phys.Rev.Lett.*, 1980, 45:1146.
- [48] Baltrusaitis R, et al. HADRONIC DECAYS OF THE $\eta(c)$ (2980). *Phys.Rev.*, 1986, D33:629.
- [49] Baglin C, et al. MEASUREMENT OF THE $\phi\phi$ CROSS-SECTION IN p anti- p ANNIHILATIONS AT E(cm) approximately 3-GeV. *Phys.Lett.*, 1989, B231:557.
- [50] Bisello D, et al. Study of the $\eta(c)$ decays. *Nucl.Phys.*, 1991, B350:1–24.
- [51] Albrecht H, et al. Determination of the radiative decay width of the $\eta(c)$ meson. *Phys.Lett.*, 1994, B338:390–396.
- [52] Quigg C, Rosner J L. Hadronic Decays of $\eta(c)$. *Phys.Rev.*, 1977, D16:1497.
- [53] Jia Y, Zhao G D. HADRONIC DECAYS OF THE $\eta(c)$ (2980). *High Energy Phys. Nucl. Phys.*, 23:765.
- [54] Sun P, Hao G, Qiao C F. Pseudoscalar Quarkonium Exclusive Decays to Vector Meson Pair. *Phys.Lett.*, 2011, B702:49–54.
- [55] Wang Q, Liu X H, Zhao Q. Study of η_c and η'_c decays into vector meson pairs. *arXiv*, 2010, 1010.1343.
- [56] Zhou H, Ping R, Zou B. $(3)P(0)$ quark-creation mechanism for $\eta(c)$ decay to vector meson pairs. *Phys.Rev.*, 2005, D71:114002.
- [57] Chang N P, Nelson C. YANG'S PARITY TEST APPLIED TO THE X (2.85). *Phys.Rev.Lett.*, 1978, 40:1617.
- [58] Trueman T. $\phi\phi$ DECAY AS A PARITY AND SIGNATURE TEST. *Phys.Rev.*, 1978, D18:3423.
- [59] Bisello D, et al. A MEASUREMENT OF $\eta_c \rightarrow \phi\phi$ IN THE RADIATIVE DECAY OF THE J/ψ . *Phys.Lett.*, 1986, B179:289–293.
- [60] Ablikim M, et al. Experimental study of $\eta(c)$ decays into vector-vector final states. *Phys.Rev.*, 2005, D72:072005.
- [61] Bai J, et al. Measurement of branching ratios for $\eta(c)$ hadronic decays. *Phys.Lett.*, 2004, B578:16–22.
- [62] Ablikim M, Achasov M, An L, et al. Observation of χ_{c1} decays into vector meson pairs $\phi\phi$, $\omega\omega$, and $\omega\phi$. *Phys.Rev.Lett.*, 2011, 107:092001.
- [63] Bai J, et al. $\psi(2S)$ decays into J/ψ plus two photons. *Phys.Rev.*, 2004, D70:012006.
- [64] Mendez H, et al. Branching Fractions for Transitions of $\psi(2S)$ to J/ψ . *Phys.Rev.*, 2008, D78:011102.

Reference

- [65] Kuang Y P, Yan T M. Predictions for Hadronic Transitions in the B anti-B System. *Phys.Rev.*, 1981, D24:2874.
- [66] Ioffe B, Shifman M A. DECAYS $\psi(2S) \rightarrow J/\psi\pi^0(\eta)$ AND QUARK MASSES. *Phys.Lett.*, 1980, B95:99.
- [67] Miller G, Nefkens B, Slaus I. Charge symmetry, quarks and mesons. *Phys.Rept.*, 1990, 194:1–116.
- [68] Guo F K, Hanhart C, Meissner U G. On the extraction of the light quark mass ratio from the decays $\psi(2S) \rightarrow J/\psi\pi^0(\eta)$. *Phys.Rev.Lett.*, 2009, 103:082003.
- [69] Guo F K, Hanhart C, Li G, et al. Effect of charmed meson loops on charmonium transitions. *Phys.Rev.*, 2011, D83:034013.
- [70] Guo Z k, Narison S, Richard J M, et al. Isospin violating decay of $\psi(3770) \rightarrow J/\psi + \pi^0$. *Phys.Rev.*, 2012, D85:114007.
- [71] Zhang Y J, Li G, Zhao Q. Towards a dynamical understanding of the non-D anti-D decay of $\psi(3770)$. *Phys.Rev.Lett.*, 2009, 102:172001.
- [72] Li G, Zhao Q. Revisit the radiative decays of J/ψ and $\psi' \rightarrow \gamma\eta_c(\gamma\eta'_c)$. *Phys.Rev.*, 2011, D84:074005.
- [73] BETTINI A. INTRODUCTION TO ELEMENTARY PARTICLE PHYSICS. Cambridge university, 2008.
- [74] Zhang C. AN OVERVIEW OF THE BEPCII PROJECT. Proceedings of 40th ICFA ABDW, 2008.
- [75] Ablikim M, et al. Design and Construction of the BESIII Detector. 2009.
- [76] Ning T. A prototype of the read-out subsystem of the BESIII DAQ based on PowerPC, Plasma Science and Technology. 2005.
- [77] Group A T. Group Meeting. <https://twiki.cern.ch/twiki/bin/view/Atlas/TriggerDAQ>.
- [78] Asner D M, et al. Physics at BESIII. IHEP-Physics-Report-BESIII, 2008.
- [79] Jadach S, Ward B, Was Z. The Precision Monte Carlo event generator K K for two fermion final states in $e^+ e^-$ collisions. *Comput.Phys.Commun.*, 2000, 130:260–325.
- [80] Jadach S, Ward B, Was Z. Coherent exclusive exponentiation for precision Monte Carlo calculations. *Phys.Rev.*, 2001, D63:113009.
- [81] Ping R G. Event generators at BESIII. *Chin.Phys.*, 2008, C32:599.
- [82] Jadach S, Placzek W, Richter-Was E, et al. Upgrade of the Monte Carlo program BHLUMI for Bhabha scattering at low angles to version 4.04. *Comput.Phys.Commun.*, 1997, 102:229–251.
- [83] Jadach S, Placzek W, Ward B. BHWIDE 1.00: O(alpha) YFS exponentiated Monte Carlo for Bhabha scattering at wide angles for LEP-1 / SLC and LEP-2. *Phys.Lett.*, 1997, B390:298–308.
- [84] Balossini G, Carloni Calame C M, Montagna G, et al. Matching perturbative and parton shower corrections to Bhabha process at flavour factories. *Nucl.Phys.*, 2006, B758:227–253.
- [85] Chen J C, Huang G S, Qi X R, et al. Event generator for J/ψ and $\psi(2S)$ decay. *Phys.Rev.*, 2000, D62:034003.

Reference

- [86] Ablikim M, et al. Determination of the number of J/ψ events with $J/\psi \rightarrow$ *inclusive* decays. Chin.Phys., 2012, C36:915–925.
- [87] Nakamura K, et al. Review of particle physics. J.Phys., 2010, G37:075021.
- [88] Baltrusaitis R, et al. OBSERVATION OF THE DECAY $\eta_c \rightarrow \phi\phi$ AND DETERMINATION OF THE η_c SPIN PARITY. Phys.Rev.Lett., 1984, 52:2126–2129.
- [89] Mitchell R, et al. J/ψ and $\psi(2S)$ Radiative Decays to η_c . Phys.Rev.Lett., 2009, 102:011801.
- [90] Ablikim M, et al. Measurements of the mass and width of the η_c using $\psi(2S) \rightarrow \gamma\eta_c$. Phys.Rev.Lett., 2012, 108:222002.
- [91] Ablikim M, et al. Study of χ_{cJ} radiative decays into a vector meson. Phys.Rev., 2011, D83:112005.
- [92] Y C, et al. Kaon's tracking and PID efficiency. BES Collaboration, 2011.
- [93] Ablikim M, Achasov M, Ambrose D. Determination of the number of ψ' event at BESIII. arXiv, 2012, 1209.6199.
- [94] Chung S. A General formulation of covariant helicity coupling amplitudes. Phys.Rev., 1998, D57:431–442.
- [95] Chung S. Helicity coupling amplitudes in tensor formalism. Phys.Rev., 1993, D48:1225–1239.

Acknowledgement

衷心感谢导师高原宁教授对我的悉心指导。高老师无论在生活上还是学习上，都给予我莫大的帮助。高老师积极乐观的生活态度，教会我正确处理好生活与学习的关系。高老师渊博的知识，一次次地帮我克服科研上的困难。

衷心感谢中国科学院高能物理研究所的平荣刚研究员。平老师认真严谨的科学态度和勤奋好学的学习态度，教会了我如何才能成为一名合格的科研人员。平老师渊博的学识让我在进行物理研究时受益匪浅。

衷心感谢家人对我的支持。爸爸妈妈以及弟弟的支持，是我能够顺利完成学业的保障，你们是我心灵的港湾。感谢女友肖湘，你总能在我感到无助的时候出现，给予我最温暖的关怀。

衷心感谢实验室的陈少敏教授，杨振伟副教授，王喆副研究员，朱相雷老师和田俊平，张艳席，刘勃，李波，张峰，李一鸣，吴素芝，袁煦昊，钟亮，景繁凡，夏力钢，张洋，随海建，丁明明，王雄飞，刘凯，魏瀚宇，古拉姆多年来对我的帮助，和你们共同度过的这3年将是我最美好的回忆。

声 明

本人郑重声明：所呈交的学位论文，是本人在导师指导下，独立进行研究工作所取得的成果。尽我所知，除文中已经注明引用的内容外，本学位论文的研究成果不包含任何他人享有著作权的内容。对本论文所涉及的研究工作做出贡献的其他个人和集体，均已在文中以明确方式标明。

签 名：_____ 日 期：_____

Appendix A

A.1 Estimation of the uncertainty of 4C-kinematic fitting

A.1.1 $J/\psi \rightarrow \gamma\eta_c(\phi\phi)$

A.1.1.1 Event selection for $J/\psi \rightarrow \phi K^+ K^-$

General event selections for charged tracks and photons are the same as before and the good charged tracks must be equalling to 4 with net charge equalling to 0. To select a control samples with a high purity, the PID information has been applied, and require the probability of all the charged tracks identified as kaon must be larger than any other particles. Other selection criteria are listed below:

- $\delta(P) = \sqrt{\sum_{i=0}^3 (CMS_i - Ptot_i)^2} < 0.03$. CMS is four momentum of the center of mass energy, $CMS = CMS(0.034, 0, 0, 3.097)$. Ptot is four momentum of all the charged tracks. The index $i(0,1,2)$ means the momentum of different direction(x, y, z).
- $1.00 \text{ GeV}/c^2 < M_{K^+K^-} < 1.04 \text{ GeV}/c^2$;
- χ^2 of 4C kinematic fit must be smaller than 60.

With these strategies, a data sample with a purity of 97.34% would be obtained and the detector efficiency is 29.57%.

A.1.1.2 Comparison between MC and Data

Figures A.1 show the pull distributions obtained after the 4C-kinematic fitting for each tracks. From these figures, the discrepancy between MC and data is obviously. It means that in order to match for the data distribution, it is necessary to make a correction to the parameters of the charged tracks in the MC.

A.1.1.3 Correction factors for MC sample

The pull of the i^{th} track parameter is defined as $pull_i = \frac{\alpha_i - \alpha_{0i}}{\sqrt{|(V_{\alpha 0})_{ii} - (V_{\alpha})_{ii}|}}$, where α_0 is the unconstrained track parameters obtained from the reconstruction, α is the constrained track parameters obtained from kinematic fit and V is the corresponding covariance matrix element. Theoretically, the pull distribution is a standard normal distribution, but

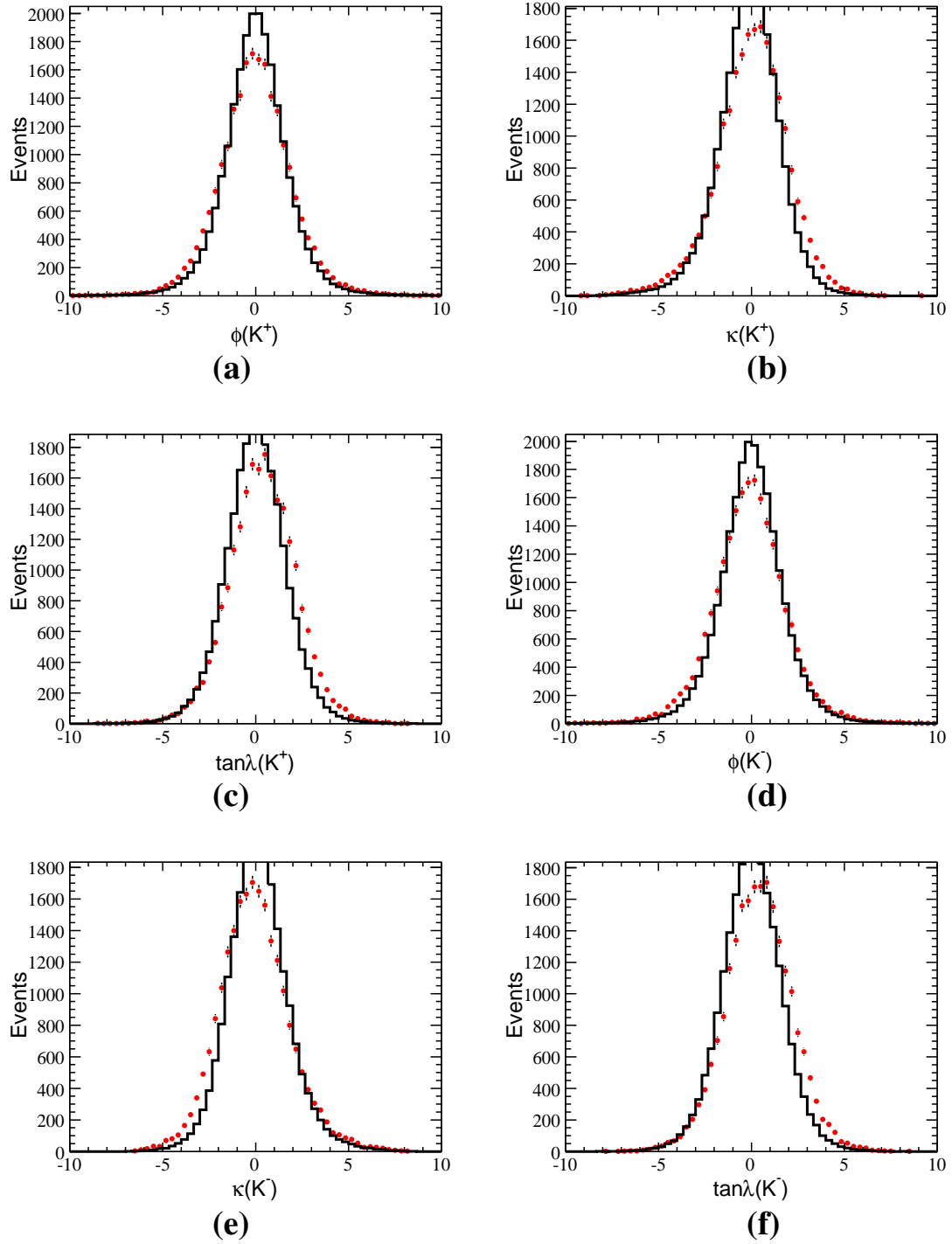


Figure A.1 The comparison of pull distribution between MC and data, the red error bars are data, the black histograms are MC.

actually, it obeys a Normal distribution with mean μ_i and deviation σ_i . There are two methods to reduce the difference between data and MC. One is to reduce $(V_{\alpha 0})_{ii}$ by multiplying it with a factor $\sigma_i^{MC}/\sigma_i^{data}$, the other one is to smear the resolution of α_{0i} by smearing it with a Gaussian distribution, in which the mean and σ values are defined as $\alpha_{0i} + (\mu_i^{data} - \mu_i^{MC}) \times (V_{\alpha 0})_{ii}$ and $\sqrt{((\sigma_i^{data}/\sigma_i^{MC})^2 - 1) \times (V_{\alpha 0})_{ii}}$. Since the data and MC are consistent with each other in the covariance matrix from MdcKalTrk, it is unnecessary to change the covariance matrix, we choose the second method to correct the MC to data. Table A.1 lists the corrected parameters for the lepton. Figures A.2 and Figures A.3 show the pull after the correction and the comparison of χ^2 between MC and data. With the parameters obtained from the pull distribution, the corrected MC is consistent with the data.

Table A.1 Correction factors extracted from the pull distribution

	ϕ_0		κ		$\tan \lambda$	
	$m^{data} - m^{MC}$	$\sigma^{data}/\sigma^{MC}$	$m^{data} - m^{MC}$	$\sigma^{data}/\sigma^{MC}$	$m^{data} - m^{MC}$	$\sigma^{data}/\sigma^{MC}$
K^+	-0.0318	1.1967	0.1280	1.2430	0.1390	1.1165
K^-	-0.0776	1.1628	-0.1369	1.2431	0.1426	1.1180

A.1.2 $J/\psi \rightarrow \gamma\eta_c, \eta_c \rightarrow \omega(\pi^0\pi^+\pi^-)\phi(K^+K^-)$

In the section, $J/\psi \rightarrow \omega(\pi^0\pi^+\pi^-)\eta(\pi^0\pi^+\pi^-)$ would be selected to extract the parameters for pion. The selections for this sample has been introduced before (estimation of uncertainties $M_{\gamma\gamma}$ and $M_{\pi^0\pi^+\pi^-}$). In this part, the selections would not be described.

A.1.2.1 The pull distribution of the track helix

Figures A.4 show the pull distributions between data and MC sample before corrected. And the correction parameters would be obtained from the discrepancy between MC and data. Table A.2 is the summary of the correction parameters. With these parameters, the pull distributions of MC will be corrected to data. Figures A.5 show the pull distribution after correction.

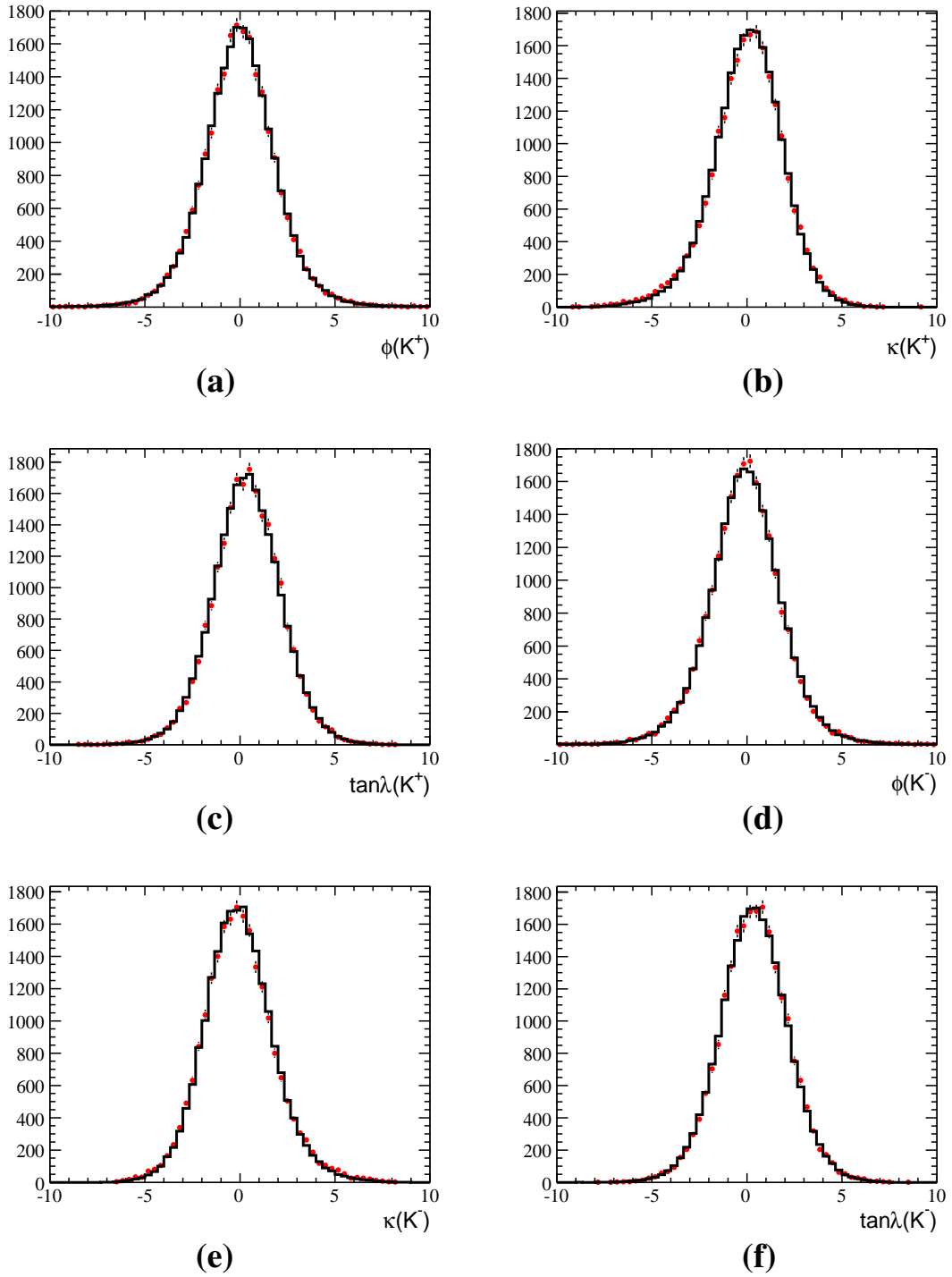


Figure A.2 The comparison of pull distribution between MC and data, the red error bars are data, the black histograms are MC.

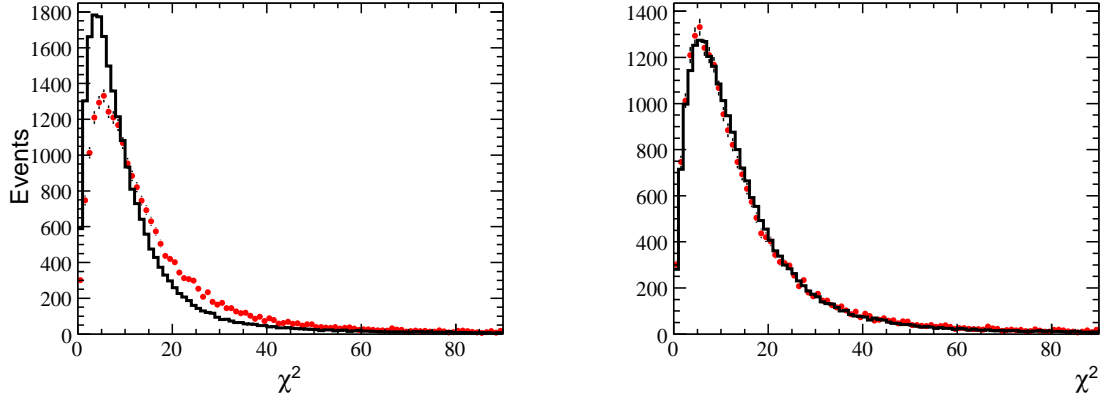


Figure A.3 The comparison of χ^2 between data and MC. The red dots are data, the black histogram is MC. Left: before correction Right: after correction.

Table A.2 Correction factors extracted from the pull distribution

	ϕ_0		κ		$\tan \lambda$	
	$m^{data} - m^{MC}$	$\sigma^{data} / \sigma^{MC}$	$m^{data} - m^{MC}$	$\sigma^{data} / \sigma^{MC}$	$m^{data} - m^{MC}$	$\sigma^{data} / \sigma^{MC}$
π^+	-0.0251	1.1714	-0.0096	1.0626	0.1947	1.0723
π^-	0.0067	0.9079	0.0060	1.0019	0.1272	1.0519

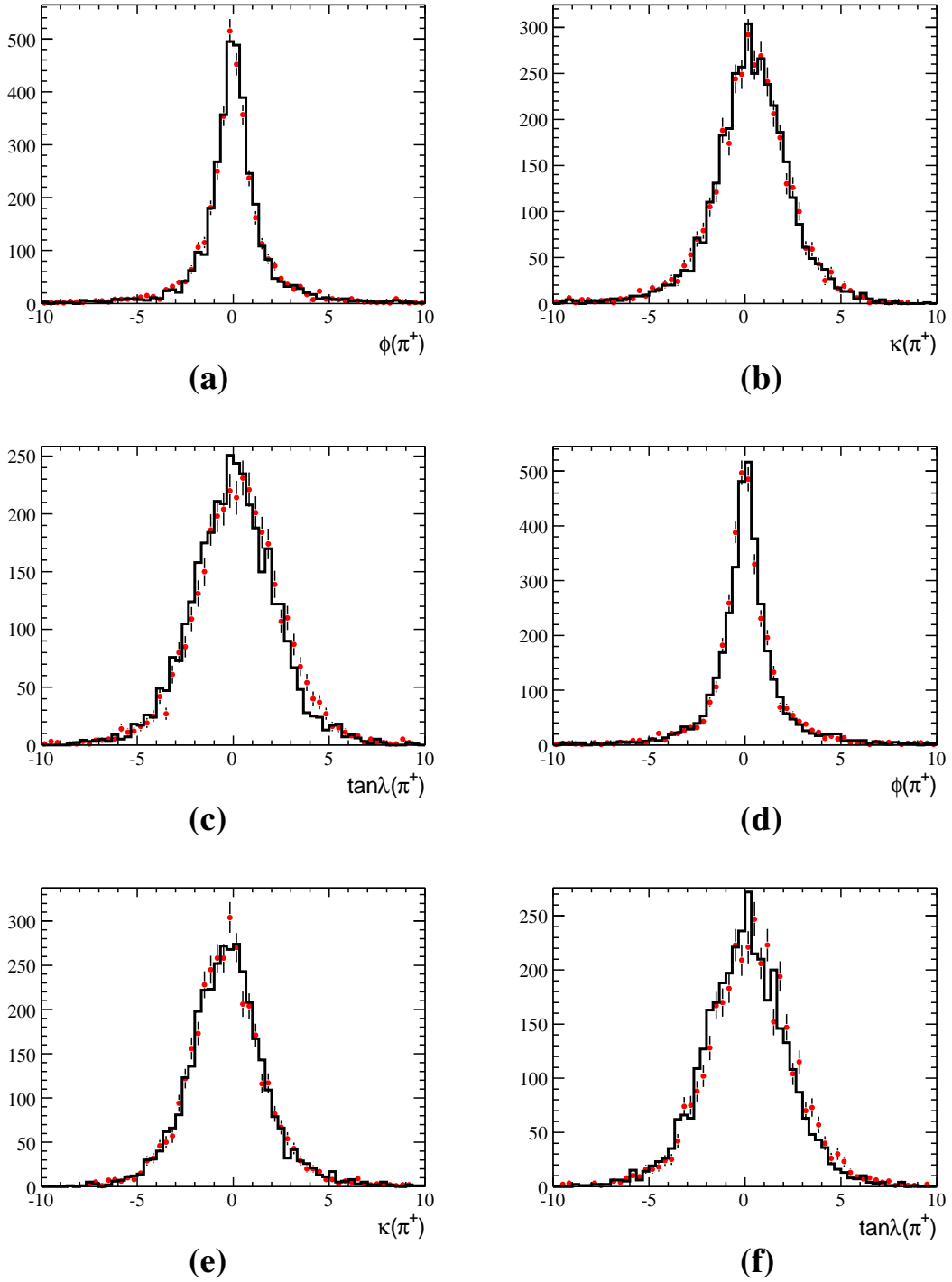


Figure A.4 The comparison of pull distribution between MC and data before correction, the red error bars are data, the black histograms are MC.

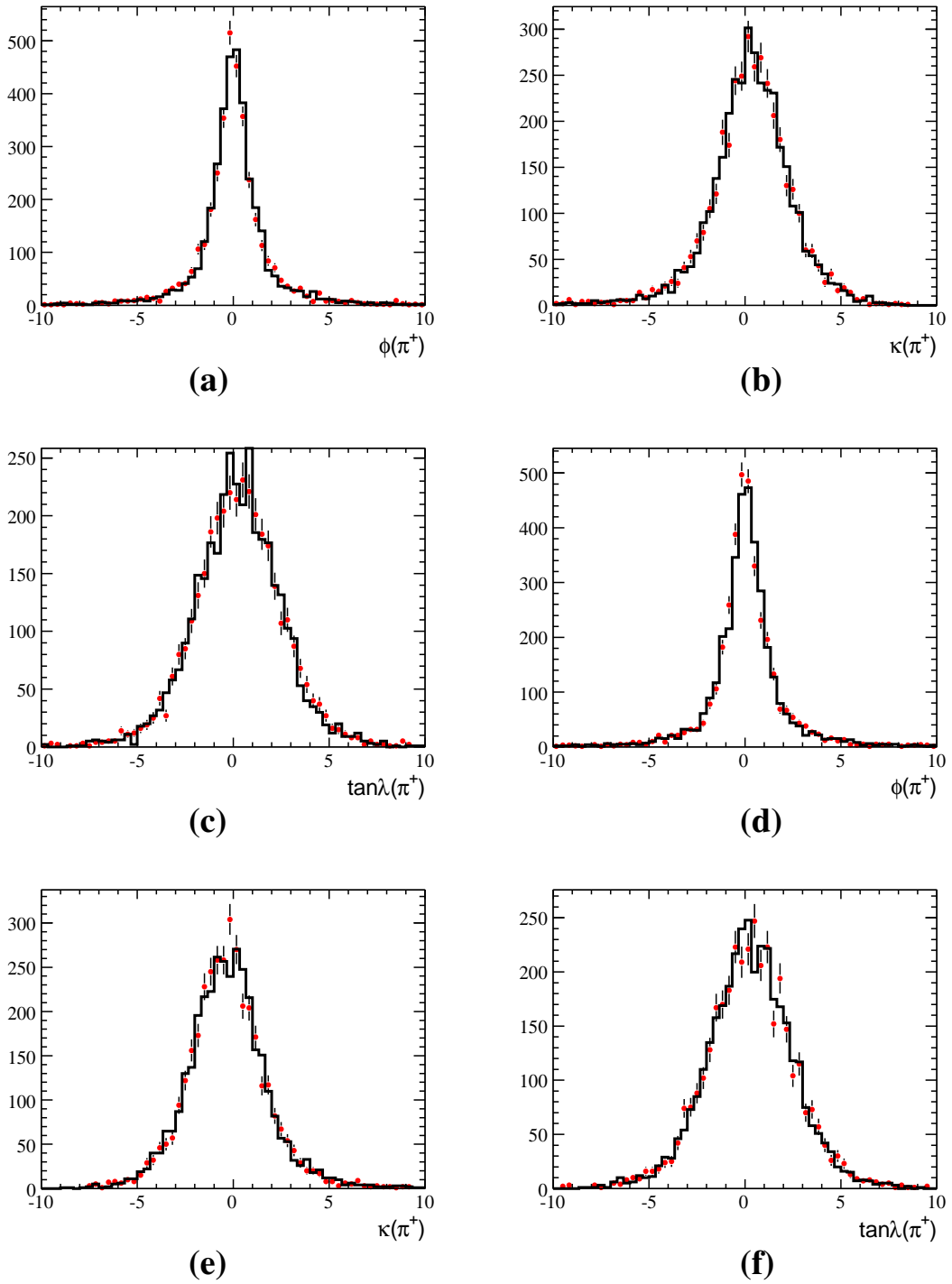


Figure A.5 The comparison of pull distribution between MC and data after correction, the red error bars are data, the black histograms are MC.

A.1.2.2 χ^2 distribution

Figures A.6 show the comparison of χ^2 between data and MC. With the parameters, the χ^2 distribution is improved obviously.

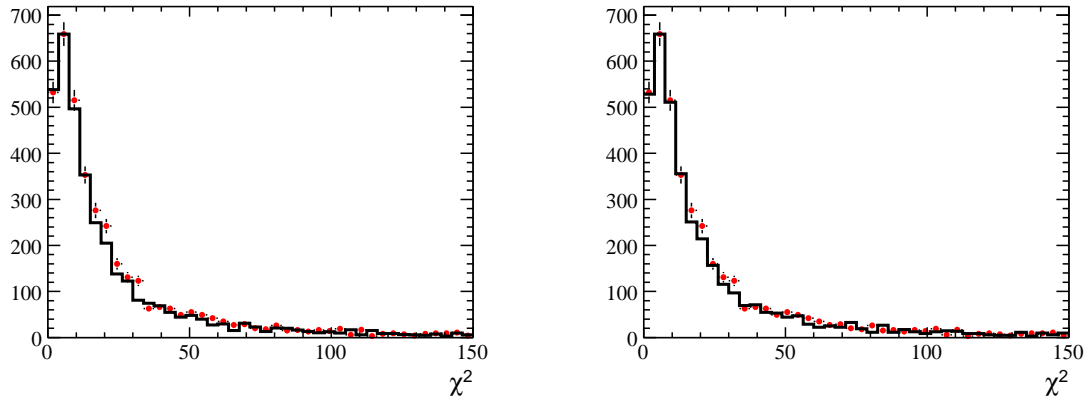


Figure A.6 The comparison of χ^2 between data and MC. The red dots are data, the black histogram is MC. Left: before correction Right: after correction.

A.1.3 $\psi(2S) \rightarrow \pi^0 J/\psi(l^+l^-)$ and $\eta J/\psi(l^+l^-)$

A.1.3.1 Event selection for $\psi(2S) \rightarrow \pi^+\pi^- J/\psi(l^+l^-)$

General event selections are the same as before, and the two tracks which have the lower momentum are taken as pion candidates, and the other two tracks are taken as leptons. To select a control samples with a high purity, the PID information has been applied, and require the probability of pion to be larger than 0.001. Other selection criteria are listed below:

- the polar angle $|\cos \theta| < 0.8$;
- require the event just has four charged tracks and the net charge equal to zero;
- the number of the good photon must smaller than 10;
- the momentum of pion has to be smaller than 450 MeV/c;
- use E/p ratio to identify the lepton. When the E/p of the charged tracks larger than 0.8, they will be identified as electron, while it smaller than 0.22, they will be identified as muon.
- $3.05 \text{ GeV}/c^2 < M_{l^+l^-} < 3.15 \text{ GeV}/c^2$;

The final efficiencies for $\psi(2S) \rightarrow \pi^+\pi^- J/\psi(e^+e^-)$ and $\psi(2S) \rightarrow \pi^+\pi^- J/\psi(\mu^+\mu^-)$ are $(25.10 \pm 0.10)\%$ and $(33.22 \pm 0.10)\%$, respectively. And their purities are 99.99%, and 99.86%, which obtain from 106M inclusive MC sample.

A.1.3.2 Comparison between MC and Data

Figures A.7 and A.8 shows the χ^2 distribution and the pull distributions obtained after the 4C-kinematic fitting for each kind of track. The mean values of $\tan \lambda$ in MC sample are significantly shifted away from the data, and the resolution of the parameter ϕ_0 and κ distributions in the MC are better than that in the data. It means that in order to match for the data distribution it is necessary to make a correction to the parameters of the charged tracks in the MC.

A.1.3.3 Correction factors for MC sample

The pull of the i^{th} track parameter is defined as $pull_i = \frac{\alpha_i - \alpha_{0i}}{\sqrt{|(V_{\alpha 0})_{ii} - (V_{\alpha})_{ii}|}}$, where α_0 is the unconstrained track parameters obtained from the reconstruction, α is the constrained track parameters obtained from kinematic fit and V is the corresponding covariance matrix element. Theoretically, the pull distribution is a standard normal distribution, but

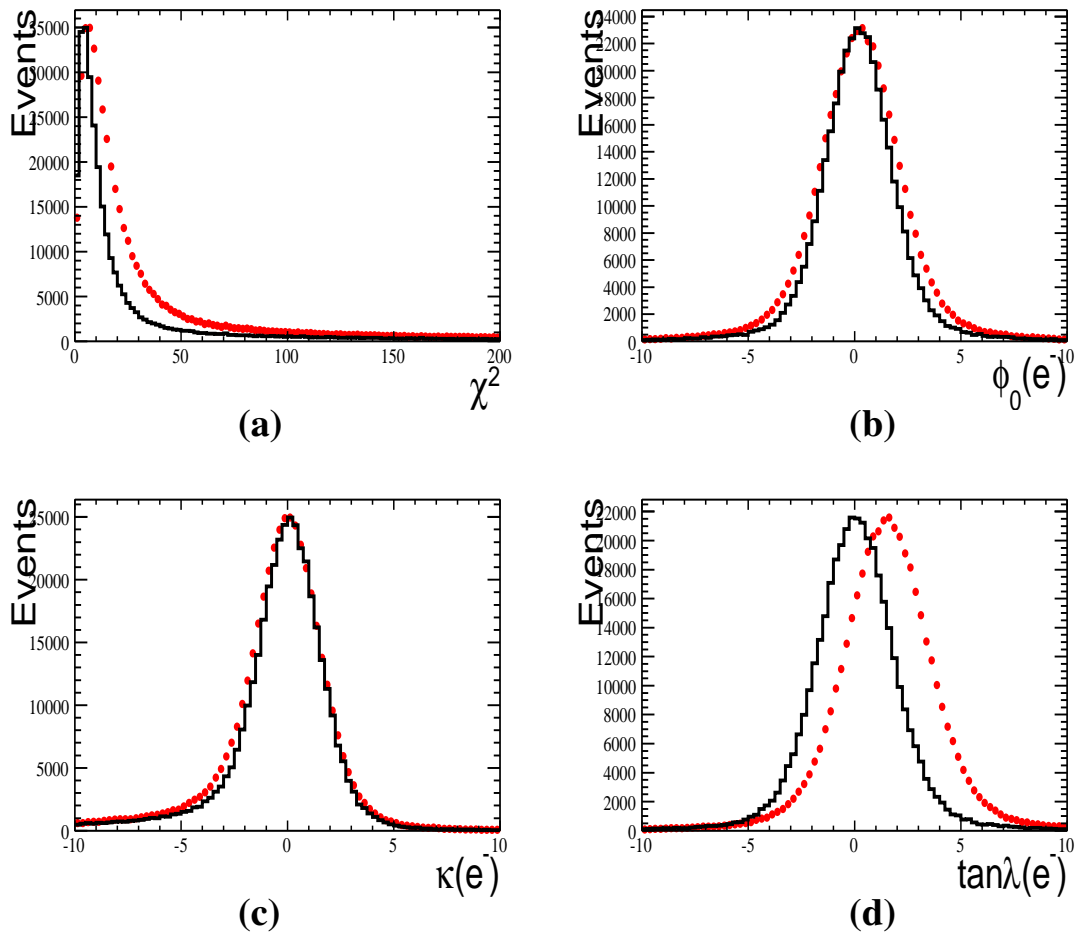


Figure A.7 the distributions of χ^2 and pull for electron

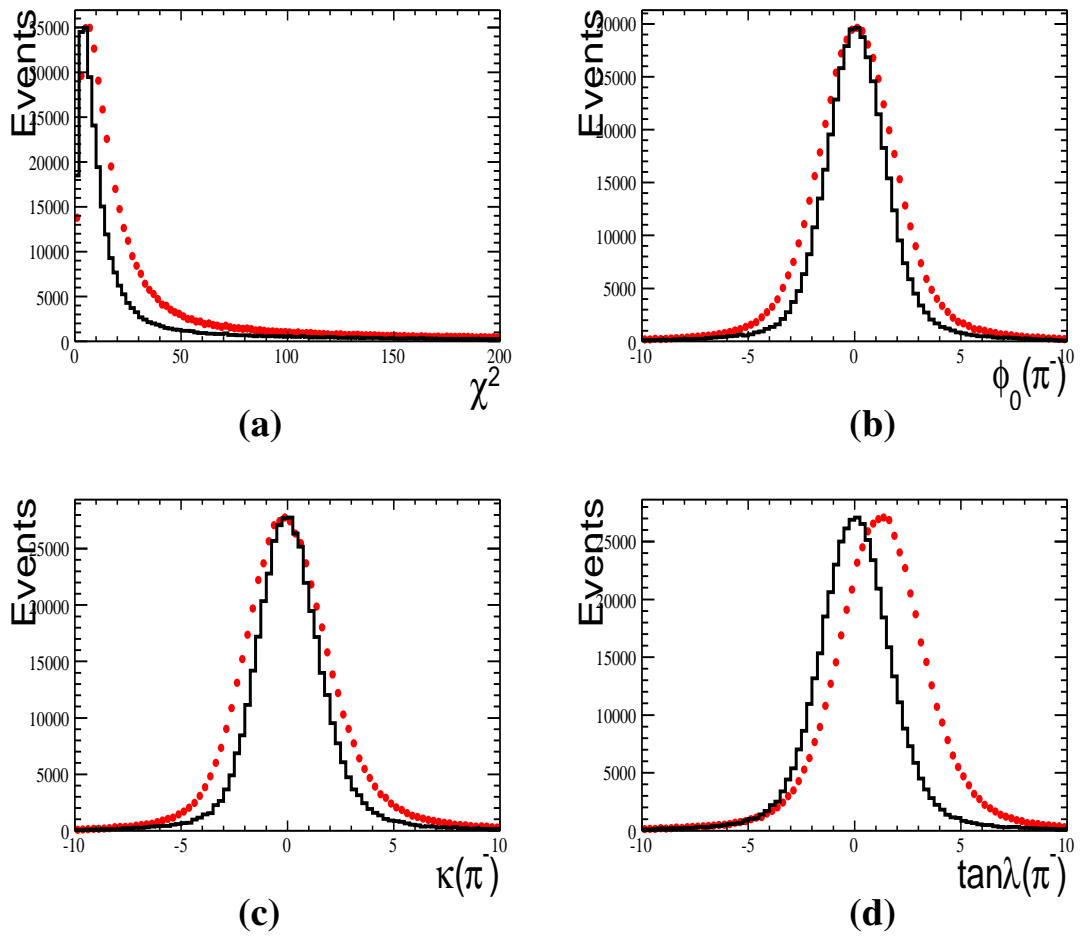


Figure A.8 the distributions of χ^2 and pull for pion

actually, it obeys a Normal distribution with mean μ_i and deviation σ_i . There are two methods to reduce the difference between data and MC. One is to reduce $(V_{\alpha 0})_{ii}$ by multiplying it with a factor $\sigma_i^{MC}/\sigma_i^{data}$, the other one is to smear the resolution of α_{0i} by smearing it with a Gaussian distribution, in which the mean and σ values are defined as $\alpha_{0i} + (\mu_i^{data} - \mu_i^{MC}) \times (V_{\alpha 0})_{ii}$ and $\sqrt{((\sigma_i^{data}/\sigma_i^{MC})^2 - 1) \times (V_{\alpha 0})_{ii}}$. Since the data and MC are consistent with each other in the covariance matrix from MdcKalTrk, it is unnecessary to change the covariance matrix, we choose the second method to correct the MC to data. Table 4.6 lists the corrected parameters for the lepton. Figures A.9 and A.10 shows the distributions of χ^2 and pull after the correction. With the parameters obtained from the pull distribution, the corrected MC is consistent with the data.

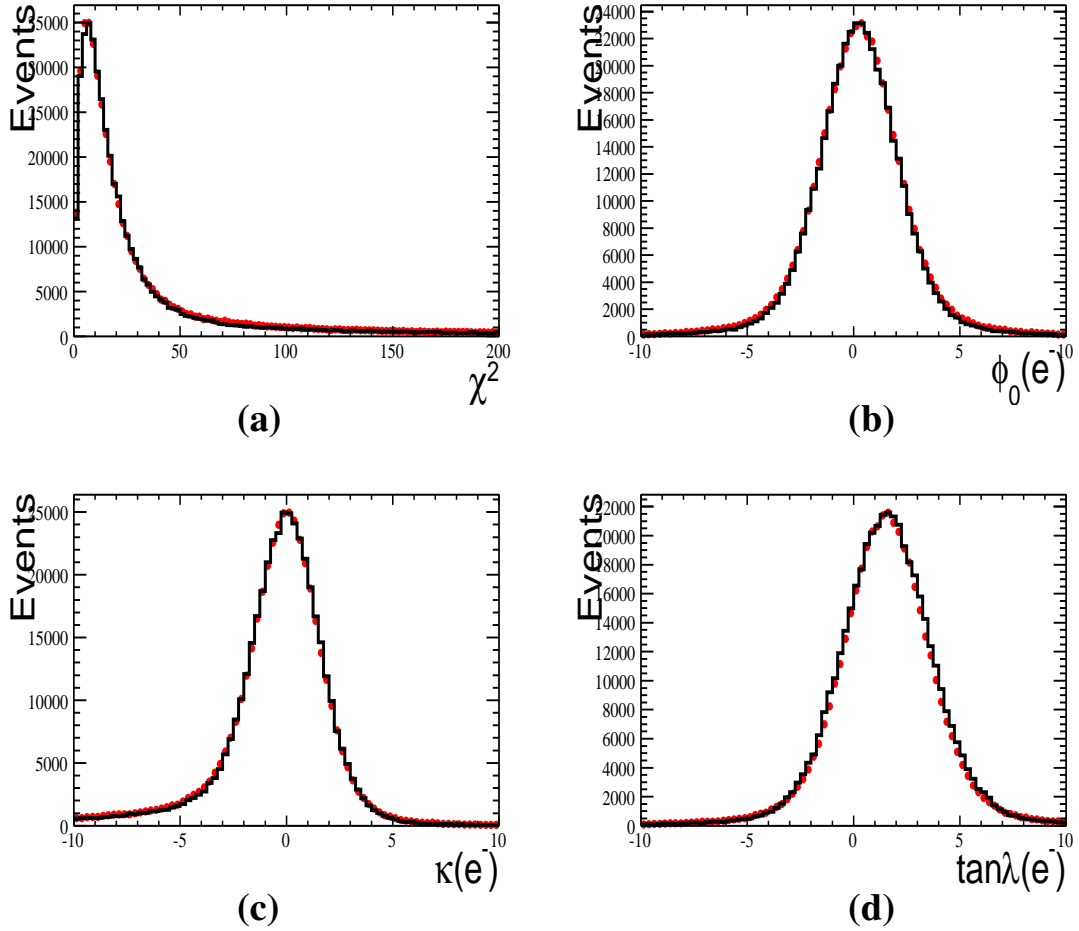


Figure A.9 the distributions of χ^2 and pull for electron after correction

With these parameters, we also correct another decay mode to check whether it work effectively. The decay modes are $\psi(2S) \rightarrow \gamma\chi_{cJ}(J = 1, 2), \chi_{cJ} \rightarrow \gamma J/\psi(l^+l^-)$. In order to

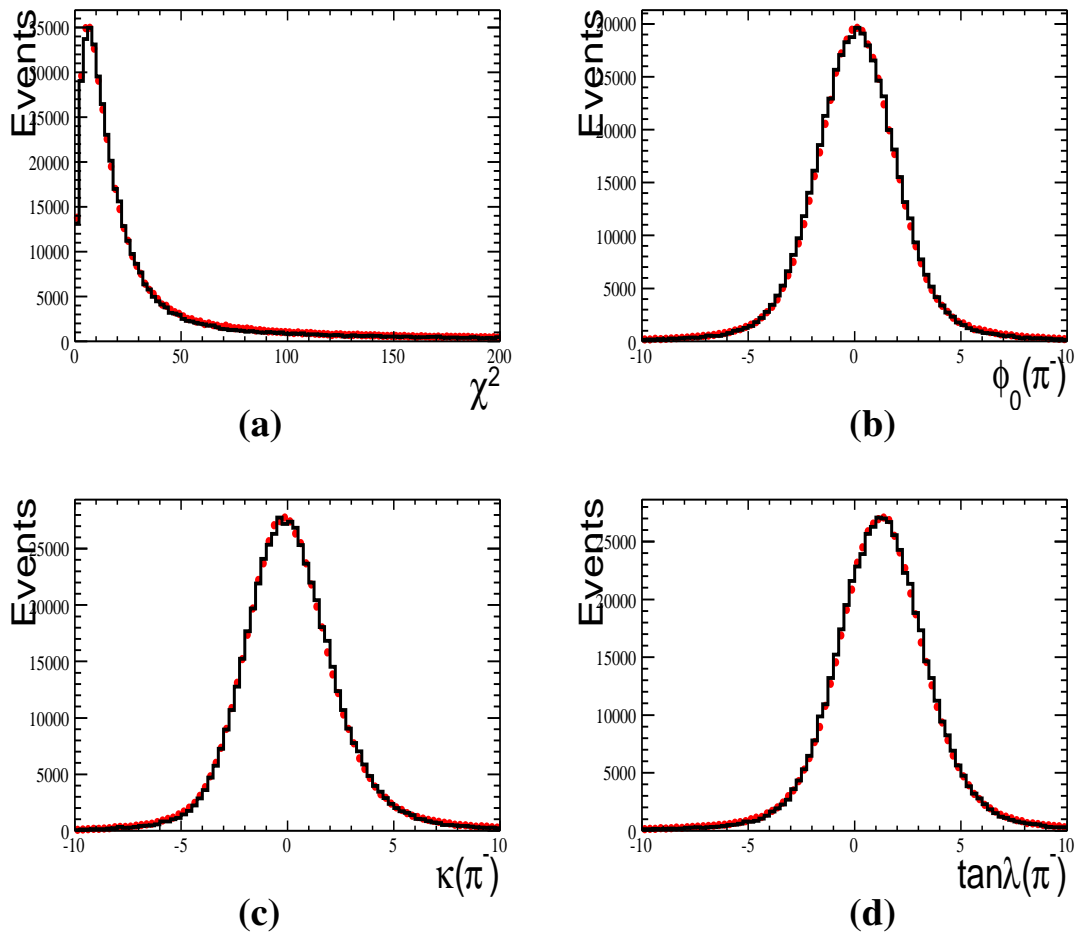


Figure A.10 the distributions of χ^2 and pull for electron after correction

select samples as pure as possible, the selection criteria for the good charged tracks and good photons are applied as the same as the normal criteria listed before, and the other selection criteria are required as listed below:

- the mass of the two lepton must be within the J/ψ mass window, $3.05 \text{ GeV}/c^2 < |M(l^+l^-)| < 3.15 \text{ GeV}/c^2$
- the mass of the two photons must not within the mass range of η and π^0 . $M(\gamma\gamma) < 0.12 \text{ GeV}/c^2$, or $M(\gamma\gamma) > 0.58 \text{ GeV}/c^2$, or $0.15 \text{ GeV}/c^2 < M(\gamma\gamma) < 0.50 \text{ GeV}/c^2$
- The mass of the highest energy photon and the two leptons, which have been constrained to the J/ψ mass window, must be between 3.43 GeV and 3.60 GeV

Figures A.11 show the mass distribution of $\gamma J/\psi$ and the distribution of χ^2 for the kinematic fitting. There are two clear peaks around the mass of χ_{c1} and χ_{c2} , and the corrected MC is consistent with the data very well. Table A.3 lists the main decay modes after these selection. The number of total event is 124440, and purity of final state with $\gamma\gamma e^+e^-$ is 93.34%, while that of the final state with $\gamma\gamma\gamma e^+e^-$ is 6.58% within the sample. The distribution of χ^2 between MC and data are not consistent with each other. Figures A.12

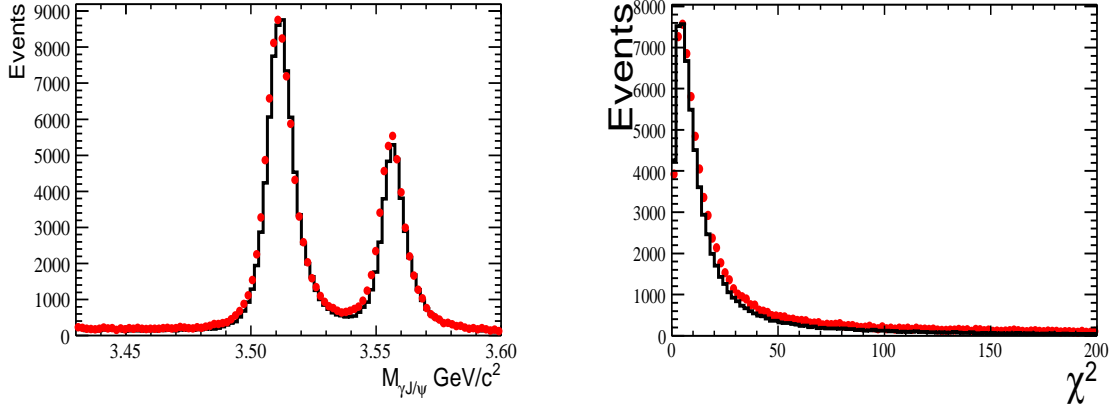
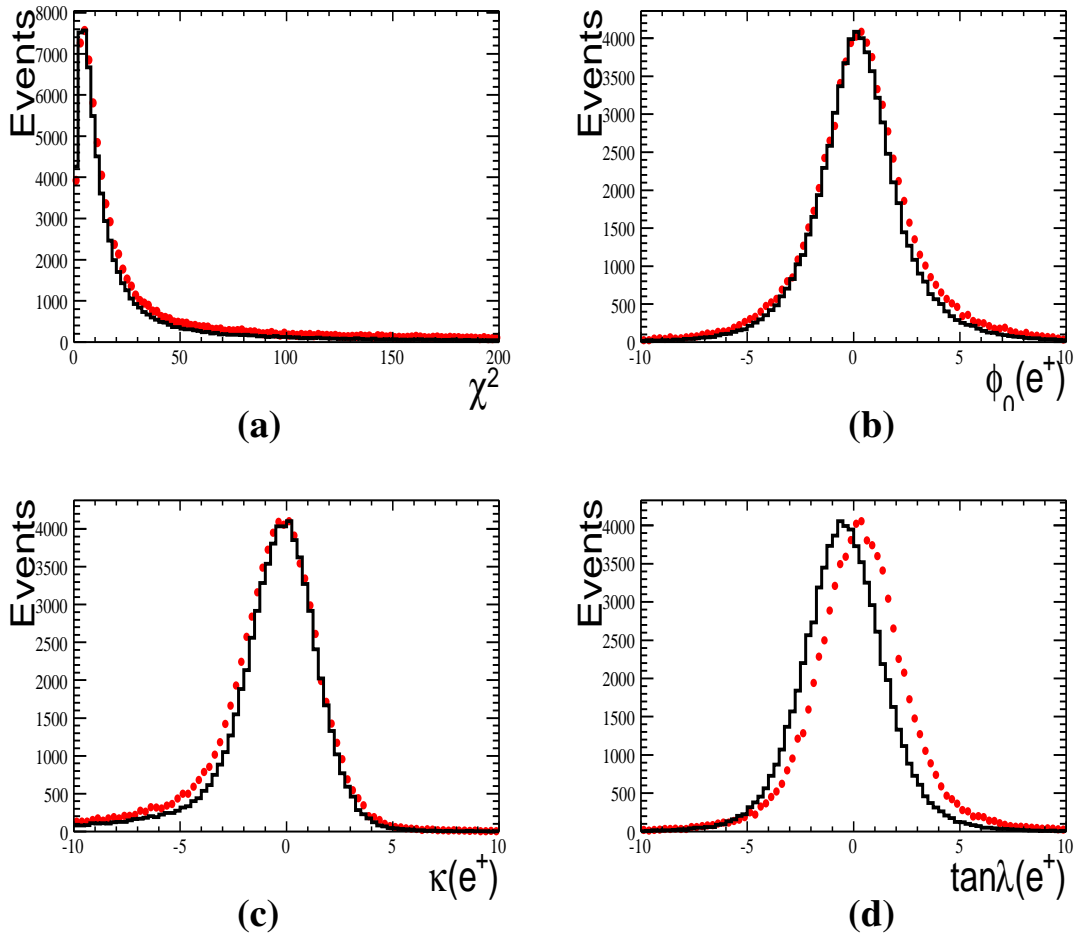


Figure A.11 The mass distribution of $\gamma J/\psi$ and the χ^2 distribution before correction.
 Left: $M_{\gamma J/\psi} \text{ GeV}/c^2$; Right: χ^2 distribution before correction

show the pull distributions; the MC and the data are different from each other. With the parameters from the control sample, we correct the MC sample, as you see figures A.13, they are consistent with each other very well.

Table A.3 summary of the decay channels for $\psi(2S) \rightarrow \gamma\chi_{c1,2}$

Decay channels	number of event	proportion(%)
$\psi(2S) \rightarrow \gamma\chi_{c1,2}, \chi_{c1,2} \rightarrow \gamma J/\psi(e^+e^-)$	113803	91.45
$\psi(2S) \rightarrow \pi^0\pi^0 J/\psi(e^+e^-)$	8189	6.58
$\psi(2S) \rightarrow \gamma\gamma J/\psi(e^+e^-)$	1473	1.18
$\psi(2S) \rightarrow \eta J/\psi(e^+e^-)$	500	0.4
total decay channels	124440	1.0


 Figure A.12 the distributions of χ^2 and pull for electron

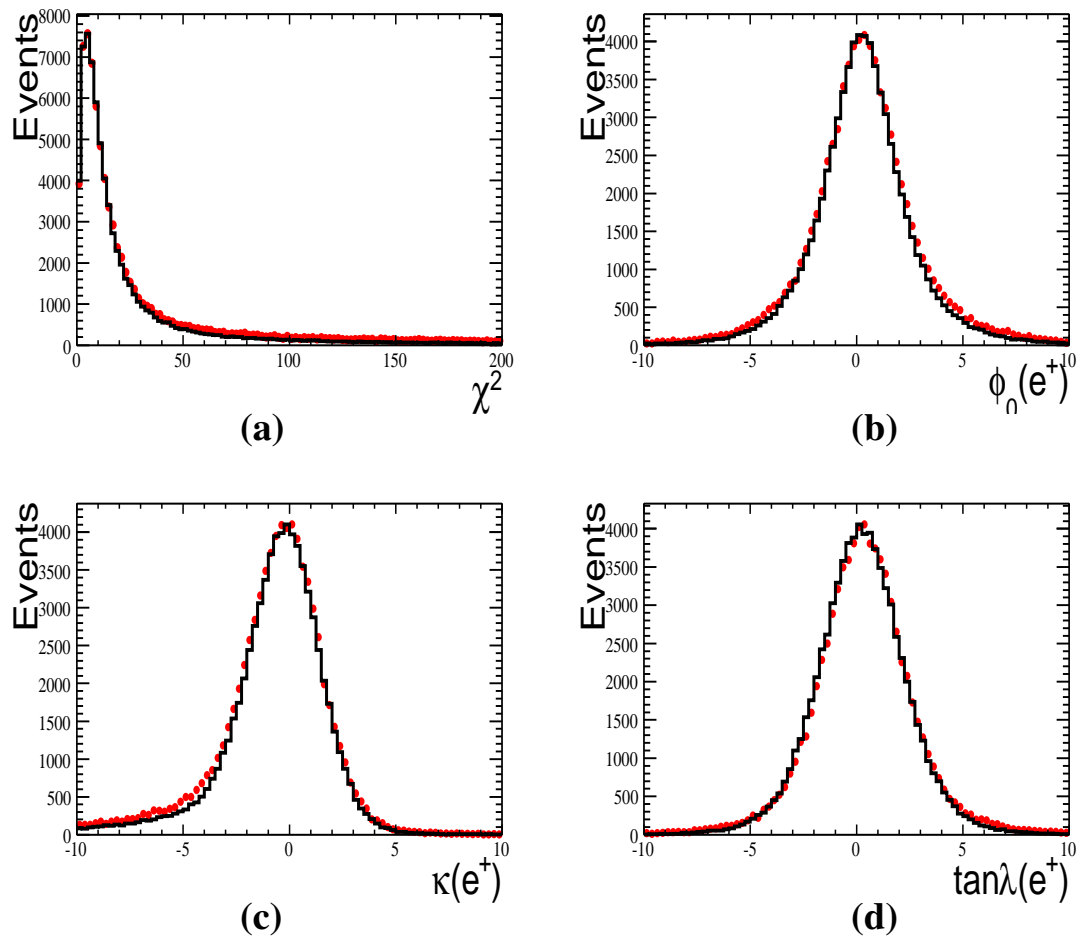


Figure A.13 the distributions of χ^2 and pull for electron after correction

A.1.3.4 Uncertainty of kinematic fitting

According to above analysis, the correction factors depend weakly on decay channels. So, we will use these parameters to correct the MC sample, and then we take half of the difference between with and without the correction for MC sample as the systematical error of 4C-kinematic fitting. Figures A.14 and A.15 show the pull distributions before and after correction, respectively.

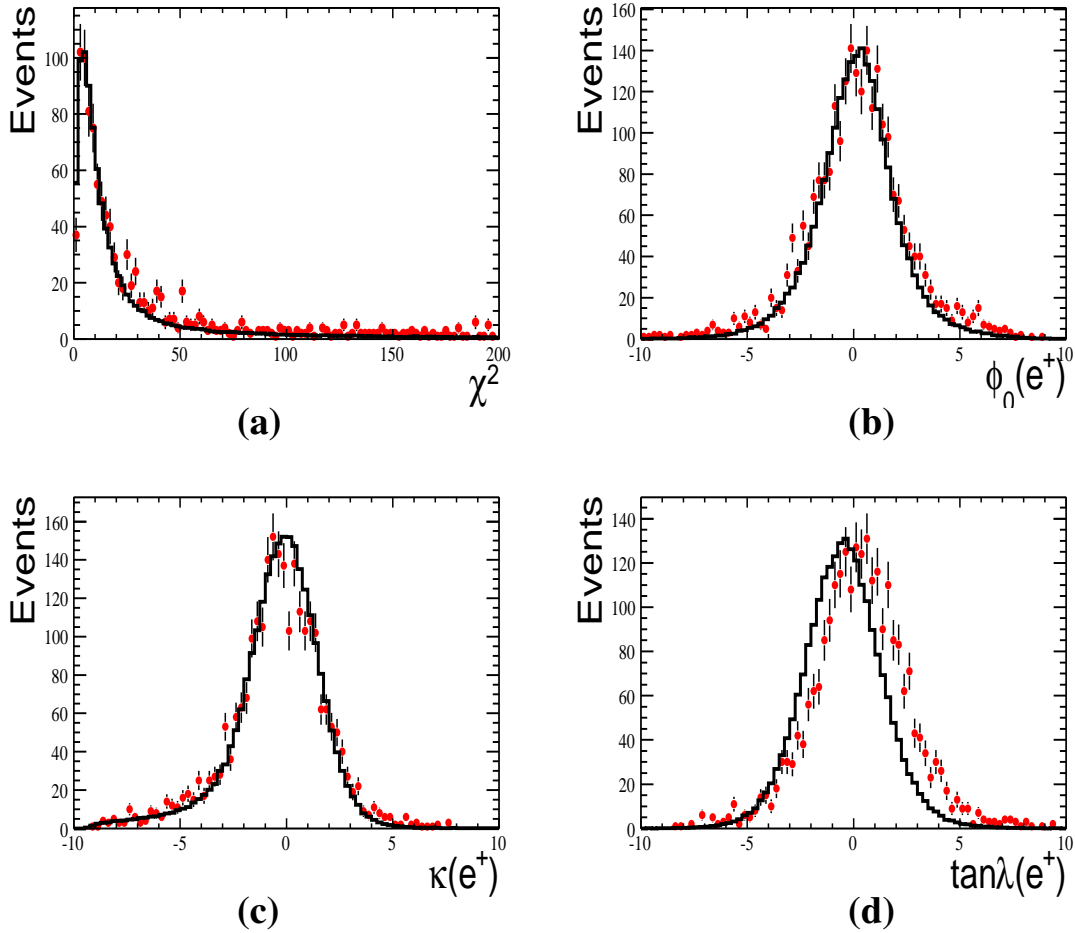


Figure A.14 the distributions of χ^2 and pull for electron

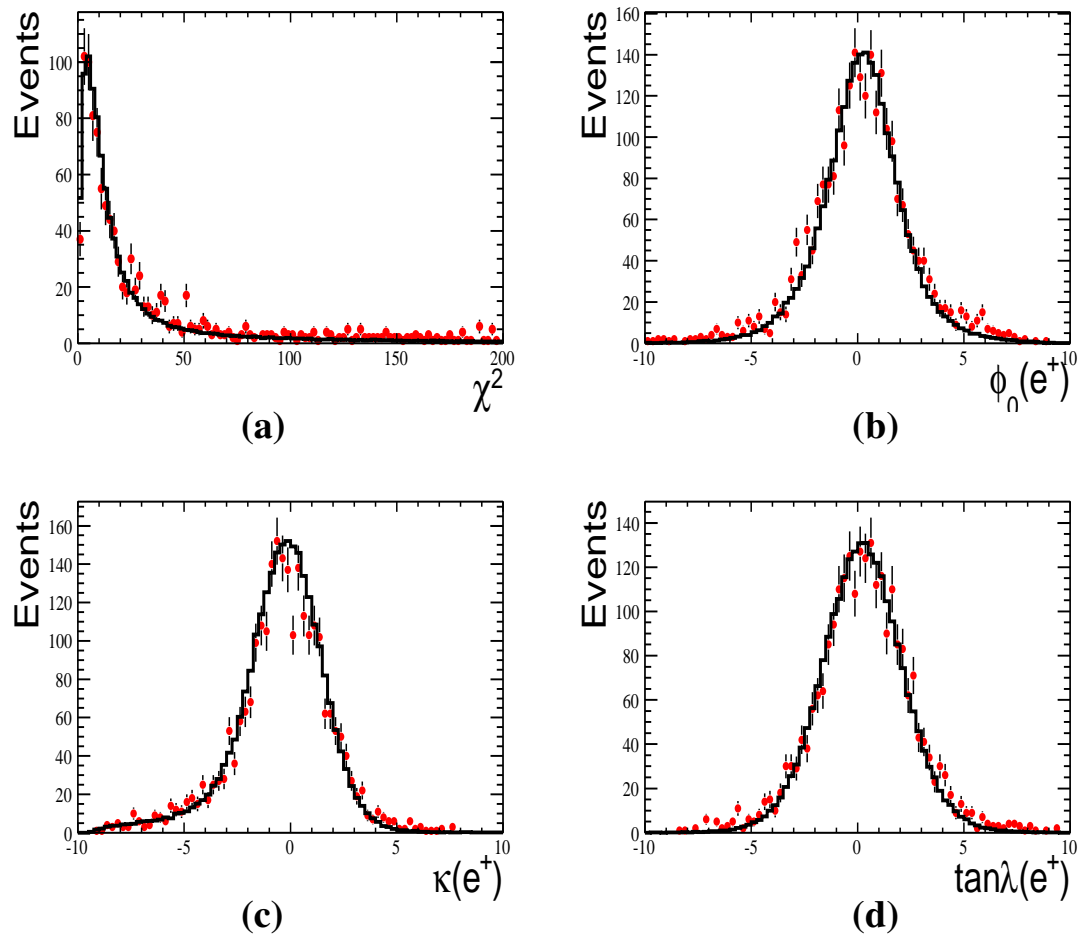


Figure A.15 the distributions of χ^2 and pull for electron after correction

Appendix B

B.1 Amplitude

B.1.1 Amplitude

Consider a decay $a(J, \eta_J) \rightarrow b(s, \eta_s) + c(\sigma, \eta_\sigma)$, where the quantum number (J, η_J) denotes (spin, parity), the decay amplitudes are given by:

$$A_{\lambda_1, \lambda_2}^J(\theta, \phi; M) \propto D_{M, \lambda_1 - \lambda_2}^{J*}(\phi, \theta, 0) F_{\lambda_1, \lambda_2}^J \quad (\text{B-1})$$

where λ_1 and λ_2 are the helicities of the two daughter particles, and $F_{\lambda_1, \lambda_2}^J$ is the helicity-coupling amplitude given by $F_{\lambda_1, \lambda_2}^J \propto \langle JM \lambda_1 \lambda_2 | T | JM \rangle$, which is constrained by the parity conservation and satisfied:

$$F_{\lambda\nu}^J = \eta_J \eta_s \eta_\sigma (-)^{J-s-\sigma} F_{-\lambda-\nu}^J \quad (\text{B-2})$$

In LS -coupling scheme, the helicity-coupling amplitudes $F_{\lambda\nu}^J$ can be build out of the particles' wave functions and momenta contracted with the modified metric $\tilde{g}_{\alpha\beta}(W) = -g_{\alpha\beta} + \frac{p_a p_b}{W}$. Here we cite Chung's formula^[94,95] as follows:

$$F_{\lambda\nu}^J = \sum_{ls} g_{ls} \left(\frac{2l+1}{2J+1} \right)^{1/2} \langle l0S \delta | J \delta \rangle \langle s \lambda \sigma - \nu | S \delta \rangle W^n r^l f_\lambda^s(\gamma_s) f_\nu^\sigma(\gamma_\sigma)$$

$$\text{with: } f_m^j(\gamma) = \frac{(j+m)!(j-m)!}{(2j)!} \sum_{m_0} \frac{j!(2\gamma)^{m_0}}{[(j+m-m_0)/2]![(j-m-m_0)/2]!m_0!} \quad (\text{B-3})$$

where g_{ls} is a coupling constant, and $\gamma_{s/\sigma} = \frac{E_{a/b}}{m_{a/b}}$ and $r = p_b - p_c$, which is always replaced with the barrier factor in data analysis, and W is the mass of the mother particle, and $n = 1$ for $s + \sigma + l - J$ odd and $n = 0$ otherwise.

For the decays $J/\psi(\lambda_0) \rightarrow \gamma(\lambda_\gamma)\eta_c \rightarrow \gamma\phi(\lambda_1)\phi(\lambda_2)$, where the $\lambda_i (i = \gamma, 0, 1, 2)$ indicate helicities for the photon and mesons, the helicity-coupling amplitudes is given by:

$$A_1(\lambda_0, \lambda_1, \lambda_2, \lambda_\gamma) = F_{\lambda_\gamma}^\psi(r_1) D_{\lambda_0, \lambda_\gamma}^{1*}(\theta_0, \phi_0) BW_j(m_{\phi\phi}) F_{\lambda_1, \lambda_2}^{\eta_c} F_{\lambda_1, \lambda_2}^{0*}(r_2) D_{0, \lambda_1 - \lambda_2}^{0*}(\theta_1, \phi_1) \quad (\text{B-4})$$

where $r_1(r_2)$ is the momentum differences between γ and η_c (ϕ and ϕ) in the CM system of J/ψ (η_c), and θ_0 (ϕ_0), θ_1 (ϕ_1) are the polar (azimuthal) angles of the momentum vector of γ (ϕ) in the CM system of J/ψ (η_c). $BW_j(m)$ denotes the Breit-Wigner for the η_c .

The helicity-coupling amplitudes $F_{\lambda_\gamma}^\psi$ and $F_{\lambda_1, \lambda_2}^{\eta_c}$ can be constructed in terms of Eq.(B-3), which are explicitly given by:

$$\begin{aligned} F_1^\psi &= -F_{-1}^\psi = \frac{r_1 m_\psi}{\sqrt{2}} g_{11} = \sqrt{2} |\vec{p}_\gamma| m_\psi g_{11} \\ F_{1,1}^{\eta_c} &= -F_{-1,-1}^{\eta_c} = \sqrt{2} |\vec{p}_\phi| m_{\eta_c} \\ F_{0,0}^{\eta_c} &= 0 \end{aligned} \quad (\text{B-5})$$

where g_{1s} is the coupling constant, m_ψ is the mass of J/ψ .

Under the η_c signal region, the non- η_c line shape is assumed smooth, but the $\phi\phi$ -system may have the quantum number $J^P = 0^-, 0^+$ and 2^+ . So the line shape for these states take as the phase space of $J/\psi \rightarrow \gamma\phi\phi$, and the angular distribution is taken into consideration with these amplitudes:

$$\begin{aligned} A_0^{0^-}(\lambda_0, \lambda_1, \lambda_2, \lambda_\gamma) &= G_{\lambda_\gamma, 0}^{0^-} D_{\lambda_0, \lambda_\gamma}^{1*}(\theta_0, \phi_0) H_{\lambda_1, \lambda_2}^{0^-} D_{0, \lambda_1 - \lambda_2}^{0*}(\theta_1, \phi_1) \text{ for } J^P = 0^- \\ A_0^{0^+}(\lambda_0, \lambda_1, \lambda_2, \lambda_\gamma) &= G_{\lambda_\gamma, 0}^{0^+} D_{\lambda_0, \lambda_\gamma}^{1*}(\theta_0, \phi_0) H_{\lambda_1, \lambda_2}^{0^+} D_{0, \lambda_1 - \lambda_2}^{0*}(\theta_1, \phi_1) \text{ for } J^P = 0^+ \\ A_0^{2^+}(\lambda_0, \lambda_1, \lambda_2, \lambda_\gamma) &= G_{\lambda_\gamma, \lambda_J}^{2^+} D_{\lambda_0, \lambda_\gamma - \lambda_J}^{1*}(\theta_0, \phi_0) H_{\lambda_1, \lambda_2}^{2^+} D_{\lambda_J, \lambda_1 - \lambda_2}^{2*}(\theta_1, \phi_1) \text{ for } J^P = 2^+ \end{aligned}$$

where $G_{\lambda_\gamma, \lambda_J}^{J^P}$ and $H_{\lambda_1, \lambda_2}^{J^P}$ are the helicity amplitudes for $J/\psi \rightarrow \gamma(\lambda_\gamma)J^P(\lambda_J)$ and $J^P(\lambda_J) \rightarrow \phi(\lambda_1)\phi(\lambda_2)$, respectively. These helicity amplitudes are required to satisfy the requirement of parity conservation, and we have:

$$\begin{aligned} G_{1,0}^{0^-} &= -G_{-1,0}^{0^-}, G_{1,0}^{0^+} = G_{-1,0}^{0^+}, G_{1,0}^{2^+} = -G_{-1,0}^{2^+}, G_{0,0}^{2^+} = 0 \\ H_{1,1}^{0^-} &= -H_{-1,-1}^{0^-}, H_{0,0}^{0^-} = 0, H_{1,1}^{0^+} = H_{-1,-1}^{0^+}, H_{0,0}^{0^+} \neq 0 \\ H_{1,1}^{2^+} &= H_{-1,-1}^{2^+}, H_{1,0}^{2^+} = H_{-1,0}^{2^+} = H_{0,1}^{2^+} = H_{0,-1}^{2^+}, H_{-1,1}^{2^+} = H_{1,-1}^{2^+}, H_{0,0}^{2^+} \neq 0 \end{aligned} \quad (\text{B-6})$$

where the identical particle symmetry has implemented. These free parameters are determined to fit data.

The total amplitude is expressed by:

$$A(\lambda_0, \lambda_1, \lambda_2, \lambda_\gamma) = \sum_{J^P=0^-, 0^+, 2^+} A_0^{J^P}(\lambda_0, \lambda_1, \lambda_2, \lambda_\gamma) + A_1(\lambda_0, \lambda_1, \lambda_2, \lambda_\gamma) \quad (\text{B-7})$$

The differential cross-section is given by:

$$d\Gamma = \left(\frac{3}{8\pi^2} \right) \sum_{\lambda_0, \lambda_1, \lambda_2, \lambda_\gamma} A(\lambda_0, \lambda_1, \lambda_2, \lambda_\gamma) A^*(\lambda_0, \lambda_1, \lambda_2, \lambda_\gamma) d\phi_3 \quad (\text{B-8})$$

where $\lambda_0, \lambda_\gamma = \pm 1$, and $\lambda_1, \lambda_2 = \pm 1, 0$, and $d\phi_3$ is the element of standard 3-body phase space.

B.1.2 Breit-Wigner

We use a relativistic Breit-Wigner in the analysis, ie.

$$BW(m) = \frac{1}{m^2 - m_0^2 - im\Gamma} \quad (\text{B-9})$$

where m_0 is the nominal mass for the resonance, eg. η_c , with a width Γ .

B.2 Fit method

The relative magnitudes and phases for coupling constants are determined by an unbinned maximum likelihood fit. The joint probability density for observing the N events in the data sample is

$$\mathcal{L} = \prod_{i=1}^N P(x_i) \quad (\text{B-10})$$

where $P(x_i)$ is a probability to produce event i with four-vector momentum $x_i = (p_{K^+}, p_{K^-}, p_{\pi^0})_i$. The normalized $P(x_i)$ is calculated from the differential cross section

$$P(x_i) = \frac{(d\sigma/d\Phi)_i}{\sigma_{MC}} \quad (\text{B-11})$$

where the normalization factor σ_{MC} is calculated from a MC sample with N_{MC} accepted events, which are generated with a phase space model and then subject to the detector simulation, and are passed through the same event selection criteria as applied to the data analysis. With an MC sample of sufficiently large size, the σ_{MC} is evaluated with

$$\sigma_{MC} = \frac{1}{N_{MC}} \sum_{i=1}^{N_{MC}} \left(\frac{d\sigma}{d\Phi} \right)_i \quad (\text{B-12})$$

For technical reasons, rather than maximizing \mathcal{L} , $S = -\ln \mathcal{L}$ is minimized using the package MINUIT. To subtract the non-interference backgrounds, the $\ln \mathcal{L}$ function is replaced with:

$$\ln \mathcal{L} = \ln \mathcal{L}_{\text{data}} - \ln \mathcal{L}_{\text{bg}} \quad (\text{B-13})$$

Resume and Publications

Resume

- Mar. 1984, born in LiuZhou, Guangxi Province, China
- Sep. 2003 - Jul. 2007, Bachelor of Physics. Guangxi Normal University, Guilin, China.
- Sep. 2007 - Jul. 2008, Master of Physics. Guangxi Normal University, Guilin, China.
- Jul. 2008 - Jul. 2010, Institute of High Energy Physics, Chinese Academy of Sciences, Beijing, China.
- Sep. 2010 - Present, Ph.D. candidate in Physics. Department of Engineering Physics, Tsinghua University, Beijing, China

Publications

- [1] G. R. Liao (on behalf of BESIII Collaboration), Precision measurements of branching fractions for $\psi(2S) \rightarrow \pi^0 J/\psi$ and $\eta J/\psi$. Phys. Rev. D **86**, 092008(2012)